Sulfheme Formation mechanism and spectra analysis using QM/MM and TDDFT

by
Héctor D. Arbelo-López

A dissertation submitted in partial fulfillment of the requirements for the degree of
Doctor in Philosophy
In
Applied Chemistry
In
Biophysics
UNIVERSITY OF PUERTO RICO
MAYAGÜEZ CAMPUS
2018

Dissertation and Defense Approved by Committee:

_____ _____
Juan López-Garriga, PhD Date
President, Graduate Committee

_____ _____
Samuel Hernandez, PhD Date
Member, Graduate Committee

_____ _____
Carmen A. Vega, PhD Date
Member, Graduate Committee

_____ _____
Alberto Santana, PhD Date
Member, Graduate Committee

_____ _____
Carlos Quiñones Padovani, PhD Date
Representative, Graduate Studies Office

_____ _____
Enrique Meléndez, PhD Date
Chairperson of the Department

Abstract

Since the 1863 discovery of a new green hemoglobin derivative called “sulfhemoglobin”, the nature of its characteristic 618 nm absorption band and formation mechanism has been the subject of several hypotheses. Many heme-containing proteins with a histidine in the distal E7 (HisE7) position can form sulfheme in the presence of hydrogen sulfide (H_2S) and a reactive oxygen species such as hydrogen peroxide. For unknown reasons, sulfheme derivatives are formed specifically on the solvent-excluded heme pyrrole B. Here, the use of hybrid Quantum Mechanical/Molecular Mechanical (QM/MM) methods have permitted characterization of the entire process of sulfheme formation in the HisE7 mutant of hemoglobin I (HbI) from *Lucina pectinata*. This process includes a mechanism for H_2S to enter the solvent excluded active site through a hydrophobic channel to ultimately form a hydrogen bond with H_2O_2 bound to Fe(III). Proton transfer from H_2O_2 to His64 to form Compound (Cpd) 0 followed by hydrogen transfer from H_2S to Fe(III)-H_2O_2 complex results in homolytic cleavage of the O-O and S-H bond to form a reactive thiyl radical (HS•), ferryl heme compound II (Cpd II) and a water molecule. Subsequently, HS• addition to Cpd II followed by three proton transfer reactions results in the formation of a 3-membered ring ferric sulfheme (S_A) that avoids the migration of the radical to the protein matrix in contrast to other peroxidative reactions. The transformation of S_A to the 5-membered thiochlorin ring structure (S_C) occurs through a significant potential energy barrier though both structures are nearly isoenergetic. Both S_A and S_C reveal a longer N_B--Fe(III) bond than the other pyrrole nitrogen--Fe(III) bonds which would lead to a decreased in oxygen binding. The sulfheme experimental spectra are a function of the observation time, and interplay between two major sulfheme isomer concentrations (S_A and S_C); the latter being the dominant isomer at longer times. Thus, time-dependent density functional theory (TDDFT) was used to calculate the sulfheme excited states and visualize the highest occupied molecular orbitals (HOMOs) and lowest unoccupied MOs (LUMOs) of

both isomers in order to interpret the transitions between them. Formation of the three-membered ring S_A and S_C isomeric structures decrease the energy of the HOMO a_{1u} and a_{2u} orbitals compared to the unmodified heme due to the electron-withdrawing sulfur-containing ring. The calculations reveal that the absorption spectrum within the 700 nm region arises from a mixture of MOs, but can be characterized as π to π^* transitions, while the 600 nm region is characterized by π to d_π (d_{yz}, d_{xz}) transitions having components of a deoxy like derivative. Overall, these results are in agreement with a wide range of experimental data and provide fertile ground for further investigations of sulfheme formation in other heme proteins, and additional effects of H_2S on cell signaling and reactivity.

Resumen

Desde el descubrimiento en 1863 de un nuevo derivado de hemoglobina de color verde llamado "sulfhemoglobina", la naturaleza de la banda característica de absorción a 618 nm y el mecanismo de formación ha sido objeto de varias hipótesis. Muchas hemo proteínas con histidina en la posición distal E7 (HisE7) pueden formar sulfhemoglobina al estas reacionar con una especie de oxígeno reactivo tal como peróxido de hidrógeno en presencia de sulfuro de hidrógeno (H_2S). Por razones desconocidas, la modificación al grupo hemo al formarse sulfhemoglobina ocurre específicamente en el pirrol B, el cual está dentro de la matriz proteica fuera del contacto con el solvente. En este trabajo se usaron métodos híbridos Mecánicos Cuánticos / Mecánicos Moleculares (QM / MM) que han permitido la caracterización del proceso de formación de sulfhemoglobina en el mutante HisE7 de hemoglobina I (HbI) de *Lucina pectinata*. Se encontró un mecanismo para que el H_2S ingrese al sitio activo a través de un canal hidrofóbico, para finalmente formar un enlace de hidrógeno con H_2O_2 unido al Fe (III). Una transferencia de protones de H_2O_2 a His64 para formar el Compuesto (Cpd) 0 seguido de transferencia de hidrógeno del complejo H_2S al Cpd 0 da como resultado la escisión homolítica del enlace O-O y SH para formar un radical reactivo de tiílo ($HS^{\bullet}$), compuesto II (Cpd II) y una molécula de agua. Posteriormente, la adición de $HS^{\bullet}$ a Cpd II seguida por tres reacciones de transferencia de protones da como resultado la formación del isómero de 3 miembros de sulfhemoglobina (S_A). Este mecanismo evita la migración del radical generado a la matriz proteica lo cual contrasta con otras reacciones peroxidativas. La transformación de esta estructura de S_A a una estructura de anillo de tioclorina de 5 miembros (S_C) se produce a través de una barrera de energía potencial significativa, aunque ambas estructuras son casi isoenergéticas. Ambos isómeros revelan un enlace N_B - Fe (III) más largo que el observado para los otros enlaces de nitrógeno a Fe (III) lo que podría explicar la redución de afinidad con oxígeno de sulfhemoglobina comparado con la afinidad por oxígeno de hemoglobina. Los espectros experimentales de sulfhemoglobina dependen del tiempo de observación y la interacción

entre las concentraciones de sus principales isómeros (S_A y S_C); siendo este último el isómero dominante en tiempos más largos. Por lo tanto, se usó la teoría de funcional de densidad dependiente del tiempo (TDDFT) para calcular los estados excitados de sulfhemo y visualizar los orbitales moleculares ocupados de más alta energía (HOMO) y los orbitales moleculares (MO) desocupados de más baja energía (LUMO) de ambos isómeros para interpretar las transiciones de ellos. La formación de los isoméros S_A y S_C disminuyen la energía de los orbitales HOMO a_{1u} y a_{2u} en comparación con el hemo. Los cálculos revelan que el espectro de absorción dentro de la región de 700 nm surge de una mezcla de MO, pero se puede caracterizar como transiciones π a π^*, mientras que la región de 600 nm se caracteriza por transiciones de π a d_π (d_{yz}, d_{xz}). En general, estos resultados están de acuerdo con una amplia gama de datos experimentales y proporcionan un terreno fértil para investigaciones adicionales en la formación de sulfhemo en otras hemo proteínas, y los efectos adicionales de la reactividad y la señalización celular de H_2S.

Dedication

Wrath, Anger , Hate are hard strong emotions
that will give you strength to walk through the dark.
Nevertheless, Patience,Kindness, Candor and Love
are soft, warm, weak and vulnerable emotions
that truly can make us invincible
and through the harshest cold darkness will make us shine.

To my family
Thank you for your love.
Your love has always been the lighthouse
that takes me to safe waters,
Your love had help me
to keep pushing the boundaries to improve myself

Acknowledgments

First I thank God for giving me strength every time I lifted my eyes over the hills. To my family and my life partner Glenda for their unconditional love and support. To my nieces Zrayre N.C. Arbelo and Zoeiry N.C. Arbelo thank you for been my sunshine, and keeping me happy when skies were gray. Thank you for my teachers because as Zrayre N.C. Arbelo told me when she was in first grade, they where who taught me to read, and had take to here. To Edgardo J Quinones-Cruz, Neit Nieves-Flores, Roberto Barreto, Angel D. Rodriguez-Mackenzie and all my friends for teaching me the great meaning of friendship and to enrich my life with your help.

I will like to thank my mentor and scientific father, Dr. Juan Lopez-Garriga, for his support, guidance, who believe in me all this years. To my second mentor, Dr. Troy Wymore will like to thank sharing his knowledge that made possible this theoretical voyage, for his support, and loyalty through all these years. I will also like to thank my dissertation committee members, Dr. Alberto Santana, Dr. Samuel Hernandez, for their guidance, support and understanding. I'm very grateful to the Chemistry Department of the University of Puerto Rico, Mayagüez Campus, for their support through all this years. To my second family at Science on Wheels and laboratory partners, thank you for been an important part in my professional and personal development.

This work was supported by funds from Alfred P. Sloan (NACME Grant 2010-3-02), National Science Foundation (NSF/MCB Grant 0843608, JLG), the National Institutes of Health (NIH 5T36GM095335-04, R25GM088023 to JLG). I will like to thank for the computational time to the Pittsburgh Supercomputing Center, to the Oak Ridge National Lab Center for Structural Molecular Biology a U.S. Department of Energy (DOE) facility, and to the University of Michigan Chemistry Department.

Table of Contents

Figures Index

Index of Tables

1 Sulfheme formation mechanism by homolytic cleavage

1.1 Introduction

1.1.1 Iron and the heme group

Iron evolution in this planet is tightly attached to oxygen and its reactions through in organisms. It has helped maintaining energy requirements for organism through the reaction with oxidative species, helping with the modification by oxidation or reduction of carbon compounds. As part of this evolutionary process, porphyrin groups are synthesized. The final step of iron insertion into the heme group came to be placed later in the outer zone of mitochondria[1]. The iron insertion to form the heme group opens a new array of complex reactions that go from electron transfer reduction to oxygen molecule transportation. This iron porphyrin group has evolved to form part of different systems as organisms evolved. The hemoglobin super family have this characteristic organometallic group in their active site. This protein super family takes advantage of iron availability as the second most abundant metal in the planet, and irons wide range redox potential which goes from 1 to -550 mV. By exploiting the oxidation states, electron spin state, and redox potential, biological systems can adjust the chemical reactivity of iron to suit physiological needs[2].

The heme group is widely conserved through the heme protein super family. This family of proteins takes part in a wide range of physiological reactions that goes from a molecule transfer to an electron transfer. Hemoglobin is an example of a molecule transportation protein that binds oxygen to the heme iron at the lungs; then oxygen is released in the tissue to be used by cells in its metabolic needs. As an electron transfer heme protein there is the cytochrome c system, which is part of the respiratory chain presented in the mitochondria inner membrane. **Figure 1** presents the protoporphyrin IX heme group usually conserved in many heme families. This large organic heterocyclic is composed

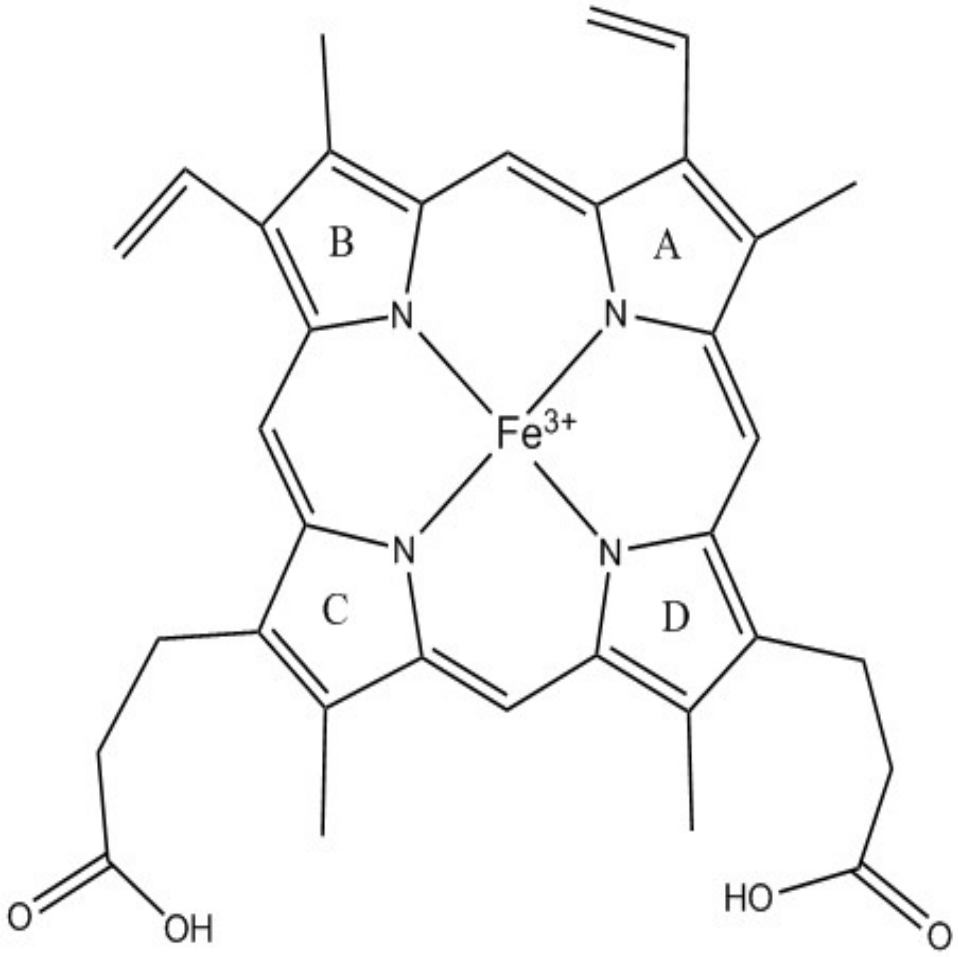

Figure 1: Protoporphyrin IX heme group.

of four pyrroline subunits interconnected via their alpha carbon atoms via methine bridges (=CH-). It has two vinyls groups, four methyl and two propionates as side chains in the macrocycle. It has a coordinated iron to the four nitrogen atoms of the pyrroline sub-units. The iron fifth and sixth coordination positions are free. One of the free coordination positions is used in a covalent bond by an active site amino acid which attaches the heme group to the enzyme protein matrix. The heme macro-cycle is a planar system with a delocalized π system. The π systems interact with the d orbitals of the iron. This creates, in many cases, an open d-shell which allows for various possible electronic configurations and can support different spin- multiplets (low spin, intermediate, and high-spin states), resulting in a spin-crossover behavior in many cases[3]. Interestingly, the chemical properties of the heme group are mainly dominated by the central transition atom. In reactions of heme proteins with hydrogen peroxide, the heme side chains play a role in the electronic density distribution through the reaction. This possibly help minimize the energy of the reaction transient species.

The heme group reactivity in heme protein is fine tuned and tailored for the physiological necessity by the protein active site amino acids, and the passages created by protein dynamics for ligand movement from the solution through the protein matrix into the active site. There are different types of heme groups inside this super family of proteins. The heme groups vary between them only at the side chains present in the heme group. There are approximately nine variants of heme prosthetic groups, such as chlorocruoroheme, which has a vinyl changed to an aldehyde. Chlorocruoroheme is present in chlorocrorins, which are oxygen binding hemoglobins present in annelids. Another example is heme D present in some catalases which decomposes hydrogen peroxide. Also, heme D is present in monooxygenases, which insert one oxygen atom from O_2 to a substrate and forms water. In the end, there is hemoglobin and myoglobins, which usually are oxygen binding proteins. One exception to this is *Lucina pectinata* HbI, whose its function is to transfer H_2S to an autotrophic bacteria with which it has a symbiotic relationship[4]. In some cases, it has been found that myoglobin can act as peroxidases,

but in these reactions, it get its iron finish with an oxidation state Fe^{+3}, rendering it unable to bind oxygen anymore. This new peroxidative role and other reactions involving hydrogen peroxide are of great interest today. Flögel and corroborators have proposed that, in the case of myoglobin, it plays an influential key role in redox pathways in cardiac muscle to functionally and metabolically protect the heart from oxidative damage[5,6].

1.1.2 Heme proteins reactions with hydrogen peroxide

Hydrogen peroxide has a long life because the peroxide bond (O-O) is relatively strong. The O-O bond distance in the hydrogen peroxide molecule is approximately 1.47 Å and has a bond energy of 51 kcal/mol^{-1} [7]. In order to facilitate the breakup of H_2O_2 into water and oxygen, the peroxide bond needs to be cleaved. This bond cleavage unleashes the oxidizing power of hydrogen peroxide. Hydrogen peroxide decomposition generates highly unstable and reactive oxidizing agents like superoxide (O_2^-) and hydroxyl radical ($OH^{\cdot}$). The reactivity of hydrogen peroxide and those oxidizing agents can cause severe damage to macromolecules in biological systems. Hydrogen peroxide is naturally generated as a byproduct of cellular oxygen metabolism, oxidative stress and other reactive oxygen species (ROS). Hydrogen peroxide and other ROS damage the DNA, proteins and cell membranes. Mechanisms for coping with oxidative stress are crucial for the survival of all organisms[8].

Peroxidases are hemeproteins that have found a way to cleave the O-O bound in an energetically favorable way. Peroxidases not only decompose hydrogen peroxide, but also are capable of taking advantage of its oxidizing power to catalyze a number of oxidative reactions. Peroxidases are found in plants, bacteria and animals, and it forms an enzyme super family inside the heme protein family. It is important for the organism to deal with hydrogen peroxide and harvest its oxidation nature for many cellular metabolic pathways. Some examples of different members of the peroxidase family are going to be briefly mentioned ahead. One of these members is the haloperoxidase family. Haloperoxidases

catalyze the halides transformation in the presence of hydrogen peroxide. Haloperoxidases are found in fungi, bacteria and red algae. Chloroperoxidase is a haloperoxidase that is a glycoprotein which catalyzes halogenation reactions using hydrogen peroxide. This enzyme has unique aspects but shares holding a distal polar pocket commonly found in other peroxidases[9]. Chloroperoxidase exhibits peroxidase, catalase and cytochrome P450 activity as well to catalyzing halogenation reactivity.

Other peroxidase family member is peroxidase-cyclooxygenase. Members of this family reduce hydrogen peroxide and oxidize a variety of organic and inorganic compounds. Some representatives of this family are: Myeloperoxidase, Lacto peroxidase, Eosinophil peroxidase, and Thyroid peroxidase. Myeloperoxidase uses H_2O_2 and chloride anion to produce hypochlorous acid and a tyrosyl radical, which are used to kill bacteria. Eosinophil peroxidase is similar to myeloperoxidase and is involved in combating infections and parasites; it is present in another type of white cell called Eosinophil granulocytes[10]. Lactoperoxidase is a peroxidase present in milk. It has antioxidant and antimicrobial properties. Lactoperoxidase uses H_2O_2 to oxidate thiocyanate ions (SCN^-), producing hypothiocyante ($OSCN^-$) which is considered to be bactericidal. Thyroid peroxidase is expressed in the thyroid, being responsible of thyroids hormone biosynthesis.

Another group of peroxidases is the non-animal peroxidases group which it is divided in three major classes. The first class (Class I) of peroxidases is a group of intracellular peroxidases. Three members of this class are: yeast cytochrome c peroxidase, found in the mitochondria, which serve as a protection mechanism for peroxides; ascorbate peroxidase, which is the main protection and removes hydrogen peroxidase in the chloroplast and cytoplasm in plants; and bacterial catalase, which is responsible for protection of cells under oxidative stress and exhibit both peroxidase and catalase activities. Cytrochrome C peroxidase is an example of a heme containing oxidoreductase that catalyzes a two-electron reduction of hydrogen peroxide to water with concomitant oxidation of two equivalents

of cytochrome C. Phylogenetic analysis has demonstrated that it is obvious that a large diversity in the genes coding for CcPs occurs among fungal genomes. The natural expression of the putative CcP genes from all three subfamilies of CcP is a response to various forms of oxidative stress in the fungal life cycle[11].

As we have presented before the peroxidases come from various organisms and have a very important biological role in nature. When these enzymes are structurally compared with each other some have very similar amino acid sequences while others are different in their amino acid sequences, thus resulting in a low percent of primary sequence homology. But what all these enzymes have in common is a highly conserve tertiary structure. This pattern, where the tertiary structure is more conserved than the primary structure, is rather widespread in many families of enzymes. This structural similarity of heme peroxidases is reflected around the common 10 helical bundle motifs. All peroxidases are heme containing enzymes. **Figure 2** shows the active site of horseradish peroxidase(HRP). HRP is a widely studied peroxidase. In its active site the His 170 is coordinated to the heme iron attaching the heme group to the protein matrix. In the distal side of the pocket we have the His 42, Arg 38 and Phe 41[12]. It is attributed to the distal amino acids, which are directly involved in the reaction of peroxidases with hydrogen peroxide. The distal amino acids interact with the different intermediates of the peroxidase reaction. Farzana and collaborators have found that HRP can be used as a biosensor to sense H_2O_2 in neutral phosphate buffer, providing a wide response range towards H_2O_2 detection with an excellent reproducibility[13]. All peroxidases have a distal and proximal helix loop close to the heme group. The proximal helix contains a His, which is coordinated to the fifth coordination position of the iron in the heme group. This is conserved through most peroxidase and hemoglobins, excluding catalases that provide an example of heme proteins where a proximal Tyr

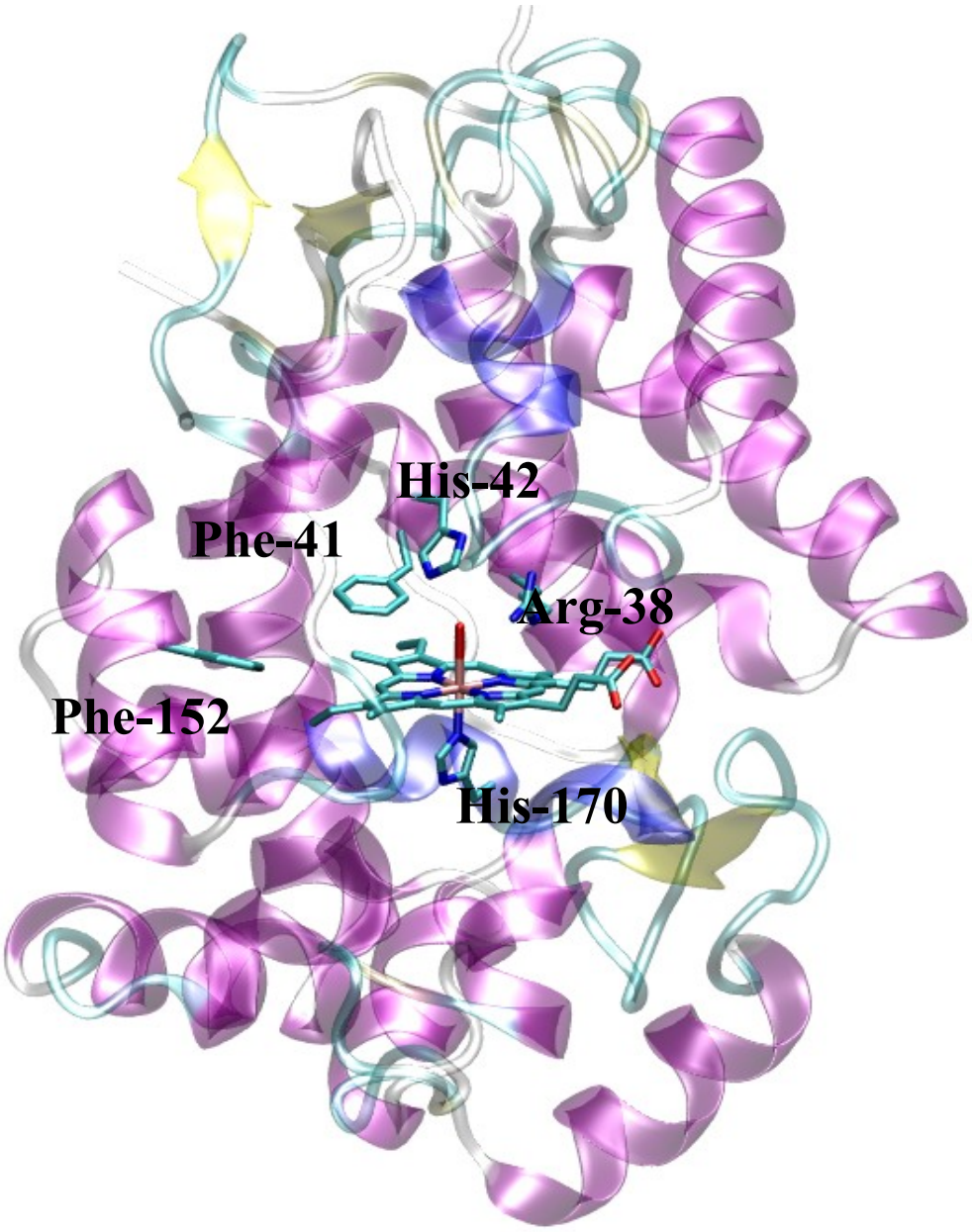

Figure 2: Horseradish peroxidase active site from 1W4Y pdb with His 42, Arg 38, Phe 41, Phe 152 as the distal amino acids and His170 in the proximal position.

residue coordinates to the heme iron. Also cytochrome P450 family is coordinated in the fifth position, by a methionine. Another important member of the peroxidase family is the catalases. Catalases are bi-functional antioxidant enzymes present in different organisms. Almost all know organism use catalase in every organ, and is normally found in high concentrations in the liver. Catalases provide protection against oxidative stress by converting two hydrogen peroxide molecules into water and oxygen. One example of the use of catalases by nature is the use of catalase as a propellant generator used by the bombardier beetle.

The bombardier beetle has two sets of chemicals ordinarily stored separately in its paired glands. The largest of the pairs of storage reservoir contains hydroquinone and hydrogen peroxide, whereas the smallest of pair of the chambers contains catalases. To activate the spray, the beetle mixes the contents of the two compartments, causing oxygen to be liberated from hydrogen peroxide decomposition. The oxygen liberated oxidizes the hydroquinones and also the oxygen acts as a propellant. The structures founded of catalase have revealed an unusually large number of modifications unique to catalases. These modifications are a result of the interaction with reactive oxygen species. Biochemical and physiological characterization of catalases from many different organisms has revealed a surprisingly wide range of catalytic efficiencies, despite similar sequences[14]. These enzymes are very stable and are more resistant to pH, temperature and proteolysis than other enzymes. This is attributed to a very rigid structure that is resistant to unfolding structure.

The mechanism proposed for the reaction of hydrogen peroxide and other ROS with the peroxidase family can be seen in **Figure 3**. This mechanism describing this reaction was initially proposed by Poulos and Kraut[15]. First the hydrogen peroxide enters to the active site and coordinates with the heme iron to make the ferric hydroperoxy complex. These short lived species, then with the assistance of the Histidine (His) in the E7 position, extracts the proton from the oxygen proximal to the

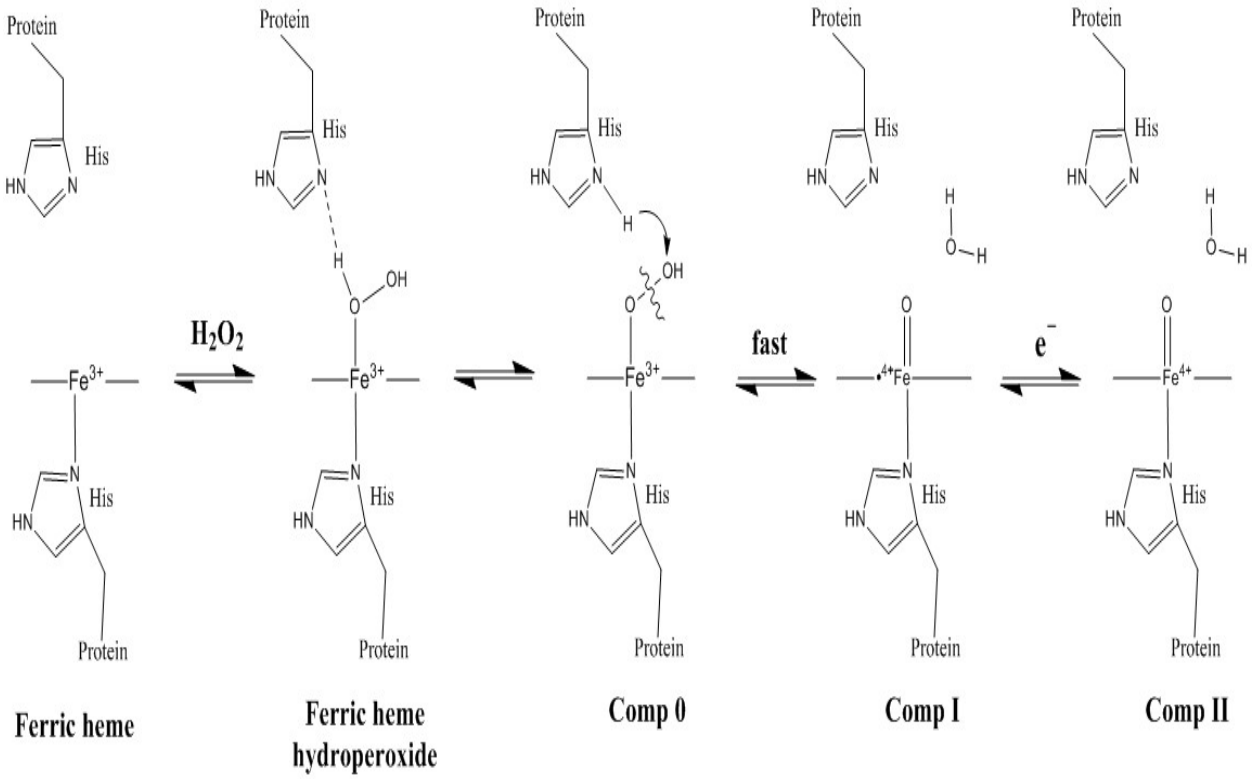

Figure 3: Mechanism proposed for the reaction of peroxidases and hemoglobins with hydrogen peroxide.

heme iron generating in the process the compound 0 specie. Then, the His transfers the hydrogen to the second oxygen in the molecule of hydrogen peroxide. After this, the O-O bond is cleaved, generating compound I species and releasing water. Afterwards, another molecule of hydrogen peroxide interacts with compound I, generating two water molecules in peroxidases, and one water molecule and an oxygen molecule in catalases. For a classic peroxidase, such as HRP, the reaction cycle involves a two-electron oxidation-reduction[16].

The mechanism proposed for the reaction of hydrogen peroxide and other ROS with the peroxidase family can be seen in **Figure 3**. The mechanism describing this reaction was initially proposed by Poulos and Kraut[15]. First the hydrogen peroxide enters to the active site and coordinates with the heme iron to make the ferric hydroperoxy complex. These short lived species, then with the assistance of the Histidine in the E7 position, extracts the proton from the oxygen proximal to the heme iron generating in the process the compound 0 specie. Then, the histidine transfers the hydrogen to the second oxygen in the molecule of hydrogen peroxide. After this, the O-O bond is cleaved, generating compound I species and releasing water. Afterwards, another molecule of hydrogen peroxide interacts with compound I, generating two water molecules in peroxidases, and one water molecule and an oxygen molecule in catalases. For a classic peroxidase, such as HRP, the reaction cycle involves a two-electron oxidation-reduction[16].

This mechanism appears to be part of the catalitic cycles of heme oxygenase, cytochrome p450, catalases, super oxide dismutase and hemoglobins with hydrogen peroxide. Because of the short life of the transient species, it's been difficult to study using spectroscopic techniques especially for the species of ferric hydroperoxy and compound 0. The use of fast spectroscopic techniques like stopped-flow has been used by several research groups. Shintaku et.al. using an optimized stopped-flow device with a microsecond time scale mixing dead time present data of the reaction of HRP with hydrogen

peroxide where the absorption soret band characteristic of compound I was detected, yet no compound O band was detected between the 50-300 μs timescale monitored[17]. However, the bands presented isobestic points, suggesting the presence of a precursor specie to the compound I specie[17].

1.1.3 Myoglobin and hemoglobin reactions with hydrogen peroxide.

The globin family of proteins to which myoglobin (Mb) and hemoglobin (Hb) are part of, are involved in very important biological processes that are diverse, and metabolize important physiological reactions vital to the life of most organisms, from protist to mammals[18]. Some of the known functions are the transport of diatomic molecules, chemical catalysis, and electron transfer. Phylogenetic analysis of the globin family suggests that all globins have evolved from a common ancestor. It was found through phylogenetic analysis that globins are mostly enzymes that transport oxygen, and its function was developed relatively recently through the emergence of multicellular organisms[19].

Mb primary function is oxygen transport in the muscle[20]. Mb is frequently found in muscle cells and gives meat its typical red color. **Figure 4** shows the structure of horse heart met-myoglobin. Over 80% of the polypeptide chain is involved in eight helical segments[21]. Its protein matrix is composed of eight (8) helical motifs compared to ten (10) found in peroxidases. Myoglobin has a heme group in their active site similar to peroxidases. The free heme group binds CO more strongly than oxygen, but Mb is capable of discriminating between both. The mechanism for the reaction of hydrogen peroxide with peroxidases and myoglobin has historical importance. Oxidative processes, which are in many cases enhanced when modifications are introduced, lower the oxygen affinity and can limit the safety of hemoglobins for oxygen-carrying therapeutics. The knowledge of the hemoglobins reaction with hydrogen peroxide can help us to overcome the limit imposed by these reactions in the development of proteins for oxygen carrying therapeutics.

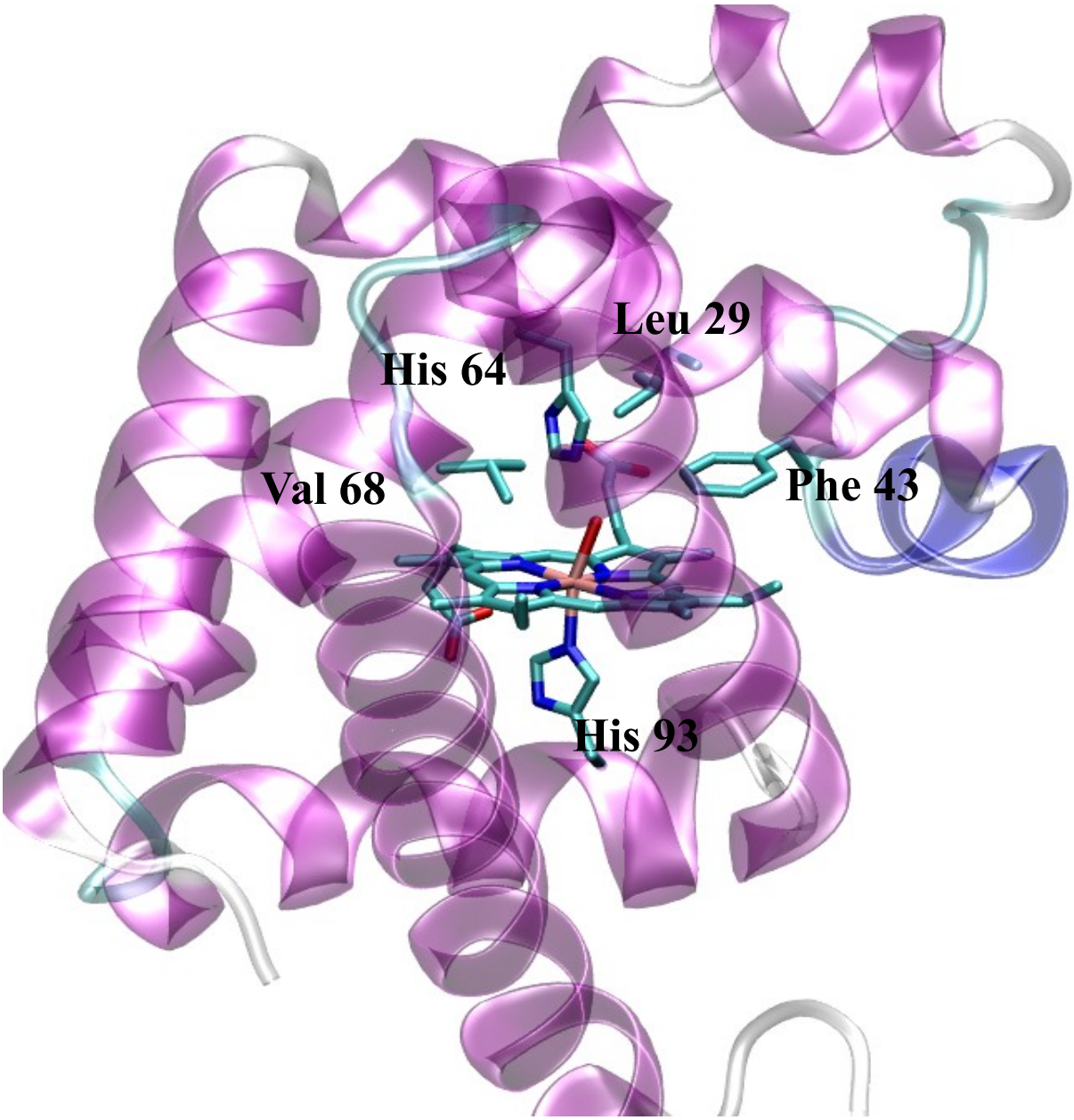

Figure 4: Structure of horse heart metmyoglobin from 1YMB pdb (Evans and Brayer 1990).

Flögel et. al. has suggested that, additionally to the typical function of oxygen carrying capacity of myoglobin, it also act as NO oxidase[5,22]. Through the comparison of mice hearts with and without myoglobin, their data shows that the lack of Mb leads to increased vulnerability of cardiac function to oxidative challenge either pharmacologically induced or endogenously generated. These results suggest that Mb is a key element influencing redox pathways in cardiac muscle to functionally and metabolically protect the heart from oxidative damage[5,22]. In the reaction of met-myoglobin with H_2O_2, a protein derivative similar to compound I in peroxidases is formed, capable of oxidizing a wide arrange of substrates[23]. Ferric myoglobin and hemoglobin undergo a two-electron oxidation in its reaction with H_2O_2. In the mechanism proposed by Poulos and Kraut[15], this reaction occurs in multiple steps. **Figure 5** shows the mechanism proposed for the reaction of H_2O_2 with HbI of the clam *Lucina pectinata*[24]. Similar to peroxidases and myoglobin, HbI forms ferryl species upon reaction with H_2O_2. But HbI showed the ability to stabilize the heme ferryl $(Fe^{IV}=O)^{\cdot+}$compound I a thousand times more than Mb through its unusual heme pocket configuration (Gln64, Phe43, Phe29, and Phe68)[25]. These heme ferryl-oxo derivatives play an important role in the design of the heme proteins substitutes of natural hemoglobin[26,27]. The compound I species have been characterized for multiple heme proteins, but its theoretical precursor is still in debate. On previous studies, it was found that compound I was formed within the dead time of stop-flow instruments[18]. This means that it is a precursor that cannot be measured in the timescales of rapid mixing techniques. Kühnel et. al., through the use of cryoradiolitic reduction, the peroxo-anion species was formed and then protonated to yield compound 0[9]. They have found that compound 0 is present in the ferric low-spin doublet ground state and is characterized by a long O-O bond length of 1.5 Å and a Fe-O bond distance of 1.8 Å, which is also observed in the crystal structure[9]. Binding kinetics of many ligands with myoglobin has been determined using stopped flow technique or laser flash photolysis. Unlike conventional chemical oxidations performed with mixing methods that have a dead mixing time of 1 ms, the photochemical approach produces transient species

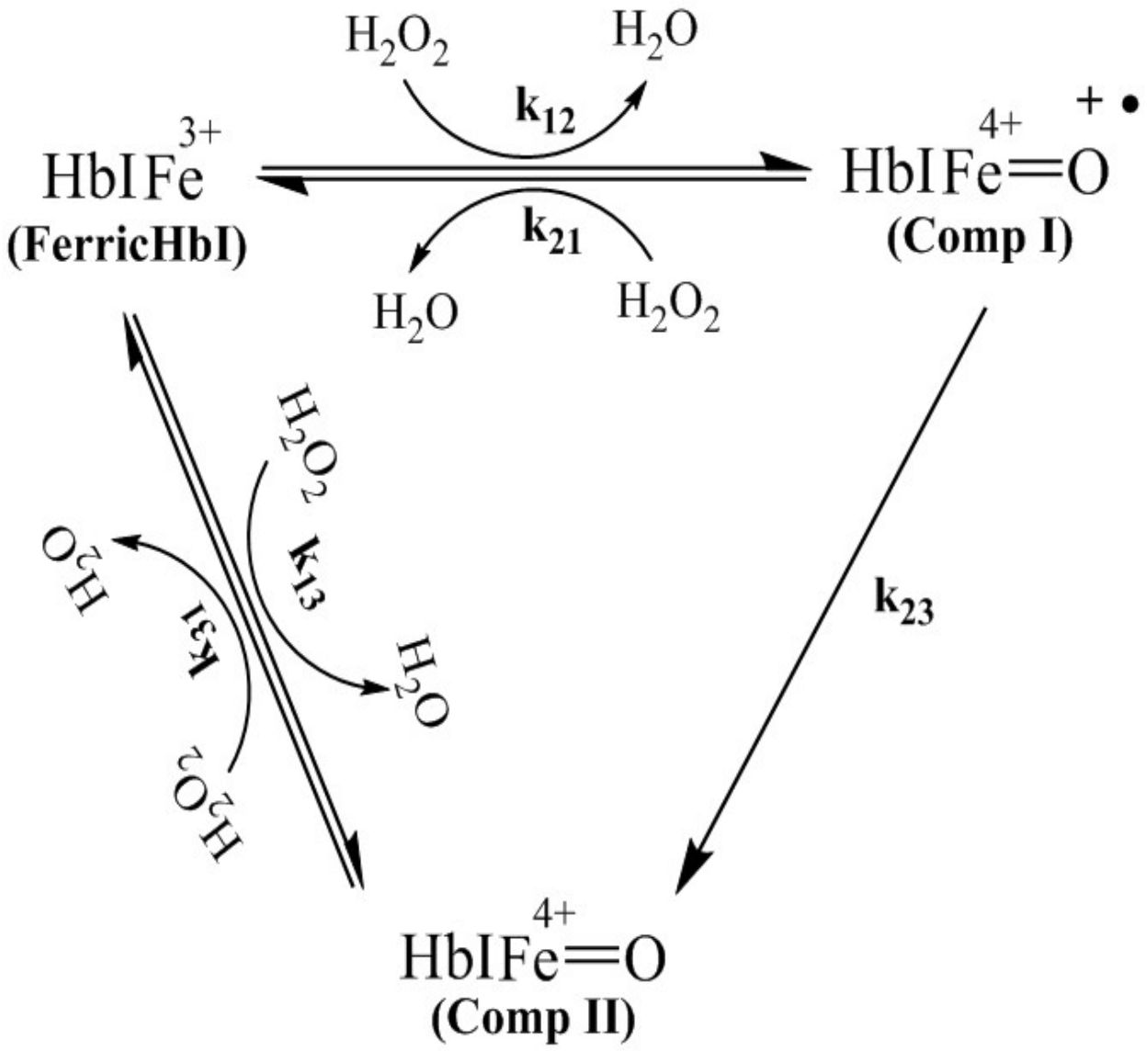

Figure 5: Reaction mechanism proposed by for the reaction of Lucina pectinata HbI with hydrogen peroxide[24].

instantly, and direct measurement of this accumulated transients could be relatively straightforward[28]. The characteristic pocket distal amino acids found in *Lucina pectinata,* which has Gln instead of the typical His, represents a good model for comparison of the role of the E7 position amino acid in the formation of the sulfheme specie.

1.1.4 Hydrogen sulfide biological relevance

To understand the biological relevance of hydrogen sulfide (H_2S) first we have to picture it as an available molecule in the body. Recent investigations suggest an important physiological and pathological role of H_2S in the human body. H_2S is enzymatically generated in the vasculature, heart, liver, kidney, brain, nervous system, lung, airway tissues, and many other tissues in the body. Another recently proposed source of H_2S is from thiosulfate. Recent study presents a thiosulfate contribution to the H_2S signaling under hypoxic conditions. Likewise, Olson and collaborators suggest that not only thiosulfate is a source of H_2S production, but also serves as means of recycling sulfur and thereby conserving biologically relevant thiols[29]. The key role of H_2S in health and disease is clearly borne out by the correlations found to exist between low levels of plasma/tissue endogenous H_2S and/or H_2S-generating enzymes in the presence and progression of adiposity, marked endothelial dysfunction/insulin resistance, hypertension, hyperhomocysteinemia, diabetes, exacerbated cardiac injury following ischemia-reperfusion injury, Alzheimer disease, cirrhosis, chronic kidney disease, GI tract irritation, asthma, wound healing and cancer[30]. Recently, it has been found that the level of H_2S concentration in maternal placenta could influence the development of preeclampsia in women. However, endogenous H_2S is required for healthy placental vasculature, and a decrease in cystathionine γ-lyase (CSE)/H_2S activity may contribute to the pathogenesis of preeclampsia.[31] Nonetheless, exogenous exposure to H_2S or compounds which could exogenous generate H_2S are related to the

development of sulfhemoglobinemia.[32–35] This type of anemia results from the reaction of hemoglobin in the presence of H_2S with H_2O_2 or other reactive oxygen specie. The final product of this reaction results in a heme group modification is named sulfheme.

1.1.5 Sulfheme specie formation

Sulfheme specie shown in **Figure 6** is a chromophore associated with heme modification in myoglobin (Mb), hemoglobin (Hb), and some peroxidases and catalases. Formation of sulfheme arises from the reaction of these particular heme proteins with hydrogen sulfide (H_2S) or other thiol compounds in the presence of hydrogen peroxide (H_2O_2) or oxygen (O_2). Sulfheme have been associated with high concentrations of H_2S and various drugs such as acetanilide, metoclopramide, phenacetin, dapsone, sulfonamide containing drugs, cimeti-dine, paracetamol, ibuprofen, and naproxen.[31,32,35,36] Notably, the formation of sulfheme complexes at moderate levels and their destruction by the physiologic turnover of red blood cells has been considered to be the major pathway for H_2S degradation in humans.[30] The presence of these sulfheme derivatives has also been used as a marker of endogenous H_2S synthesis.[36,38]

The concentration of O_2 required to saturate half of the sulfmyoglobin (sulfMb) molecules is approximately 2500 times higher than that for the native protein, indicating a much lower O_2 affinity for the former.[39,40] Remarkably, catalases and peroxidases having a distal (ligand-binding site) His in the active site also generate sulfheme derivatives that exhibit a lower affinity toward O_2.[41] Sulfheme derivatives have a sulfur atom incorporated into pyrrole B (**Figure 6**), with a characteristic optical band around 620 nm.[42–45] The displacement of this band depends on heme Fe oxidation and ligation states, as well as on the type of the sulfheme isomer.[39,46–48]

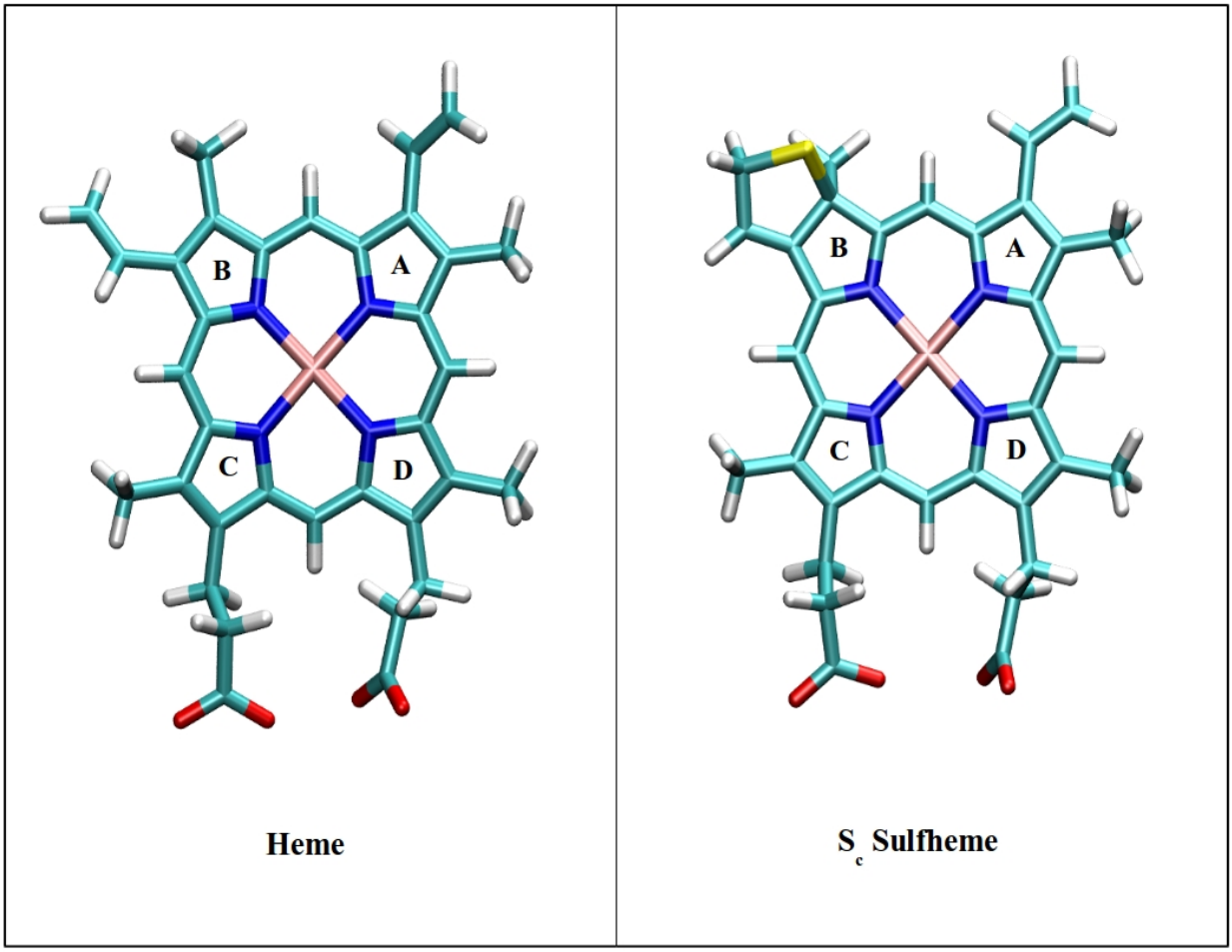

Figure 6: Typical protoporphyrin IX heme group vs sulfheme modified heme group.

Considerable research efforts have been directed toward the structural and mechanistic formation of these sulfheme proteins. Proton NMR studies of several sulfMb−cyano complexes revealed that there are at least three isomeric forms of the chlorin structure that may affect O_2 affinity,[43,48] named S_A,S_B, and S_C, followed by the abbreviation for the heme-containing protein (**Figure 7**). Each sulfheme isomer has different physicochemical properties and hence a different reactivity and stability pattern.[43,47] As such, the isomer distribution can be controlled by changes in pH, temperature, and protein concentration. The NMR spectra of all isomers showed symmetry reduction of the prosthetic group and alteration of the π conjugation of pyrrole B.[47] The S_A structure is an episulfide formed across the C3−C4 double bond (**Figure 7**), which is rapidly reconverted to the protoheme when the heme is extracted from the protein, whereas S_B is characterized as a "ring-opened episulfide", and finally, S_C is the thiochlorin structure.[43,44,49,50]

S_AMb (the S_A form of Mb) is converted into both S_BMb and S_CMb, although conversion from S_BMb to S_CMb has not been observed, indicating that S_AMb could be the precursor of both sulfheme derivatives.[43,44] S_CMb is the most stable isomeric form when a vinyl group is bonded to C4 (**Figure 7**) and appears to predominate under physiological conditions, implying that this compound may account for the reduced O_2 affinity in sulfMb.[48,51]

1.1.6 Density Function Theory

The organization, interaction and movement of electrons to distinguish the internal structure of atoms and molecules is important in chemistry. Several electronic structure theories try to describe how the electrons are arranged inside them. Some examples of electronic structure theories proposed are Hartree-Fock[52,53], configuration interaction (CI)[54], coupled cluster [63], Møller-Plesset perturbation theory[55], quantum Monte Carlo[56], and density functional theory (DFT)[57,58]. The main purpose of these

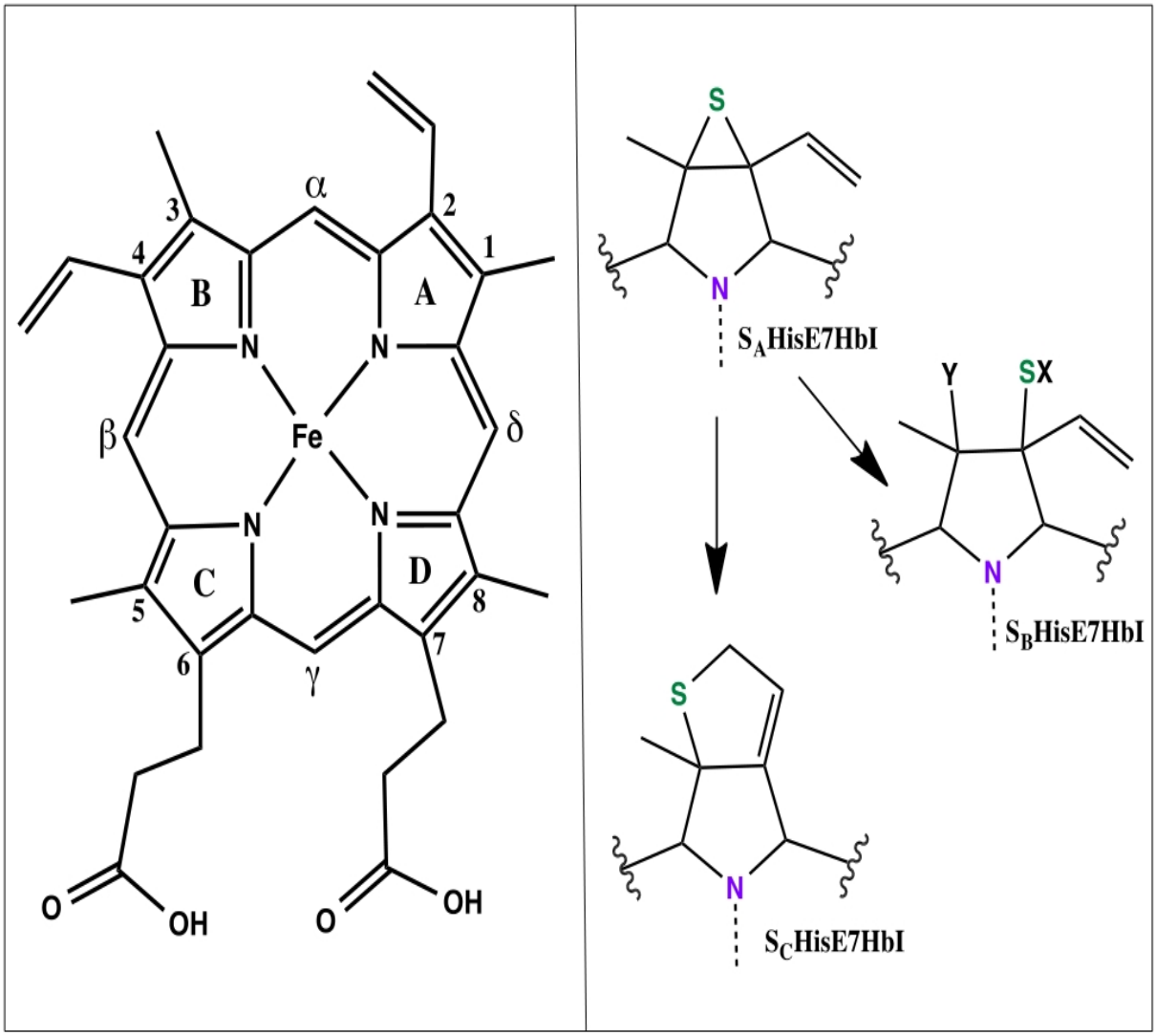

Figure 7: (left) Depiction of protoporphyrin IX which binds to HbI viewed from the distal side of heme. Important carbons are labeled numerically and with symbols while the pyrroles are labeled alphabetically (right) Sulfheme derivatives (SA, SB, and SC) showing the experimentally determined transformation pathways. From http://dx.doi.org/10.1021/acs.jpcb.6b02839

theories is to achieve the ground state energy calculation of a many electron system found in molecules. From the several electronic structures theories, the density functional theory (DFT) can determine the ground state energy in an accurate and efficient manner by representing the many electron system as a function of the electron ρ (r) density and not via its many-body wavefunction.

DFT is mainly imputed to Hohenberg, Kohn, and Sham in 1964–1965[57,58], but DFT theoretical framework can be trace back to Thomas[59], Fermi, and Dirac[60]. Thomas, Fermi, and Dirac were the first ones to suggest a theory for electronic structure description using only the system total electron density ρ(r). Though this approach was very simple and roughly estimates of atomic properties, and it failed to describe the bonds between atoms which is important in chemistry. Although Thomas, Fermi, and Dirac theory was not useful for chemical description, but it served as an foundation to Hohenberg, Kohn, and Sham DFT theory[61]. In Hohenberg and Kohn (HK) all ground state properties can be known from knowing the total electron density ρ[57]. The HK second theorem establishes that there is an universal functional of the density who's global minimum value is the exact ground state energy of the studied system. The ground state density minimizes this functional[57,58]. The universal functional is expressed as shown next

$$F(\rho)=T_0(\rho)+J(\rho) \tag{1.1}$$

where $T_0(\rho)$ first term is the total kinetic energy for non interacting particles which is equal to

$$T_0(\rho)=-1/2\sum_i \int \psi_i^*(\rho)\nabla^2\psi_i(\rho)d\rho \tag{1.2}$$

and the $J(\rho)$ is the classical Coulombic energy of electrons

$$J(\rho)=1/2\iint\frac{\rho(1)\rho(2)}{r_{12}}d_1d_2 \tag{1.3}$$

To adjust and include the energy of interacting particles the exchange-correlation energy (E_{XC}) was added to the universal functional. The E_{XC} have components of kinetic and potential energy. The universal functional on equation 1.1 with the E_{XC} included will be seen next

$$F(\rho)=T_0(\rho)+J(\rho)+E_{xc}(\rho) \tag{1.4}$$

To give a precise description of a condensed matter system it is important to have an accurate E_{XC} functional[61]. The most widely used approximation to calculate the E_{XC} are the local density aproximation (LDA) and the general gradient approximation (GGA). Moreover E_{XC} can be expressed as follows

$$E_{XC}=E_X+E_C \tag{1.5}$$

in which we divide th E_{XC} into exchange and correlation parts. The E_X depicts the exchange energy of the Slater determinant of the KS orbitals, and the E_C portrays anything else from particle interactions[62]. Because of the integration form of E_X and E_C, $E_C < E_X$, therefore the unknown correlation effects are moved into an even smaller part of the KS total energy[62]. The the local density aproximation (LDA) is simple model proposed by Kohn and Sham[58] to describe the E_{XC}. A general E_{XC} LDA equation is

$$E_{xc}^{LDA}=\int\rho(r)e_{XC}^{UEG}(\rho)dr=\int\rho(r)(-\frac{3}{4}\sqrt[3]{\frac{3\rho(r)}{\pi}})dr \tag{1.6}$$

where $e_{XC}^{UEG}(\rho)$ is the E_{XC} for uniform electron gas density (UEG). The LDA for pure exchange is shown in equation 1.7

$$E_X^{LDA} = -\frac{3}{2}\left(\frac{3}{4\pi}\right)^{1/3} \int \left(\rho_\alpha{}^{4/3}(r) + \rho_\beta{}^{4/3}(r)\right) dr \tag{1.7}$$

The E_C correlation energy is calculated at two scenarios. It is calculated for the regions were the density limits are low and high. This is related to an infinite weak and infinite strong correlation. The form is presented in the next to equations[63].

$$E_C^{High\,density} = c_0 \ln r_s - c_1 + c_2 r_s \ln r_s - c_3 + \ldots \left(r_s \to 0\right) \tag{1.8}$$

$$E_C^{Low\,density} = -\frac{d_0}{r_s} + \frac{d_1}{r_s^{3/2}} + \ldots \left(r_s \to \infty\right) \tag{1.9}$$

Accurate values for the correlation energy at intermediate density values, a quantum Monte Carlo (QMC) simulations for the UEG is needed. In practice most LDA interpolate the values for the correlation energy from QMC simulations while achieving the exactly known limiting behavior. Some of the different approaches to calculate the correlation energy at intermediate density values for local density approximations are Vosko-Wilk-Nusair(VWM), Perdew-Zunger (PZ81), Cole-Perdew(CP) and Perdew-Wang (PW91)[61].

The GGA functionals can be seen as an adjustment of the LDA presuming an a infinite order gradient expansion[62].

Another option for E_{XC} functional is to include a hybrid functional into E_{XC} functional where a part of the exchange is replaced with a nonlocal Hartree-Fock exchange. An example of this is the next one proposed by Becke[66].

$$E_{XC}^{B3PW91} = E_{XC}^{LDA} + a\left(E_X^{HF} - E_{XC}^{LDA}\right) + b\,\Delta E_X^{B88} + c\,\Delta E_C^{PW91} \tag{1.10}$$

where a = 0.20, b = 0.72, c = 0.81. There are a variety of E_{XC}functionals which help to computationally study the chemical nature of molecules through the use of DFT with accuracy and computational efficiency.

1.2 Methods

1.2.1 Model construction

Atomic coordinates for construction of the HisE7HbI model were obtained from the 1.9 Å resolution X-ray structure of Hemoglobin I from *Lucina pectinata* with H_2S bound to the Fe atom (PDB entry *1moh*)[67]. Model construction was performed with CHARMM version c36b2[68]. Glu64 was mutated to a neutral histidine residue. The proximal oxygen of H_2O_2 replaced the sulfur atom bound to Fe. The final solvated system contained ~20,000 atoms.

The CHARMM27 force field[69] with CMAP corrections[70] and the TIP3P water model[71] were used to describe the protein and solvent, respectively. The remaining atoms were described based on a CHARMM modified force field for the heme group[72]. One thousand steps of energy minimization were performed using the steepest descent (SD) algorithm. Periodic boundary conditions were applied, and the Particle Mesh Ewald method[73] (~1 grid point $Å^{-3}$) was used to describe long-range electrostatic effects. The SHAKE algorithm was used to constrain all bonds to hydrogen[74]. Because molecular dynamics (MD) simulations of this heme protein using force field produced unphysical distortions in the planarity of the heme, therefore, just the energy minimized structure was used as the initial structure for subsequent simulations with a hybrid QM/MM method.

1.2.2 Parameterization Method 6 PM6/MM Molecular Dynamics

Hybrid QM/MM simulations were performed with pDynamo version 1.5.51 The QM region was composed of the entire heme, the Arg99, the proximal His96, and H_2O_2 (**Figure 8**) for a total of 108 QM atoms using the PM6 method[75]. Arg99 forms hydrogen bonds with one of the propionate groups of heme. All residues were modeled in their canonical protonation states. A force switch was used to describe the electrostatic and van der Waals interactions, with an inner cutoff of 8.0 Å and an

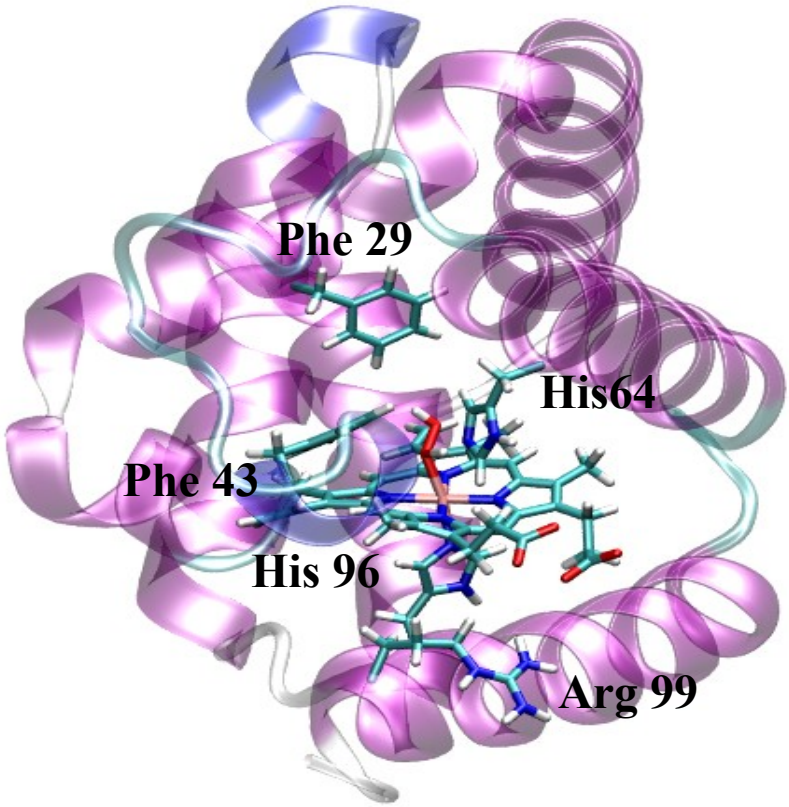

Figure 8: Depiction of lucina pectinana HbIGlnE7His mutant with the entire heme, the distal His 64, Phe 29, Phe 43, the proximal His96, the Arg99,and H_2O_2.

outer cutoff of 14.0 Å. Hydrogen link atoms were used to describe the QM/MM boundary, and these were automatically placed 1.0 Å away from Cβ along the Cα-Cβ bond axis for side chains in the QM region by pDynamo. The QM region multiplicity was set to the lowest energy spin state (doublet). The MM region was described by the same CHARMM force field mentioned previously and will be referred to as PM6/MM. The systems were simulated for 3 ps (1 fs time-step), during which the velocities were scaled every 100 steps until a temperature of 300 K was reached. The systems were then simulated for 1.4 ns in the NVT ensemble under periodic boundary conditions. The dimensions of the system were 79.7 × 67.9 × 60.0 $Å^3$. The final structure was used for subsequent investigations with DFT/ MM methods. Visualization of the structures and analysis were performed with the visual molecular dynamics (VMD) program[76].

1.2.3 DFT/MM investigations of sulfheme formation

A water molecule that penetrated into the active site was replaced by H_2S in order to model a mechanism of sulfheme formation. This H_2S molecule was always treated within the QM region with Lennard Jones parameters obtained from the literature[77]. The hybrid DFT/MM calculations were performed using pDynamo interfaced with the ORCA program version 3[78]. All water molecules with an oxygen atom greater than 30 Å from the Fe atom were deleted to create a spherical boundary model of the system, a common approach that has been shown to yield good accuracy in investigations of enzymatic reactions[79,80]. The entire enzyme was contained within the 30 Å solvent sphere with an atom count of ~11,300. All water molecules and protein residues containing an atom greater than 20 Å from the Fe atom of the heme were held fixed. The QM region was composed of the entire heme group, the proximal His96 that binds to the Fe atom, the distal (ligand-binding side) His64, three distal phenylalanines (Phe29, Phe43, and Phe68), H_2O_2, and H_2S for a total of 149 QM atoms. The three distal phenylalanines create a hydrophobic “cage” that surrounds any bound ligand.

The QM region during the PE scans was described with the gradient-corrected BP86 functional[64,81,82] with an Ahlrichs split-valence basis set augmented with polarization (SVP)[83,84]. The resolution-of-the-identity (RI) or RIJCOSX approximation with the SVP/J or TZV/J Coulomb fitting basis was applied in all cases when pure or hybrid functionals were used, respectively[85,86]. The Stuttgart-Dresden ECP10MDF energy-consistent small-core effective core potential and basis set were used to describe Fe[87,88]. Hereafter, we refer to the combination of this DFT approach and the CHARMM molecular mechanics potential as DFT_1/MM. Single-point DFT/MM energies were computed with the B3PW91 functional[89,90] and the Ahlrichs TZV(P) basis set for the QM region. Hereafter, we refer to the combination of this DFT approach and the CHARMM molecular mechanics potential as DFT_2/MM. The calculations were performed in the doublet, quartet and sextet states.

The initial structure for the PE scans was obtained from a PM6/MM simulation snapshot, followed by a 100-step DFT_1/ MM geometry optimization using the SD algorithm. The proton transfer from the proximal oxygen of H_2O_2 to His64 to form Cpd 0 was investigated by performing a series of constrained geometry optimizations along a reaction coordinate defined as the mass-weighted distance difference between Nδ(His64)-H(H_2O_2) and O(H_2O_2)-H(H_2O_2) divided into 21 windows. A harmonic restraint potential of 475 kcal $mol^{-1}Å^{-2}$ was used on this and all the other reaction coordinate PE scans while each window was always minimized for 50 steps using the SD algorithm. The formation of Cpd II, H_2O and the thiyl radical was investigated by performing a series of constrained geometry optimizations along the hydrogen peroxide O-O bond distance divided into 24 windows. DFT_2/MM single points were then performed on the DFT_1/MM-optimized structures to obtain a more accurate PE profile. Thiyl radical insertion into various points within the heme macrocycle was investigated by performing a series of constrained geometry optimizations along a reaction coordinate defined as the distance between S(HS)-Cx(macrocycle). These explorations of thiyl radical insertion mechanisms were computationally demanding, requiring thousands of geometry optimization steps, and so were

performed using the more efficient DFT_1/MM method. We report only on the additions to C2 (pyrrole A) and C3 (pyrrole B) (**Figure 7**) because they were the only ones shown to be favorable and sufficient to demonstrate the cause of specificity for sulfheme formation on pyrrole B. Surprisingly, the products of thiyl radical addition to C2 or C3 were only metastable. Once a hydrogen bond forms between the thiol and the intermediate water molecule (which is also hydrogen bonded to $Fe^{(IV)}$=O), DFT_1/MM PE scans along the reaction coordinate for (1) proton transfer from the thiol to the intermediate water molecule and (2) from the water molecule to $Fe^{(IV)}$=O and (3) from His64 to $Fe^{(IV)}$=O all occur without any PE barrier, leading to the formation of S_AHisE7HbI, the three-membered episulfide ring

Sulfheme derivative S_AHisE7HbI (**Figure 7**, three-membered ring structure) was further geometry-optimized for 200 SD steps by the DFT_1/MM method and then for 50 additional SD steps by the DFT_2/MM method. The transformation from S_AHisE7HbI to S_CHisE7HbI (three- to five-membered ring structure) was investigated through a DFT_1/MM PE scan using the distance difference between S−C4(pyrrole B) and S− C(terminal vinyl) as a reaction coordinate. Sulfheme derivative S_CHisE7HbI was further geometry-optimized for 200 SD steps with the DFT_1/MM method and then for 50 additional SD steps with the DFT_2/MM method. Spin-density plots and structural representations were created with VMD version 1.9[76].

1.2.4 Mössbauer Calculations

The Mössbauer parameters, ΔE_q (quadrupole splitting) and δ_{Fe} (proportional to the electron density around Fe) were calculated using the ORCA program, and a previously developed calibration method[91]. δ_{Fe} is calculated using the following formula: $\delta_{Fe} = \alpha(\rho_0 - C)\beta$, where α, β and C were determined by linear regression fit to experimental data with values of -0.298, 1.118 and 11580 respectively. The calculations used the hybrid functional B3PW91 with the Ahlrichs TZV(P) basis set and the DFT_2/MM geometry optimized structures.

1.3 Results and Discussion

1.3.1 PM6/MM MD Simulations

The PM6/MM MD simulation of HisE7HbI in the doublet state resulted in trajectories with only minimal heme distortion (**Figure 9**, average root- mean-square deviation (rmsd) = 0.36 ± 0.04 Å), without the addition of artificial restraints. MM MD simulations without restraints on the heme resulted in severe distortions of the heme from planarity. In addition, attempts to geometry- optimize such structures with DFT/MM methods in the doublet state result in the unpaired electron being delocalized over the heme instead of correctly centered on the Fe(III) atom. In addition, these severe distortions could propagate to other parts of the protein, creating channels for water penetration where none exist. The PM6/MM simulations (**Figure 9**, average rmsd = 0.94 ± 0.13 Å) did not show these discrepancies. Only minimal deviation of the heme from planarity is observed, even in the crystal structure of HbI[21,67,92].

The most drastic deviation in the heme (rmsd = 0.58 Å) results from the γ-meso carbon fluctuating above the plane of the heme, with an adjacent δ-meso carbon fluctuating below the plane (**Figures 7** and **9**). The γ-meso carbon is located between the propionates of the heme, which are exposed to bulk solvent and have larger fluctuations than the rest of the heme. Thus, the fluctuations of the propionates likely propagate to this part of the heme. Although the PM6/MM method is not appropriate for investigating heme chemistry, the method may be used to accurately simulate the structural dynamics of heme-containing proteins on the nanosecond time scale in the doublet state.

Most interestingly, the simulations reveal the penetration of a single water molecule through what has been termed the Xe4 pocket[93–95] by a gating motion of Phe29 (the B10 residue). The water molecule equilibrates to a location proximal to the site of sulfur insertion (**Figure 10**). This water molecule that enters the active site is one of the 97 identified in the electron density maps[67]. This water

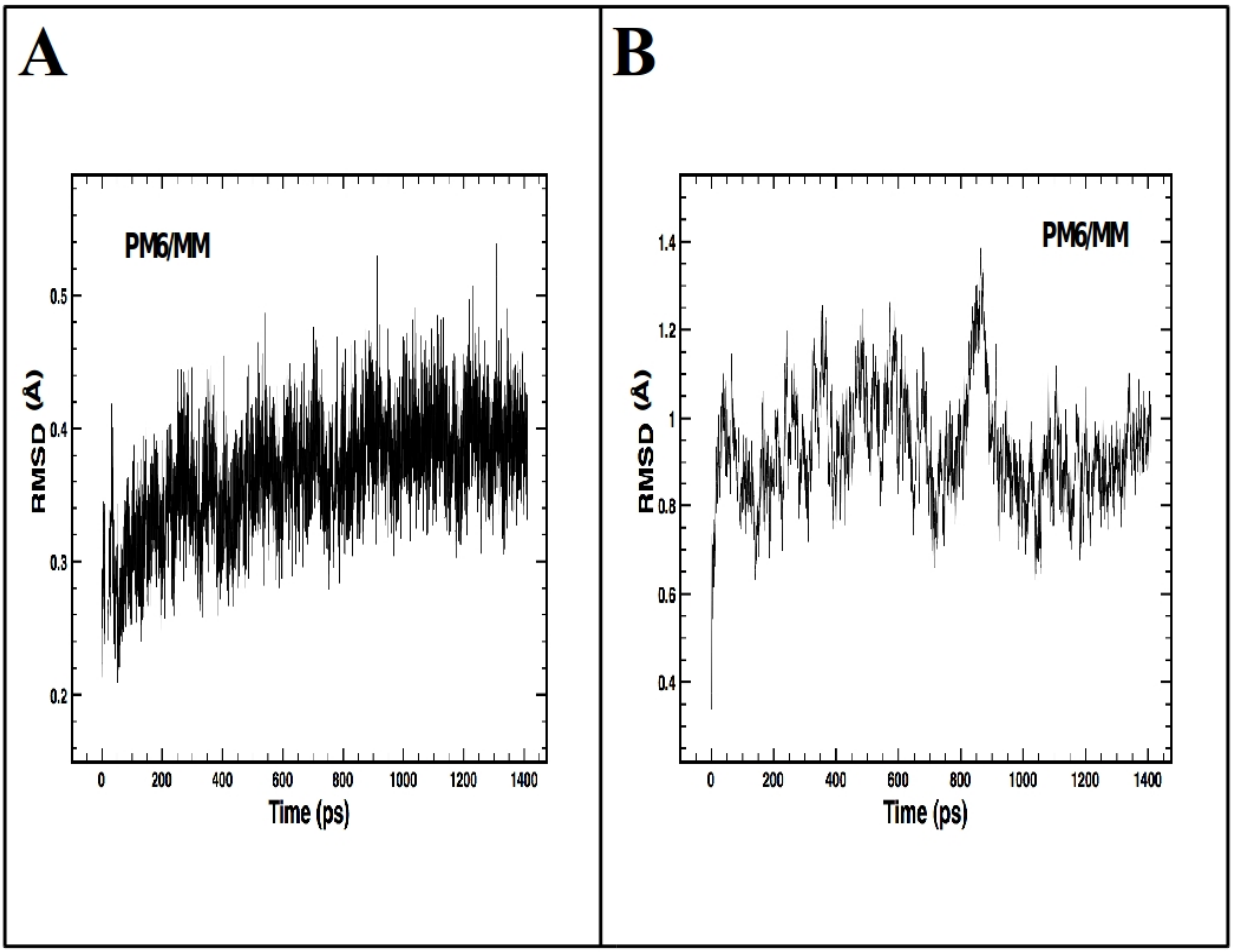

Figure 9: **(A)** *Root mean square deviations in the coordinates of the heme (left) and in the Cα of the protein* ***(B)*** *compared to those in the model determined from X-ray crystallography*[96]*. From* http://dx.doi.org/10.1021/acs.jpcb.6b02839

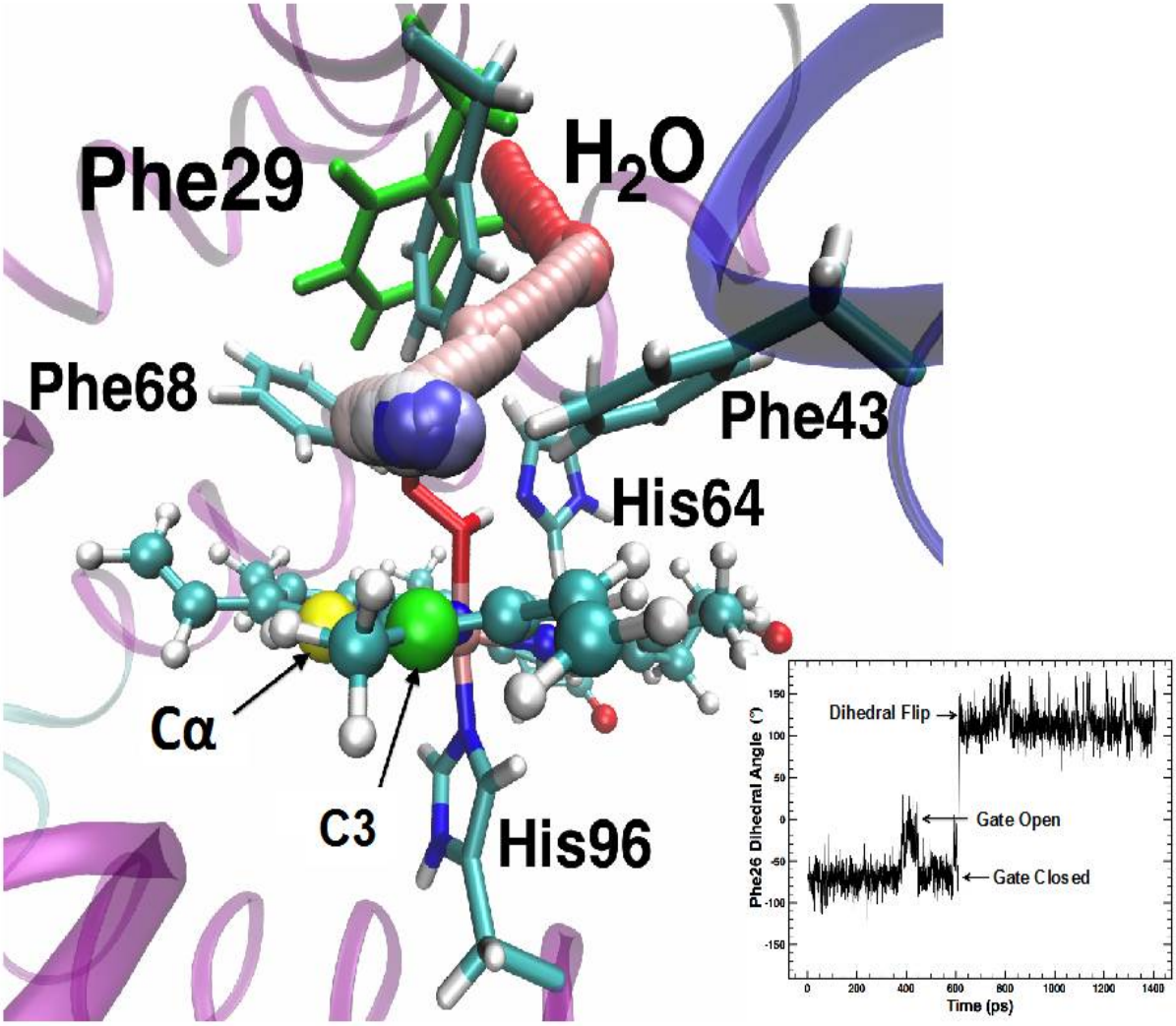

Figure 10: Representation of the HisE7HbI active site showing the progression (from red to blue) over 1.4 ns of a water molecule through Xe4 hydrophobic tunnel caused by the gating motion of Phe29 (closed state depicted in green, open state in aqua). ***(inset)*** *Time series plot showing the side chain dihedral angle of Phe29 going from closed to open and finally a complete dihedral rotation[96]. From* [*http://dx.doi.org/10.1021/acs.jpcb.6b02839*](http://dx.doi.org/10.1021/acs.jpcb.6b02839)

molecule occupies a hydrophobic pocket and is hindered from accessing the active site by Phe29. However, a change in the Phe29 Cα−Cβ−Cγ−Cδ dihedral at around 370 ps opens up a passage to the active site where the water molecule then acts as the acceptor and hydrogen bonds with bound H_2O_2. The water molecule then approaches closer to the heme at around 430 ps and equilibrates in this general location while remaining hydrogen bonded to H_2O_2.

A change in the Phe29 dihedral around 490 ps closes the passage once again. The Phe29 side chain ultimately undergoes a flip, demonstrating the significant conformational freedom available to side chains within the active site. No other water molecules penetrate the H_2O_2 bound active site during the simulation through this or any other route. Experiments performed on sperm whale Mb and neuronal Hb from *Cerebratulus lacteus* demonstrated that the dominant pathway was through the E7 gate[95]. Opening and closing of the E7 gate would be defined by fluctuations of His64 that allow water molecules from the adjacent bulk solvent to penetrate the active site. However, the MD simulations suggest that once H_2O_2 is bound in the active site of HisE7HbI the strong hydrogen bonding of the proximal hydrogen of H_2O_2 with His64 effectively keeps the E7 gate closed on the simulation time scale. MD simulations with classical force fields on Mb's and Hb's indicate that passage through the HisE7 gate is a minor route though this result could be due to inaccuracies in the force field[97,98].

Although both HisE7HbI and Mb are in closer proximity to the bulk solvent than horseradish peroxidase, cytochrome c peroxidase, and P450s, the active sites are much more hydrophobic, primarily due to the lack of a distal Arg residue. H_2S, which is less polar than H_2O (dipole moments: H_2S = 0.97 D, H_2O = 1.85 D), may be even more likely to traverse the Xe4 hydrophobic pocket. Interestingly, the rate of sulfMb formation decreases 250 fold at basic pH values, at which the predominant species is the hydrosulfide anion, HS^- [99]. This rate decrease may arise, in part, because HS^- is less likely to enter the hydrophobic active site of Mb, most Hb like HisE7HbI, through any of

the hydrophobic channels. Therefore, these PM6/MM simulations provide, in part, an explanation for why the site of sulfur insertion is on the side of the heme removed from bulk solvent. Interestingly, alkyl radicals react with the more solvent-exposed γ-meso carbon in Mb[100], clearly indicating that auto catalytic modifications of heme proteins[101] will be a function of the ligand-binding path.

1.3.2 Structure of H_2O_2 Bound to HisE7Hb1 and Cpd 0

DFT_2/MM PE scans of proton transfer from H_2O_2 to His64 show a minimum for the proton located on His64 (Cpd 0) in the doublet state but located on H_2O_2 for both the quartet and sextet states (**Figure 11**). The minimum energy structures for the quartet and sextet states are 1.9 kcal mol^{-1} lower in energy than that of the minimum energy structure for the doublet state. During these calculations, H_2S was not hydrogen bonded to H_2O_2, showed only minor movements during the proton transfer, and, from this position, most likely had little effect on the results. This admixture of spin states with similar energies in the resting state is similar to that observed in the electron paramagnetic resonance spectra of HRP[102].

These PE scans suggest that formation of Cpd 0 occurs through a spin-crossing event, moving from the lowest energy quartet/sextet state to the doublet state, with a barrier of ~4 kcal mol^{-1}. Because the exact nature of this spin-crossing event is not critical to our investigation, it was not investigated further. The existence of this barrier to the formation of Cpd 0 suggests that a proton/hydrogen donating molecule entering the active site would be most likely to encounter a Fe(III)− H_2O_2 resting state. When H_2S hydrogen bonds with the distal oxygen of H_2O_2, the lowest energy structures are not altered except for the sextet state. In the sextet state, hydrogen bonding between H_2S and H_2O_2 results in the formation of Cpd 0 (i.e., the proximal proton on H_2O_2 is transferred to His64), as shown in **Figure 11**.

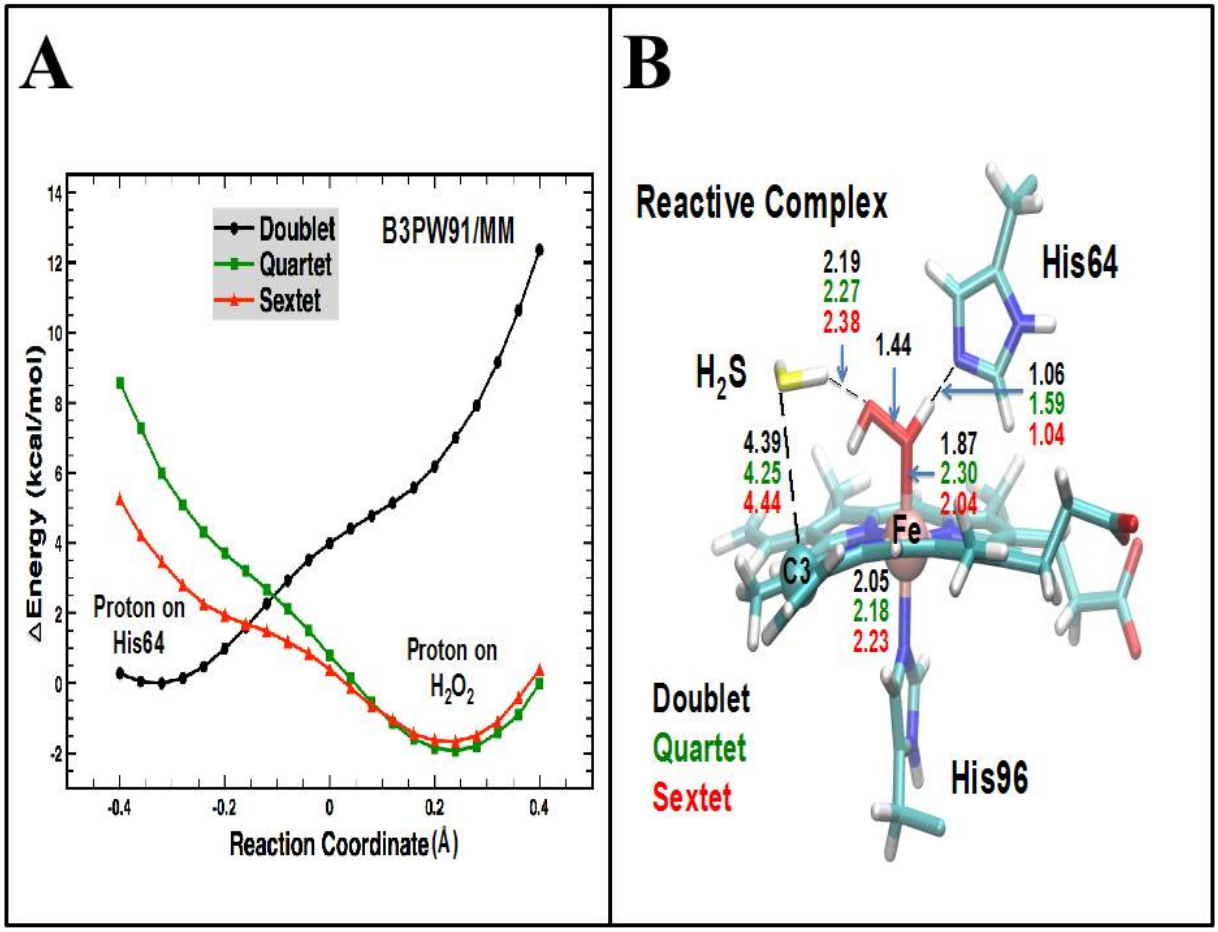

Figure 11: ***(A)*** *DFT_2/MM minimum energy paths for proton transfer from H_2O_2 to His64 using geometries optimized with the DFT_1/MM method. The reaction coordinate is the mass weighted distance difference between His64N--H(proximal) and O-H(proximal).* ***(B)*** *DFT_2/MM geometry optimized structures of the reactive complex in all three spin states. The H_2O_2 O-O bond length is 1.44 Å for all three spin states[96]. From http://dx.doi.org/10.1021/acs.jpcb.6b02839*

1.3.3 Formation of the Thiyl Radical and Cpd II.

DFT_2/MM PE scans using the H_2O_2 O−O bond distance as a reaction coordinate were used to investigate possible mechanistic routes to the formation of a reactive sulfur moiety. The complex, modeled on the results of PM6/MM MD simulations (see the **Method**), is very different from the model used in other theoretical studies investigating the role of water molecules in HRP catalysis[103,104]. In those studies, a water molecule assisted the peroxidase activity by positioning between HisE7 and H_2O_2 whereas in our studies, the analogous H_2S molecule is positioned in the space between H_2O_2 and the interior of the heme active site. The lowest DFT_2/MM energy structure for the reactant complex indicates that hydrogen bonding between H_2S and the distal oxygen of H_2O_2 lengthens the O−O bond from 1.46 to 1.65−1.70 Å. This result clearly demonstrates the connection between hydrogen bonding to the distal oxygen of H_2O_2 and the strength of the O−O bond. The DFT_2/MM calculations indicate that the reaction would first occur through the formation of Cpd 0 in the doublet state, followed by O−O homolysis concerted with hydrogen transfer from H_2S to the developing water molecule (see the reaction scheme in **Figure 12**) because this pathway has a much lower PE barrier, 5.4 kcal mol^{-1}. In contrast, the quartet and sextet states have much higher calculated barriers of 20.1 and 21.1 kcal mol^{-1}, respectively. In the quartet state, there are two large decreases in the PE scan (**Figure 13**), one at an O−O bond distance of 2.05 Å, associated with proton transfer from H_2O_2 to His64, and another at an O−O bond distance of 2.15 Å, associated with proton transfer from H_2S to the distal oxygen of H_2O_2. In the sextet state, this latter proton transfer occurs at an O−O bond distance of 2.20 Å.

The homolytic cleavage product was further geometry- optimized with the DFT_2/MM method. The quartet state is clearly favored for the product of this reaction, being 10.2 kcal mol^{-1} lower in energy than that of the doublet state and 12.5 kcal mol^{-1} lower in energy than that of the sextet state. Thus, the DFT_2/MM calculations indicate a spin-crossing event from the doublet to quartet state,

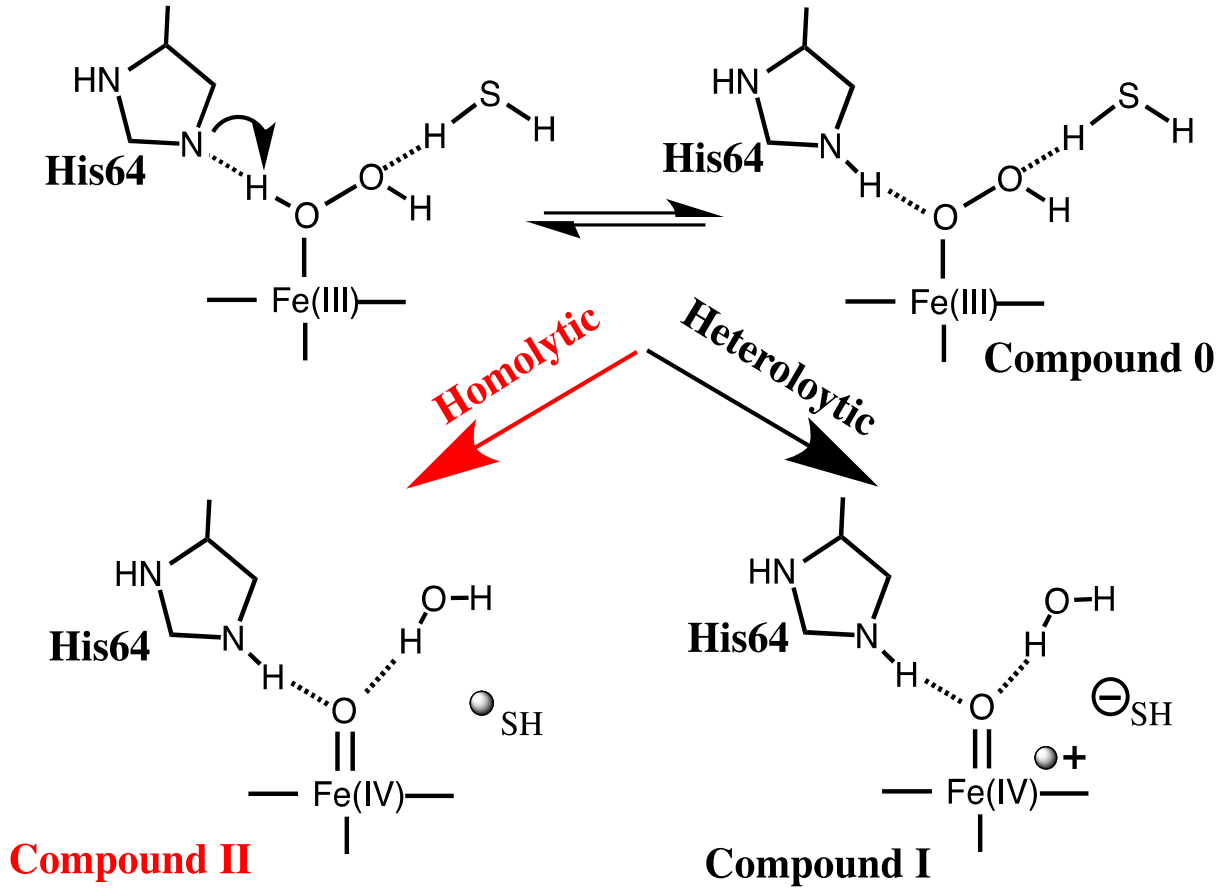

Figure 12: Reaction pathways leading to formation of a reactive sulfur moiety. Reactions could be initiated from either the Fe(III)-H_2O_2 bound state or Cpd 0 with homolytic or heterolytic bond cleavage leading to either Cpd II or Cpd I respectively. The formation of Cpd 0 could be concerted with these reactions[96]. From http://dx.doi.org/10.1021/acs.jpcb.6b02839

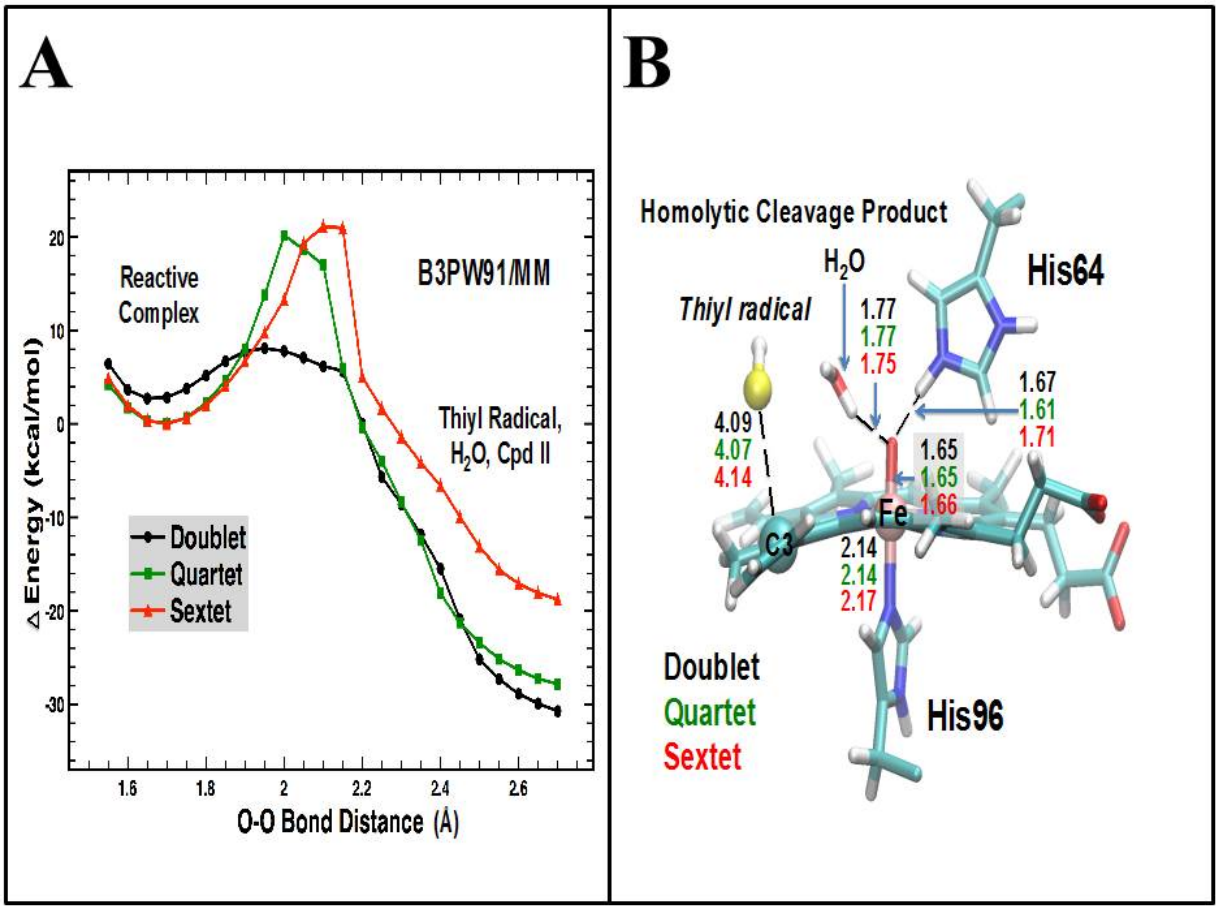

Figure 13: ***(A)*** *DFT_2/MM minimum energy path for breaking the H_2O_2 O-O bond using geometries optimized with the DFT_1/MM method. The reaction coordinate is the O-O bond distance.* ***(B)*** *DFT_2/MM geometry optimized structures of the homolytic cleavage product in all three spin states[96]. From* http://dx.doi.org/10.1021/acs.jpcb.6b02839

occurring past the transition state for O−O homolysis. The formation of a thiyl radical through O−O homolysis rather than heterolysis agrees with the findings on heme oxygenases that demonstrate that weak hydrogen bonding to the distal ligand will result in homolytic cleavage rather than heterolytic cleavage[105]. Finally, although the DFT_2/ MM PE scan along the O−O bond distance does not show a minimum along this reaction coordinate, the thiyl radical likely exists within a "minimum energy cage" made up of Phe28, Phe29, Leu32, Phe33, Phe43, Phe68, Ala109, and the heme. Thus, the thiyl radical is more likely to react instantly with proximal sites on the heme rather than escape the active site. Analogous calculations performed on $OH^{\cdot}$ formation within a heme oxygenase indicated that the radical was bound by 11 kcal mol^{-1} [106]. Representative products are shown in **Figure 13**. As previously mentioned, a primary objective of this study was to determine whether the breaking of the O−O bond in the presence of H_2S hydrogen bonding to the distal oxygen would be through heterolytic or homolytic cleavage of the O−O and S−H bonds (**Figure 12**). The DFT_2/MM PE scans in all three spin states result in the formation of H_2O, $HS^{\bullet}$ (thiyl radical), and a ferryl heme, as shown in **Table 1** and **Figure 14**. DFT_2/MM spin-density distribution of the homolytic cleavage product in the doublet and quartet states is shown on **Figure 14**. The doublet state is anti ferromagnetic, with three unpaired electrons (two α and one β). The spin of the electron centered on sulfur is flipped in the quartet state, whereas the higher- energy sextet shows two additional unpaired electrons centered **Figure 14**. Green surfaces show areas of α spin density, whereas yellow surfaces show areas of β spin density. **Table 1** provides the spin-density values from the Mulliken population analysis on the Fe atom and a small increase in the α spin density on the pyrrole nitrogens (**Figure 14** and **Table 1**). The catalytic cycle of peroxidases often produces a Cpd I species (the $Fe^{(IV)}$ porphyrin radical cation) in which an unpaired electron is delocalized over the pyrrole nitrogens. Significant spin density over the porphyrin ring is not observed from our calculations for this intermediate in all three spin states, suggesting that Cpd II ($Fe^{(IV)}=O^{-}$) is the product of this reaction as shown in **Figure 12**. The calculated Mössbauer parameters

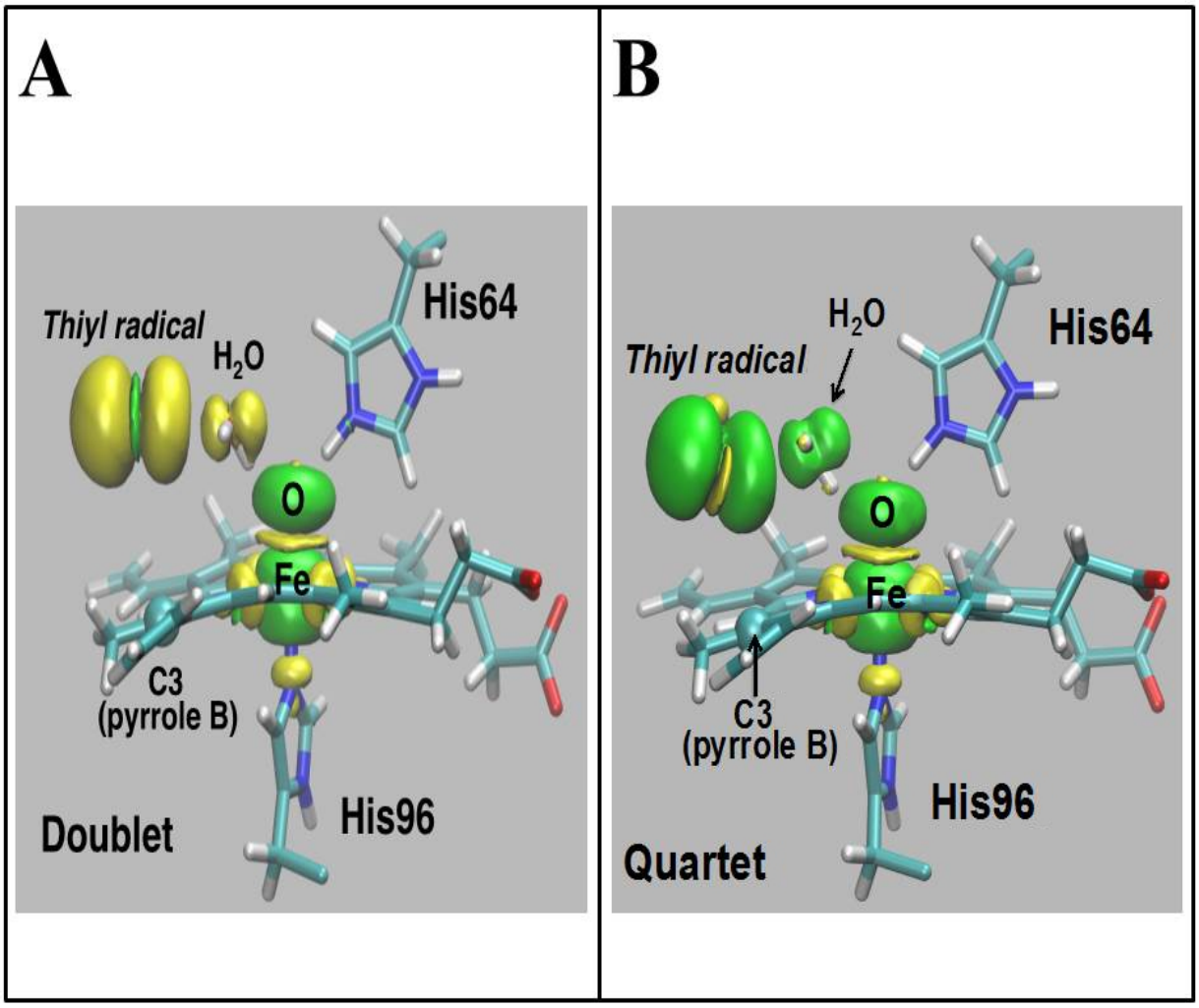

*Figure 14: DFT_2/MM spin-density distribution of the homolytic cleavage product in the **(A)** doublet and **(B)** quartet states. Green surfaces show areas of α spin density, whereas yellow surfaces show areas of β spin density. **Table 1** provides the spin-density values from the Mulliken population analysis[96]. From http://dx.doi.org/10.1021/acs.jpcb.6b02839*

Table 1: Spin density values from Mulliken population analysis for all relevant structures along the reaction path of sulfheme formation[95]. From http://dx.doi.org/10.1021/acs.jpcb.6b02839

	Fe	O1 (bonded to Fe)	O2	N (pyrroles)	S
HisE7HbI with H_2O_2 bound to Fe(III)					
Cpd 0-Doublet	1.05	0.06	0.00	-0.12	0.00
Hydroperoxy-Quartet	2.98	0.09	0.01	-0.26	0.00
Hydroperoxy-Sextet	4.37	0.14	0.02	0.23	0.00
Thiyl radical, H_2O and Cpd II					
Doublet	1.62	0.47	-0.10	-0.09	-0.90
Quartet	1.64	0.50	0.12	-0.14	0.92
Sextet	3.54	0.29	0.10	0.14	0.93
3-membered episulfide ring					
Doublet	1.10	0.02	0.00	-0.13	0.00
Quartet	3.05	0.06	0.00	-0.27	0.00
Sextet	4.43	0.07	0.00	0.25	0.00
Thiochlorin					
Doublet	1.09	0.02	0.00	-0.13	0.00
Quartet	3.07	0.05	0.00	-0.28	0.00
Sextet	4.43	0.06	0.00	0.24	0.00

for the ferryl complex in the doublet and quartet states are similar to other experimental Cpd II values[107] (**Figure 15** and **Table 2**).

1.3.4 Formation of the Three-Membered Episulfide Ring.

The selectivity of sulfur insertion into pyrrole B of the porphyrin system is not immediately apparent, although experimental studies of sulfHb and sulfMb have demonstrated that the process is specific for pyrrole B (presumably through addition to C3; **Figure 7**)[47]. The penetration of the sulfur source, H_2S, into this specific region of the heme (near pyrroles A and B as opposed to pyrroles C and D) provides a partial explanation for the selectivity toward the part of the heme most separated from bulk solvent. Yet, once the thiyl radical is formed, it appears entirely possible that it could react with other parts of the heme as well. Here, we will focus our discussion on the results that distinguish thiyl radical addition to C3 (pyrrole B) and to C2 (pyrrole A) because these two positions were energetically most favorable. Additional PE scans were performed for thiyl radical addition to other positions on the heme, but the PE barriers and thermodynamics of these additions were highly unfavorable and therefore have not reported.

DFT_1/MM PE scans along the $^{\bullet}S-C3$(pyrrole B) bond distance in all three spin states indicated no PE barrier for this addition step, whereas PE barriers of 12−15 kcal mol^{-1} were observed for PE scans along the $^{\bullet}S-C2$(pyrrole A) bond distance in all three spin states (Supporting Information). The thiyl radical is positioned between Phe68/C2 on one side and Phe43/C3 on the other (see **Figure 10** for locations of Phe43/68). Yet, Phe68 is in closer proximity to C2 than that of Phe43 to C3. This differential placement of the Phe residues is most likely the basis of the difference in PE barriers. Phe68 is displaced during thiyl radical addition to C2 (rmsd = 0.48 Å between the starting and ending structures), whereas a much smaller displacement of Phe43 occurs (rmsd = 0.23 Å) during thiyl radical addition to C3. These differential barriers provide another reason for the specificity of sulfheme

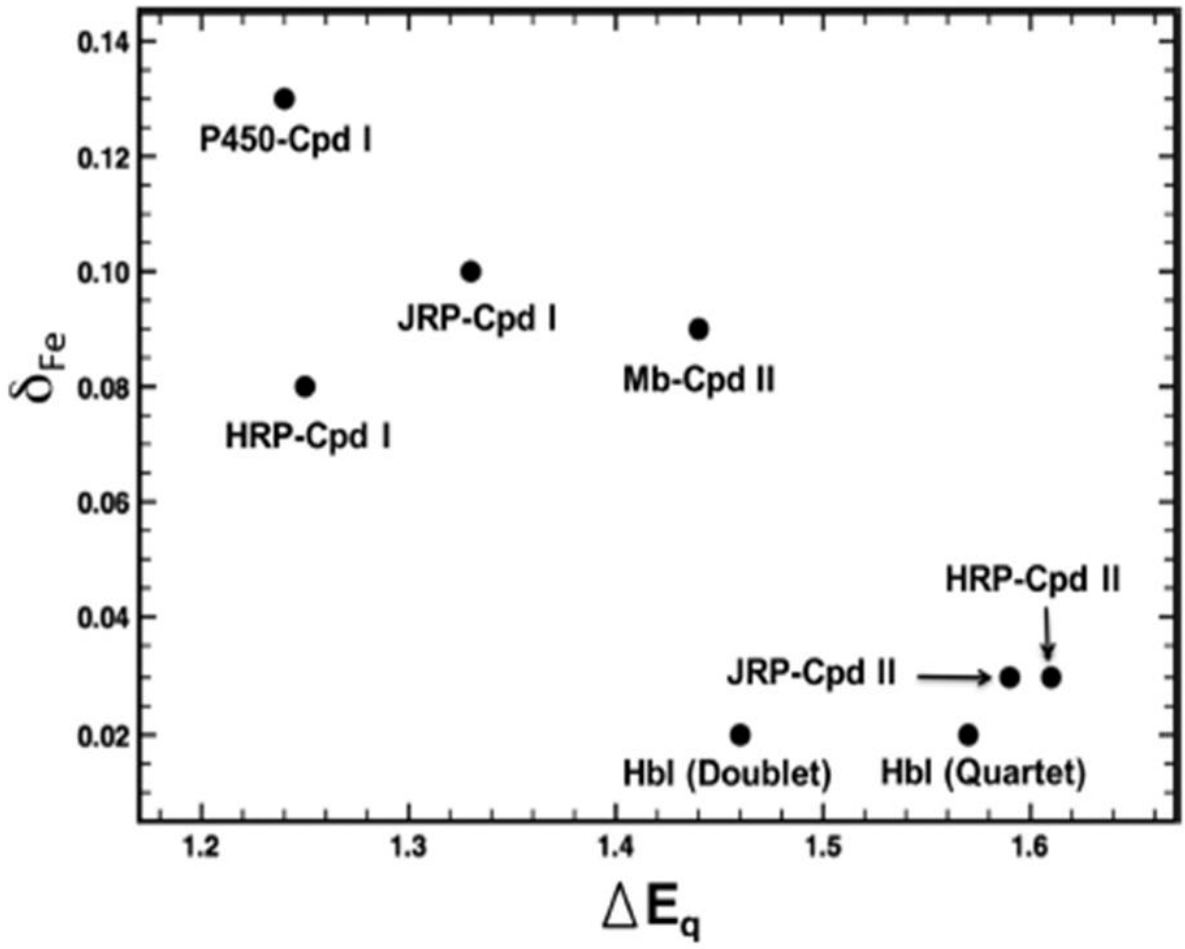

Figure 15: Experimental Mössbauer spectra values plotted vs the values obtained from B3PW91 calculations of HbI once the thiyl radical and a water molecule are formed through the breaking of the H_2O_2 O−O bond. The lowest energy quartet state is near other values for Cpd II and thus is assigned to be Cpd II[96]*. From* http://dx.doi.org/10.1021/acs.jpcb.6b02839

Table 1: Mössbauer parameters, δ_{Fe} and ΔE_Q, for all relevant structures along the reaction path of sulfheme formation. δ_{Fe} is calculated using the following formula: $\delta_{Fe} = \alpha(\rho_0 - C)\beta$, α, β and C were determined by linear regression fit to experimental data with values of -0.298, 1.118 and 11580 respectively[90]. ρ_0 is proportional to the electron density around Fe. From http://dx.doi.org/10.1021/acs.jpcb.6b02839

	δ_{Fe}	ΔE_Q
Thiyl radical, H_2O and Cpd II		
Doublet	0.02	1.46
Quartet	0.02	1.57
Sextet	0.02	1.57
3-membered episulfide ring		
Doublet	0.29	2.32
Quartet	0.38	1.70
Sextet	0.35	0.74
Thiochlorin		
Doublet	0.30	2.31
Quartet	0.39	1.91
Sextet	0.36	0.81

formation at pyrrole B. Significant spin density is transferred into the vinyl moieties of pyrrole A/B upon thiyl radical addition to C2/C3 and into the pyrrole moieties (**Figure 16**). Calculated Mössbauer parameters indicate that the projection of spin density onto the heme results in a species similar to Cpd I but with the spin density anisotropically distributed toward pyrrole B.

Yet, both of the ring-opened episulfide structures, on C3 and C2, are only metastable along this particular reaction coordinate (see the **Method**). This lack of stability is in agreement with NMR experiments that do not detect any intermediate of this type[48,108]. Extensive DFT_1/MM geometry optimizations and PE scans along different reaction coordinates and in all three spin states all lead to the formation of the three membered ring (S_AHisE7HbI) sulfheme. This result indicates that only the final product is stable (**Figure 17**). Interestingly, these calculations indicate that once the thiyl radical reacts with pyrrole B, the thiyl proton is transferred to the intervening water molecule and two protons are transferred to $Fe^{(IV)}$=O, one from His64 (as observed in the geometry optimization with no restraints) and another from the intervening water molecule. The final product is the $Fe^{(III)}$–H_2O resting state and S_AHisE7HbI. Thus, the calculations suggest a compelling mechanism, as shown in **Figure 18**. The overall reaction may appear concerted, although most likely asynchronous, given the results of our unrestrained geometry optimizations in which only one proton transfer occurred spontaneously (**Figure 17**). The mechanism determined through these calculations has similarities to another proposed mechanism for the covalent modification of myeloperoxidase by thioxanthine in which the ligand donates a proton to Cpd I/II as part of the covalent binding process to regenerate the Fe(III) resting state[109]. The Mulliken population analysis indicates that one unpaired electron is centered on the Fe atom in the doublet state, verifying the Fe(III) assignment (**Figure 19**). An electron must be transferred from the vinyl moiety of pyrrole B to Fe through a coupling of the π/d_π orbitals to reduce the Fe from the ferryl to the ferric state.

DFT_2/MM geometry-optimized structures of S_AHisE7HbI showed that the sulfheme formed on

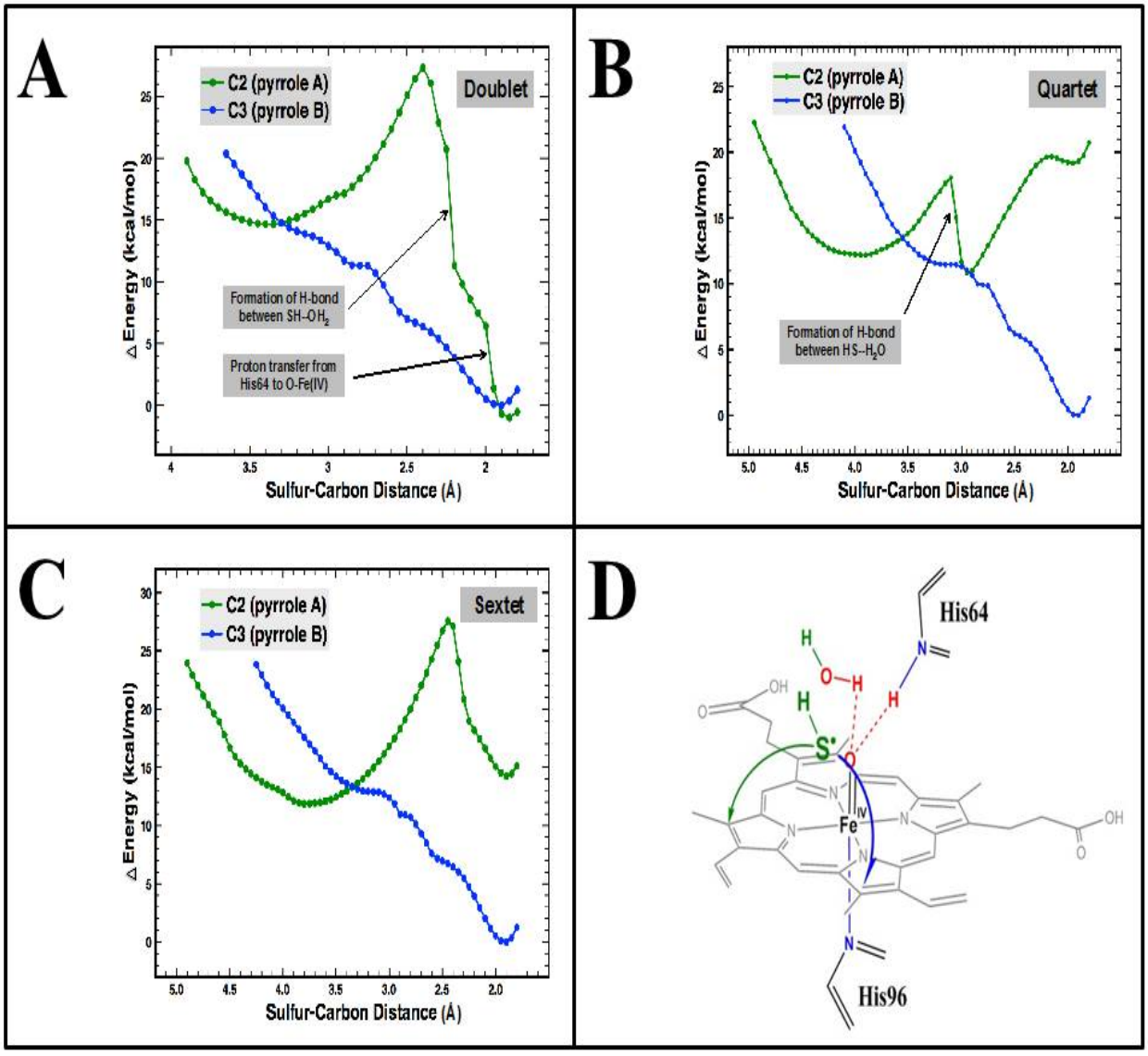

Figure 16: BP86/MM PE scans along the ˙S-C3/C2 bond distance to form metastable ring opened episulfide. We have different multiplicities PE scans where the ***(A)*** *belongs to the Doublet, the* ***(B)*** *for the Quartet, and the* ***(C)*** *for the Sextet. On* ***(D)*** *is shown the scans positions over the heme. The green for the C2(pyrrole A) and blue for the C3(pyrrole B)*[96]*. From* http://dx.doi.org/10.1021/acs.jpcb.6b02839

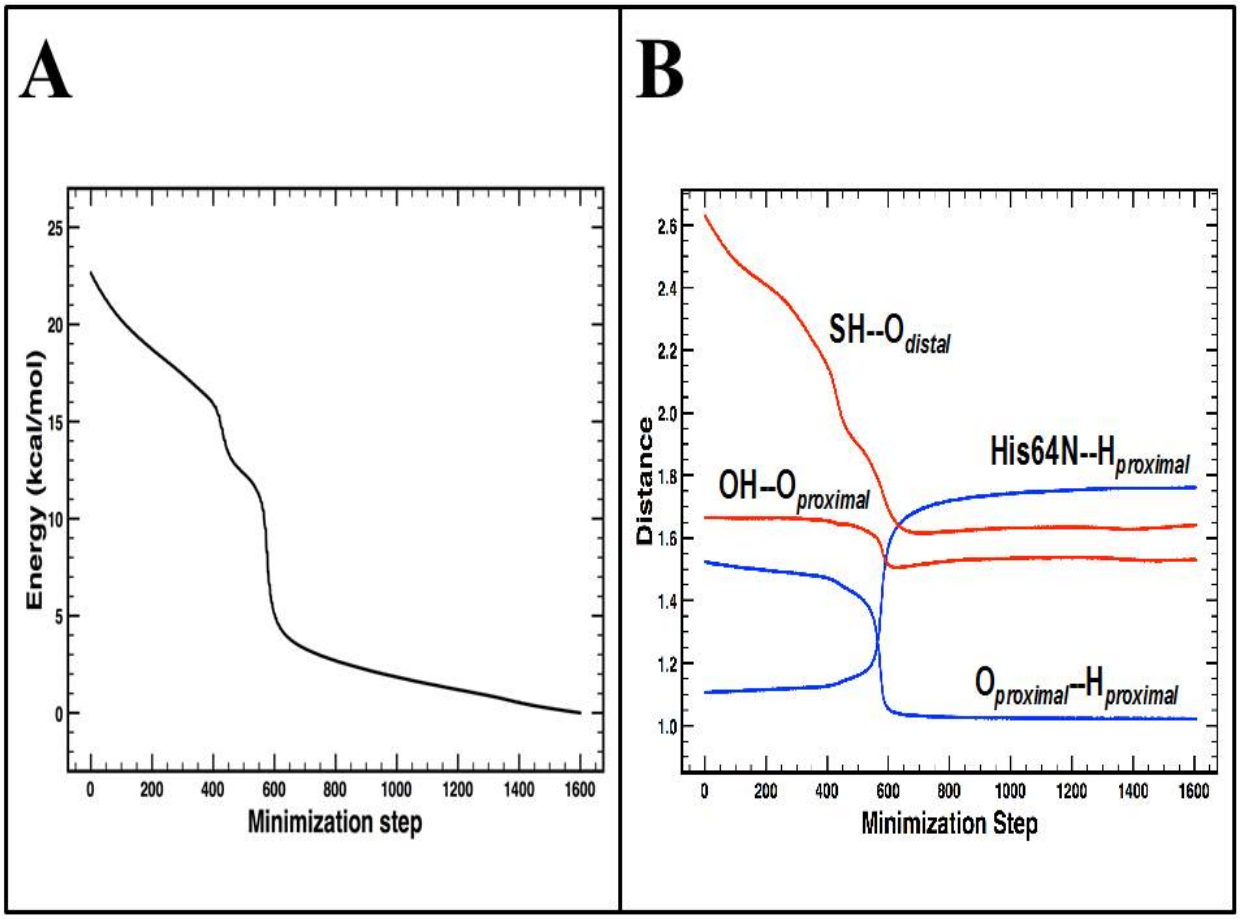

*Figure 17: (**A**) Change in potential energy upon a conformational change that leads to hydrogen bonding between –C3-S-H and the water molecule that is, in turn, hydrogen bonded to Fe(IV)=O and subsequently proton transfer from His64 to Cpd II. Upon completion of this scan, the model is aligned for two more proton transfers. One from –C3-S-H to the water molecule and one from the water molecule to Fe(IV)=O to form the 3-membered episulfide ring and the Fe(III) resting state. (**B**) Change in distances (Å) associated with the conformational change. BP86/MM PE scans along the reaction coordinates for proton transfer did not indicate any PE barrier[96]. From* http://dx.doi.org/10.1021/acs.jpcb.6b02839

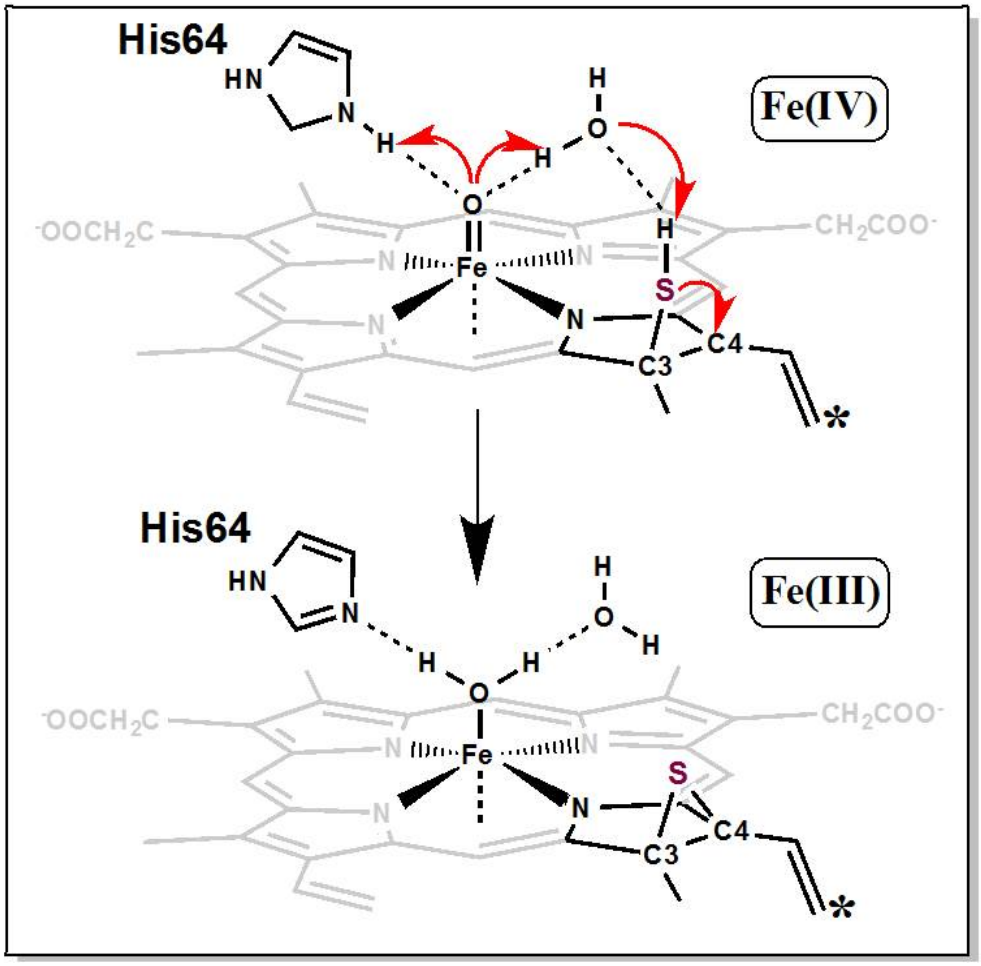

*Figure 18: The complex mechanism for the formation of SAHisE7HbI (three-membered ring) in pyrrole B once the thiyl radical (see **Figure 14**) has added to C3 involves **(A)** sulfur addition to C4, **(B)** proton transfer from R-S−H to the intervening water molecule, and **(C)** two proton transfers to the ferryl oxygen, one from the intervening water molecule and the other from His64[96]. From http://dx.doi.org/10.1021/acs.jpcb.6b02839*

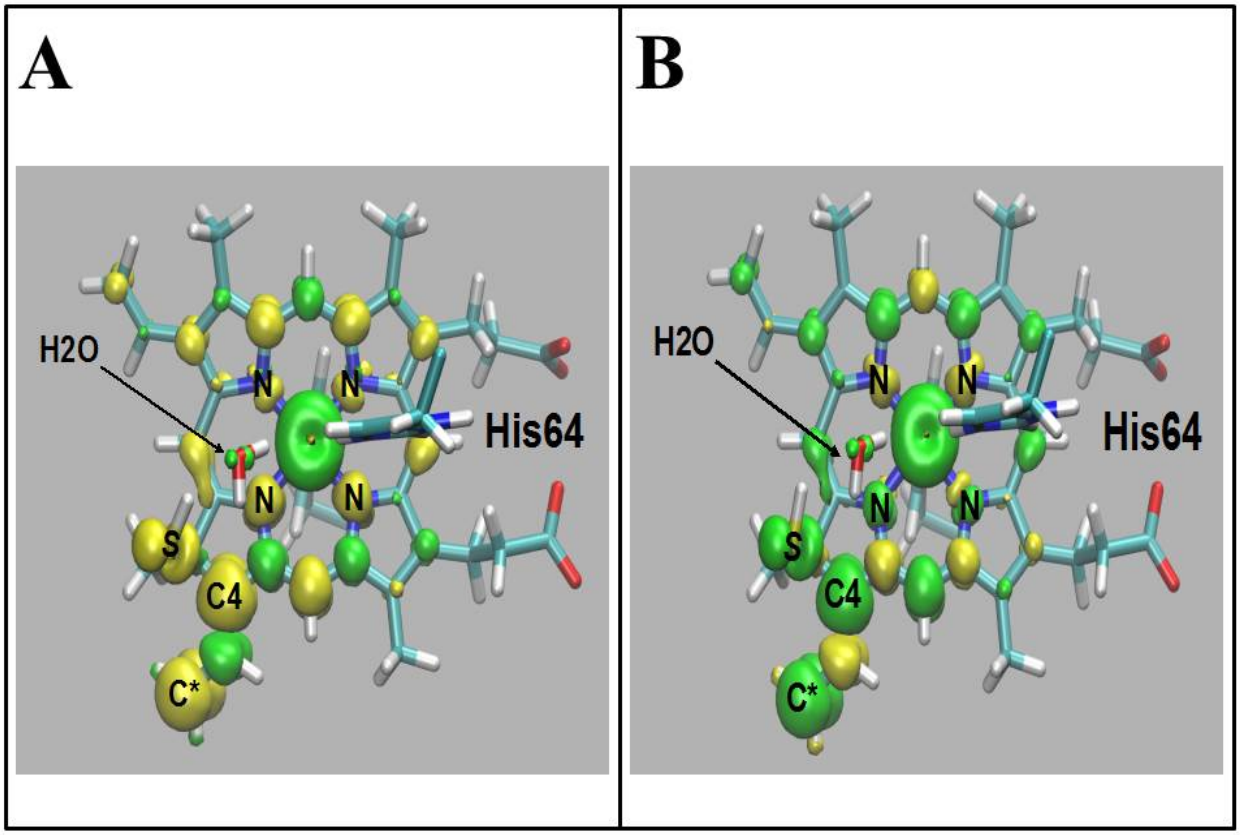

Figure 19: Spin density distribution of BP86/MM structure of the metastable ring-opened episulfide in doublet ***(A)*** *and quartet* ***(B)*** *states. View is looking down on heme from the distal side. Significant spin density is projected into the porphyrin ring and the vinyl group attached to pyrrole B*[96]*. From* http://dx.doi.org/10.1021/acs.jpcb.6b02839

pyrrole B is more stable than the one formed on pyrrole A in each respective spin state (**Figure 20**). The PE differences between the two structures in the doublet, quartet, and sextet states are 3.2, 3.1, and 3.7 kcal mol^{-1}, respectively. The sextet state was the lowest in PE for SAHisE7HbI on pyrrole B, being favored by PEs of 2.7 and 3.7 kcal mol^{-1} over those of the doublet and quartet states. Thus, the DFT_2/MM results suggest that a spin-crossing event from the quartet to the sextet state would occur at some point between the creation of the thiyl radical/Cpd II and the formation of S_AHisE7HbI. A decrease of 55.7 kcal/mol^{-1} in the DFT_2/MM PE is observed for progressing from the thiyl radical/Cpd II quartet complex to the sextet form of S_AHisE7HbI.

The S_AHisE7HbI structures on pyrrole B (**Figure 20**) reveal a lengthening of the pyrrole NB−$Fe^{(III)}$ bond relative to the length of the other pyrrole nitrogen−$Fe^{(III)}$ bonds and to that of these bonds seen in the $Fe^{(III)}$–H_2O_2 complex. Thus, formation of S_AHisE7HbI is likely to cause a reduction in O_2 affinity, as experimentally found for sulfheme derivatives in Mb. The calculated Mössbauer parameters, δFe and ΔEQ, for S_AHisE7HbI in the quartet state are most similar to those reported for ferric met-aquo (**Table 2**). The δFe values are larger than those calculated for ferryl Cpd II, suggesting weaker σ bonds around the iron due to a decrease in the total s-electron density. This weakening of the σ bonds leads to increased Fe−N(pyrrole) bond lengths.

1.3.5 Formation of the Thiochlorin Ring Structure.

A DFT_2/MM PE scan along a reaction coordinate connecting SAHisE7HbI (three-membered ring) to SCHisE7HbI (five membered ring) indicates that a significant PE barrier of about 28 kcal mol^{-1} must be traversed in all three spin states (**Figure 21**). Yet, it has been observed in many mechanistic studies that PE barriers are often much higher than free-energy barriers obtained through umbrella-sampling MD simulations[109]. In addition, entropic effects not accounted for in PE scans would be favorable for transforming S_AHisE7HbI to SCHisE7HbI, because SCHisE7HbI is much less

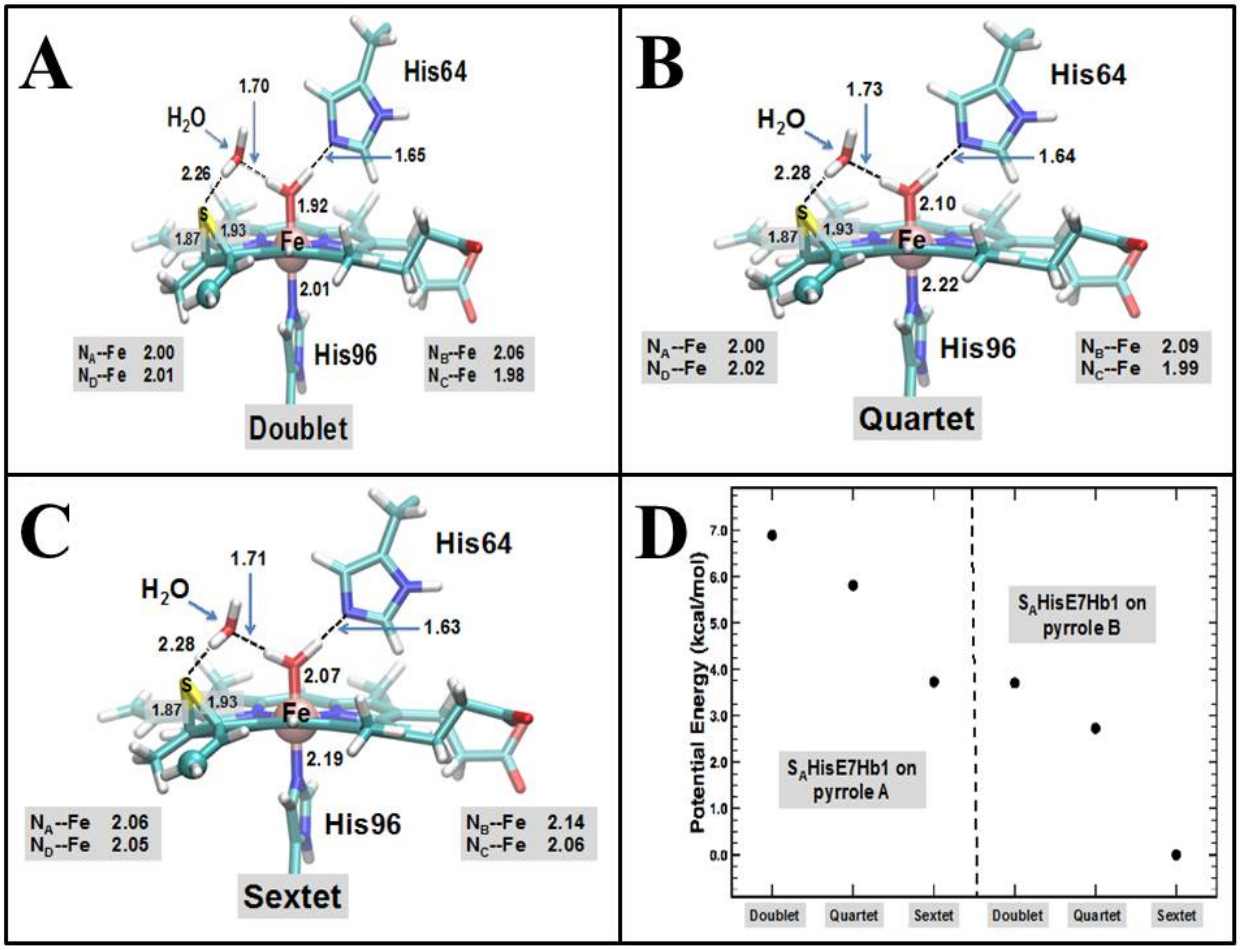

*Figure 20: DFT_2/MM geometry-optimized structures of the three-membered episulfide ring (S_AHisE7Hb1) in the doublet **(A)**, quartet **(B)**, and sextet **(C)** states, annotated with selected bond lengths (Å), including the distances of the pyrrole nitrogens from Fe(III). **(D)** DFT_2/MM energy- level diagram of S_AHisE7Hb1 in pyrrole B vs pyrrole A[96]. From http://dx.doi.org/10.1021/acs.jpcb.6b02839*

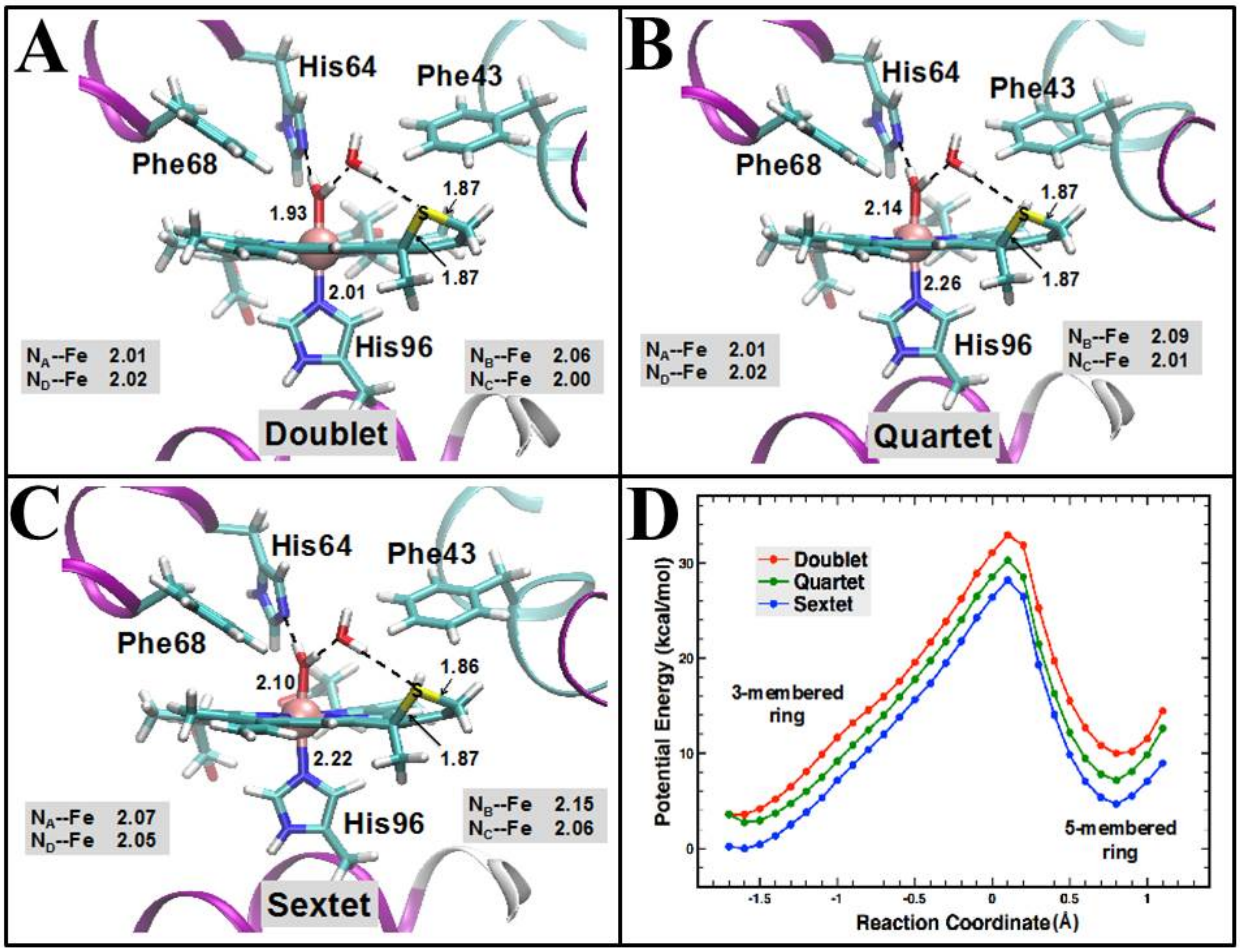

*Figure 21: DFT$_2$/MM geometry-optimized structures of the thiochlorin (S$_C$HisE7Hb1) in the doublet **(A)**, quartet **(B)**, and sextet **(C)** states, annotated with selected bond lengths (Å), including the distances of the pyrrole nitrogens from Fe(III). **(D)** DFT$_2$/MM PE profile along the reaction coordinate, described by the distance difference between S−C4 and S−C* (see **Figure 18** for atom names), using geometries optimized with the DFT$_1$/MM method. The energy of S$_A$HisE7Hb1 in the sextet state is set to zero[96]. From http://dx.doi.org/10.1021/acs.jpcb.6b02839*

strained than S_AHisE7HbI. Thus, with significantly more computationally intensive methods, we would expect to calculate a lower free-energy barrier. The DFT_2/MM PE differences between the three-membered episulfide and five-membered thiochlorin ring structures were 6.2, 3.1, and 2.9 kcal mol^{-1} in favor of S_AHisE7HbI for the doublet, quartet, and sextet states, respectively. Finally, the high-spin sextet state is favored by PEs of 2.9 and 7.0 kcal mol^{-1} over those of the quartet and doublet states, respectively, for S_CHisE7HbI. The favorably high-spin state is in agreement with NMR experiments[108].

Formation of S_CHisE7HbI results in a heme that is much more planar than S_AHisE7HbI. The formation of S_CHisE7HbI causes a distortion from planarity not only evident mostly in pyrrole B but also evident to some extent in pyrrole A. Val39 and Leu106 rotate slightly to accommodate the formation of S_CHisE7HbI. The $Fe^{(III)}$–OH_2 bond lengthens by only 0.02 Å. The pyrrole nitrogen–$Fe^{(III)}$ bond lengths are within 0.01Å of the values seen for the S_AHisE7HbI structure. Thus, both sulfheme species would be expected to decrease the affinity for O_2 by approximately the same magnitude. The crystal structure of cyanomet-S_CMb (PDB code 1YMC)[110] also shows that the pyrrole NB–$Fe^{(III)}$ and ND–$Fe^{(III)}$ bond lengths of 2.10 and 2.07 Å, respectively, are longer than the NA,C–$Fe^{(III)}$ bond length of 2.00/2.01 Å. The S–C3/C* bond distances are the same (1.87 Å) in all three spin states but asymmetric in the crystal structure (1.77/1.89 Å). Here, refinement of the mid- range resolution data is most likely the cause of the difference because DFT_2/MM calculated bond lengths are unlikely to have such a large error.

The calculated Mössbauer parameter, δFe, is practically identical for S_AHisE7HbI and S_CHisE7HbI in each respective spin state (**Table 2**). Some small differences in ΔE_Q are observed between the two isomers in the quartet and sextet states (0.21 and 0.05, respectively). The Mössbauer parameter, ΔE_Q, is sensitive to the surrounding environment and thus the small differences in ΔE_Q are likely due to the small differences in Fe–N and Fe–O bond lengths observed in the optimized structures (**Figure 20** and **21**).

1.4 Concluding Remarks

PM6/MM molecular dynamics simulations suggest that a small molecule like H_2O or H_2S could enter the most solvent excluded section of the HisE7Hb1 active site through the experimentally-determined Xe4 channel, forming a hydrogen bond with bound H_2O_2. The penetration of a water molecule in the simulations was mediated by the gating motion of Phe29 (B10). In addition, the DFT/ MM quartet and sextet states in the HisE7Hb1-H_2O_2 complex appear slightly more stable than the doublet state (Cpd 0) and thus would be less likely to react until a "co-substrate" like H_2O or H_2S were present in a catalytically relevant configuration. These calculated models observations argue for a mechanism of sulfheme formation involving the concerted interaction between His64, Fe(III)-H_2O_2 and H_2S through the formation of a thiyl radical.

DFT/MM calculations also revealed the basis for specificity of sulfheme formation on pyrrole B. Phe68 acts as a steric barrier for thiyl radical addition to C2 (pyrrole A) though other physicochemical properties may also contribute. C3 (pyrrole B) is bonded to two sp^2 carbons and a sp^3 carbon making it slightly more electrophilic than C2 (pyrrole A) that is bonded to three sp^2 carbons. These factors could be tested by mutating Phe68 to a smaller hydrophobic residue and or chemical modification of pyrroles A and B. Steric arguments have been used extensively to explain the results of heme modifications[111].

Finally, the calculations on S_AHisE7HbI and S_CHisE7HbI reveal a lengthening of the N_B-Fe bond, breaking the symmetry of the pyrrole rings around $Fe^{(III)}$. Furthermore, the heme π orbital coupling to the iron d_π orbitals may facilitate electronic withdrawal from the iron caused by the sulfur insertion. These structural and electronic changes will lead to a reduced oxygen affinity. A more in-depth molecular orbital analysis on these features is required along with the substitution of aqua met-HisE7HbI by HisE7HbI-O_2 models for a fuller understanding of the reduced oxygen affinity. In

summary, our DFT/MM calculations have led to a mechanism of sulfheme formation involving the concerted action of His64 in the E7 position and H_2S as well as the basis for specificity towards pyrrole B. Additionally, these simulations provide a mechanistic route where the generated radical avoids migration to the protein matrix in contrast to other peroxidative reactions. Finally, the calculations are in agreement with many experimental observations and suggest further experiments to verify the mechanism in this and other heme proteins.

2 Sulfheme Charge Transfer and π to π* Transitions in the Visible Spectra

2.1 Introduction

2.1.1 Sulfheme spectroscopy characteristics

The idea to understand the H_2S reaction phenomena in proteins started to be explored in the 19th century with the discovered "hemoglobin", in particular, Hoppe-Seyler, by presenting the first hemoglobin absorption spectrum in 1862[112]. In the year 1863 with the aid of the spectroscope, oxyhemoglobin was first studied while in the presence of H_2S and called this new green hemoglobin derivative "sulfhemoglobin"[113]. Thus, he was able to describe that sulfheme had a characteristic 618 nm absorption band which was located in the red region of the spectrum, slightly displaced toward the blue from the 635 nm methemoglobin band[112]. The work was extensively followed by Keilin[114] and Michel[115]. In 1933, Keilin showed that oxygen was essential for the formation of these sulfheme derivatives[114]. While, Michel demonstrated the formation of an analogous compound upon interaction of oxymyoglobin (oxyMb) with H_2S and termed the complex sulfmyoglobin (sulfMb)[115]. Both, hemoglobin (Hb) and myoglobin (Mb) in the presence of O_2 or H_2O_2 and H_2S generate sulfHb and sulfMb, respectively. Anaerobically H_2S binds to the heme reaction center and it can reduce the heme as function of the H_2S concentration and heme electronic environment[112–115].

Considerable research efforts have been directed toward the structural and mechanistic formation of sulfHb, sulfMb and other sulfheme proteins, which supported the modification of the heme chromophore by H_2S. The experiments reaffirm the characteristic transitions around 620 nm and 717 nm regions for the ferrous (deoxy) and ferric (met) sulfheme, being the electronic displacement function on heme oxidation and ligation states[41,115–117]. Vibrational analysis of the carbomonoxysulfmyoglobin (CO-SMb) complex showed, relative to carbomonoxymyoglobin (CO-

Mb), an increase in the CO stretching frequency suggesting a charge transfer process associated to a decrease in electron density from d iron orbitals to the antibonding π* orbital of carbon monoxide[39]. Radioactive sulfide species demonstrated that a single sulfur atom is integrated per mole of Mb to form sulfMb. The sulfur insertion resulted in a covalent heme modification of the pyrrole ring bearing the 4-vinyl group across the β-β double bond, removing electron density from the ferrous iron towards the periphery of the new chlorin ring[118].

Subsequent studies demonstrated that oxygen binding to sulfMb and to sulfHb decreased by ~2,500 and ~135 times, respectively in relation to the normal heme proteins[39,42,117,118]. The presence of an analogous sulfur chlorin ring in sulfheme has been supported by the X ray three-dimensional structure of cyanomet-sulfmyoglobin[110], resonance Raman[40,119], NMR[44,45,48,51,120], hemoglobin I(HbI), and HbI mutants from *Lucina pectinata*[121,122], Catalase[41,123], and lactoperoxidase (LPO)[124]. The relative fast reaction of sulfMb formation ($2.5\pm0.1 \times 10^6$ $M^{-1}s^{-1}$)[125] relative to the reaction between H_2S with Mb ($1.6\pm0.3 \times 10^4$ $M^{-1}s^{-1}$) and Hb (3.2×10^3 $M^{-1}s^{-1}$)[99,125] indicates the important role of peroxide species for the formation of the sulfheme species. At the same time, there is an inverse relationship between this increase rate and the decrease in pH supporting the crucial role of distal E7 His in the site plays in the mechanism of sulfheme formation[120,123]. However, there are heme proteins that do not form the sulfheme complex, for example, HbI from *L. pectinata,* which has Gln64 in the E7 position. Nonetheless, when glutamine (Gln) in the 64 position was site directed mutated to His64, an optical band at 624 nm attributed to sulfheme was observed. The results supported the unique function of E7 His in sulfheme formation[120,123]. These observations and the tautomeric nature of distal His[126,127] are in agreement with the importance of His protonation toward formation of Compound 0 and the ferryl heme O−O bond cleavage under two different scenarios dominated by O_2 and H_2O_2, respectively[128].

NMR of several sulfMbCN complexes revealed the presence of three isomeric forms of sulfMb

named S_AMb, S_BMb, and S_CMb (**Figure 22**)[48,51,120]. The S_A structure is an episulfide formed across the C3-C4 double bond, S_B is characterized as a "ring opened episulfide", and S_C is a thiochlorin structure[48,51,120]. Each sulfheme isomer has different physicochemical properties and hence, different reactivity and stability patterns. The NMR spectra of all isomers showed symmetry reduction of the prosthetic group and alteration of the π conjugation of pyrrole B that can be correlated with the electronic spectra[44,51]. Isolated deoxy sulfheme isomers S_AMb, S_BMb and S_CMb showed electronic transitions at 618 nm, 618 nm and 636 nm, while the met sulfheme isomers presented electronic bands at 718 nm, 720 nm and 736 nm, respectively[51]. Moreover, at pH=8 the deoxy sulfheme visible spectrum of the 600 nm region containing a 75% of S_CMb is red shifted in relation to the sulfheme species containing 87% of S_AMb. In the met sulfheme derivatives this changes are smaller and observed in the 700 nm region where the species containing 80% S_CMb is also red shifted relative to the sulfheme species containing 85% S_AMb[44,51]. Therefore, the sulfheme UV-Vis electronic transitions are a function of the heme oxidation, spin, and coordination state, moreover, the nature of the sulfur isomer structure stabilized in the process. Furthermore, the sulfheme mechanism[35] presented on **Figure 23**, indicates a hydrogen transfer from H_2S to Fe(III)-H_2O_2 complex resulted in the homolytic cleavage of the O-O and S-H bond to form a reactive thiyl radical ($HS^{\bullet}$)[96,129], ferryl heme compound II, and a water molecule. Subsequent addition of $HS^{\bullet}$ to pyrrole B in compound II specie leads to a metastable ring-opened episulfide (S_B) and a decrease of 64.9 kcal/mol^{-1} in the PES. This species become a met-aquo Fe(III) 3-membered thiochlorin ring (S_A) upon further decreasing of 73.3 kcal/mol^{-1} in the PES. Finally, the 5-membered thiochlorin structure is formed (S_C) upon a total favorable energy drop in the PES of approximately 140 kcal/mol^{-1} [96]. Under these circumstances, the formation and stability of sulfheme isomers S_A and S_C are both kinetically as well as energetically preferred. Overall, these theoretical results are in agreement with a wide range of experimental NMR data[44,48,51,120]. The sulfheme group has a modified π electron distribution where the number of double bond is reduced in

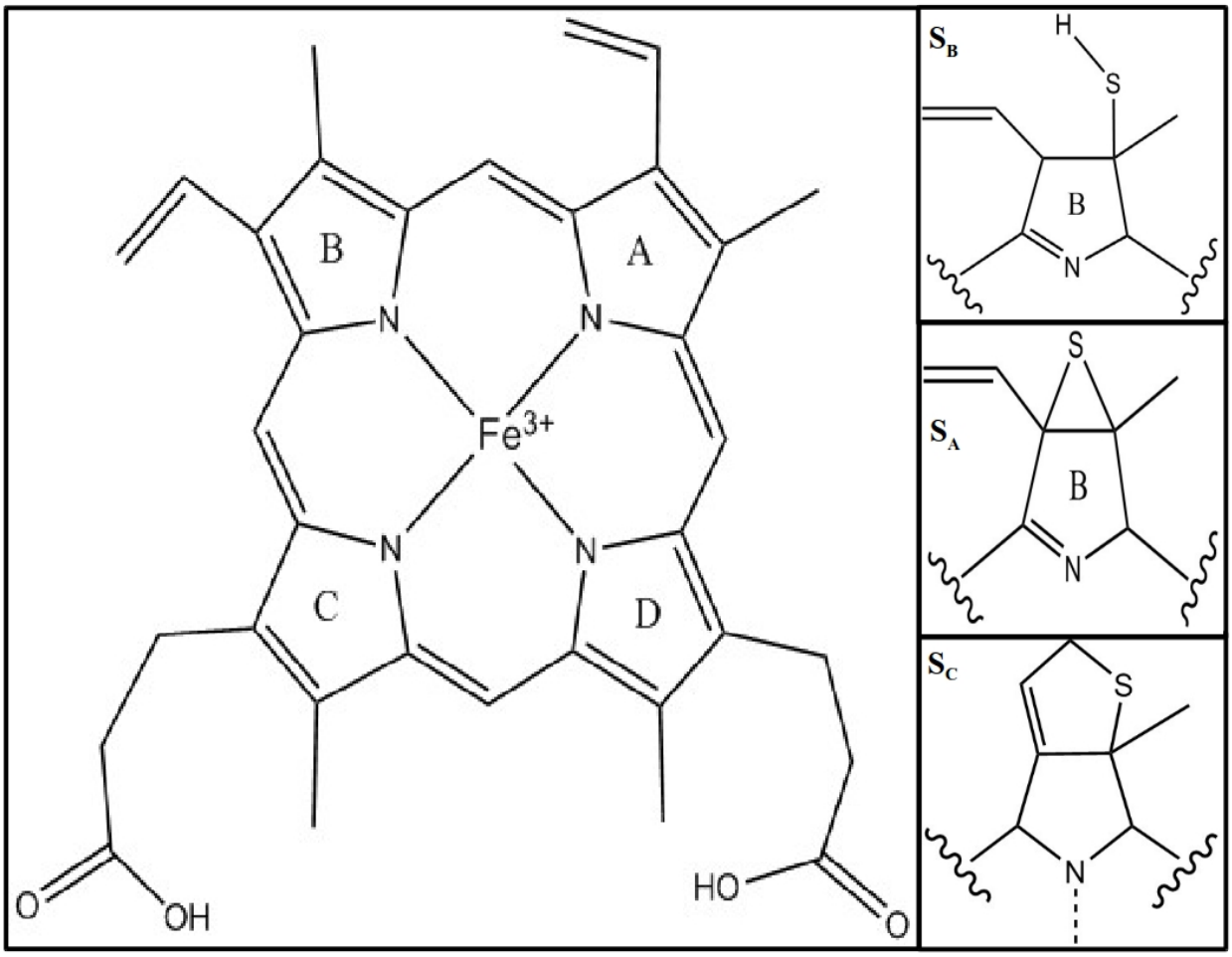

Figure 22: Porphyrin group and the three sulfheme pyrrole B isomers from top to bottom are sulfheme, S_B, S_A, and S_C . From https://pubs.acs.org/doi/abs/10.1021/acs.jpcb.7b12393

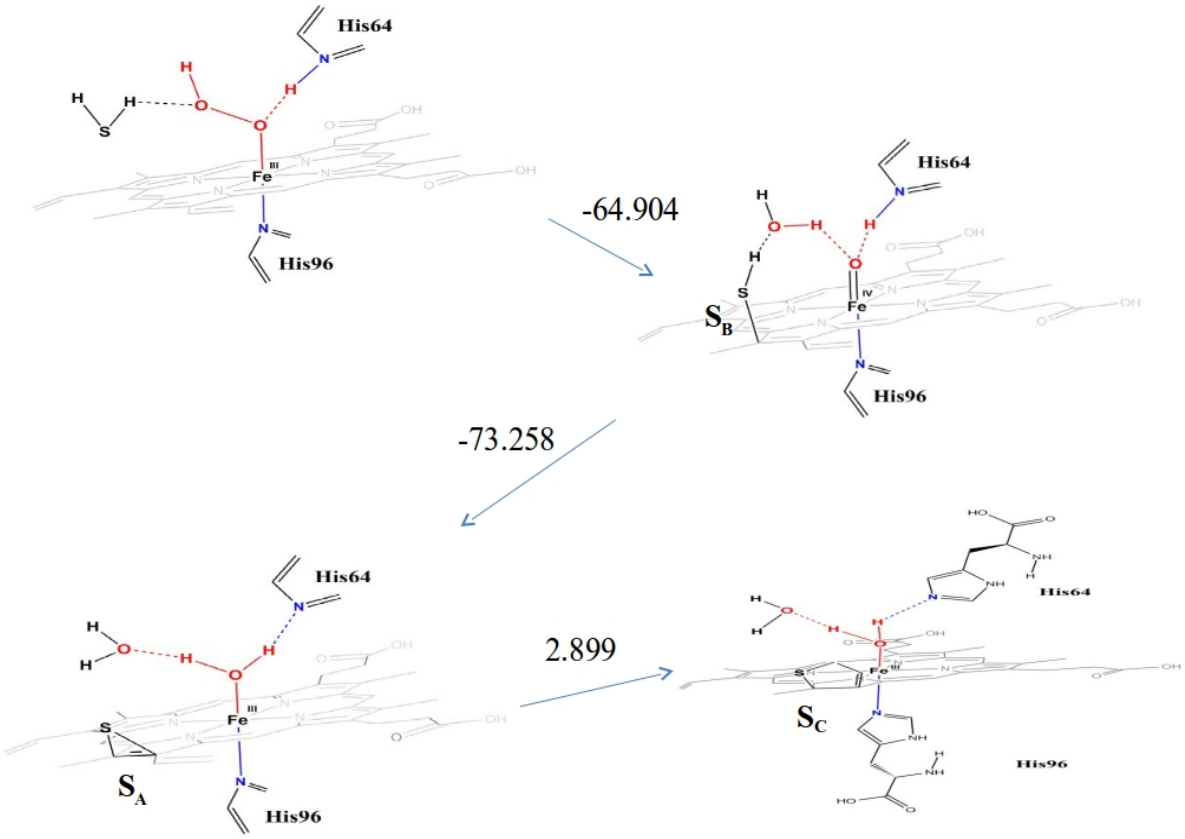

Figure 23: Sulfheme formation reaction: Heme in the presence of H_2O_2 and H_2S. kcal/mol^{-1} units. From https://pubs.acs.org/doi/abs/10.1021/acs.jpcb.7b12393

relation to a normal heme group. At the same time, a reduction in symmetry from a D_{4h} to a C_{2v} environment is acquired.

2.1.2 Heme molecular orbitals (MO) transitions

According to Gouterman[130–132] model, the electronic transitions of a D_{4h} symmetry aproximation porphyrin arises from the a_{1u} and a_{2u} orbitals to a degenerate e_g orbitals. The heme a_{1u} and a_{2u} orbitals are the HOMO orbitals, and the e_g orbitals represent the LUMO orbitals. The electronic transitions from HOMO to LUMO gave rise to one permitted transition of higher intensity called the Soret band, and a lower transition visible bands called the Q-bands. **Figure 24** presents the porphyrins HOMO (bottom orbitals) and LUMO (top orbitals). The experimental spectrum for porphyrins are characterized by π to π^* transitions with the presence of a strong Soret band and two weak visible bands[133]. In heme the a_{1u} orbital is unable to mix directly with the iron orbitals and is less affected by axial ligands but the a_{2u} orbital with its density dwelling around the pyrroles nitrogens (**see Figure 24**) is affected by them. Ligands above and below the central metal may have subtle influences, but may not affect the main features of the π to π^* porphyrin transitions in the visible and near UV experimental spectrum of porphyrins[130]. Therefore, upon sulfheme formation, there is a change to a C_{2v} symmetry similar to a chlorin, where the a_{1u} and a_{2u} orbitals become a_2 and a_1 while the degenerate e_g orbitals split into a set of b_1 plus b_2 orbitals. From this orbital rearrangements caused by the change in system symmetry we suggest could be a change of the main characteristic of the porphyrins transitions exhibited by sulfheme. It is suggested that charge transfer behavior in the porphyrin transitions could results from a shift of electronic density from one part of the heme to heme iron[42,123,133]. Thus, still is unclear the relationship between the electron withdrawing character of the sulfur in the three isomers, the nature of the transitions between the iron d orbitals, and the integrated heme porphyrin systems responsible from the electronic bands in the 600 nm and 700 nm region. It is suggested that the extra

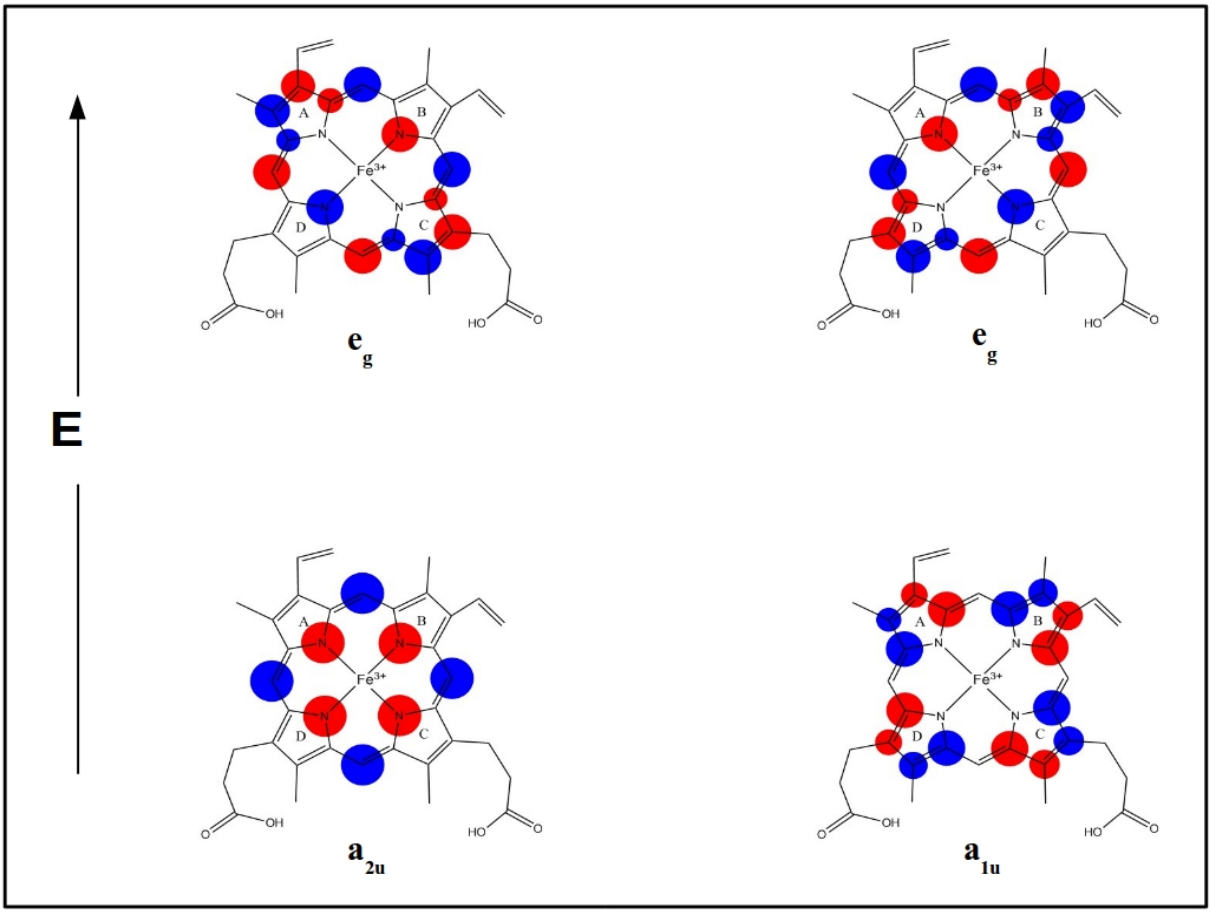

*Figure 24: Porphyrin frontier orbitals. HOMOs orbitals **(bottom)** and LUMOs orbitals **(top)**.*

visible bands are due to the (x,y) polarized charge transfer transitions. Zerner predicted that these charge transfer transitions should heavily mix with the π to π^* porphyrin transitions[133]. Possibly, the role of the heme iron oxidation state, and the effects of the D_{4h} to C_{2v} symmetry reduction in the electron density distribution of the HOMO and LUMO sulfheme orbitals are responsible for the experimental UV-Vis spectra.

2.1.3 Time-Dependent Density Functional Theory (TDDFT)

As presented before DFT had proven it is possible to describe all the ground state properties of a many body system from functionals dependent of the electron density. Otherwise, DFT can not predict excited state properties. It is needed to determined excited states properties if we want to be capable to predict spectra. To be able to explain correlated electron motion observed in physical phenomena, and help provide theoretical description of observed transitions it was need a *ab initio* theoretical ground work which will help to solve the non-relativistic time-dependent Schrödinger equation. Equation 2.1 shows the time-dependent Schrödinger equation

$$\hat{\mathrm{H}}(t)\Psi(t)=i\frac{\delta\Psi(t)}{\delta t} \tag{2.1}$$

and the Hamiltonian $\hat{\mathrm{H}}(t)$ generally is represented as shown next

$$\hat{\mathrm{H}}(t)=\hat{T}+\hat{V}_{ee}+\hat{V}_{ext}(t) \tag{2.2}$$

In the Hamiltonian the first term represents the kinetic energy and the second term the electron-electron repulsion. Next equation shows the kinetic energy and electron-electron repulsion, respectively.

$$\hat{T}=-\frac{1}{2}\sum_{i=1}^{N}\nabla_i^2 \quad , \quad \text{and} \quad \hat{V}_{ee}=\frac{1}{2}\sum_{i\neq j}^{N}\frac{1}{|r_i-r_j|} \tag{2.3}$$

The last term in the hamiltonian is $\hat{V}_{ext}(t)$ represents the potential experimented by the system which includes any external field applied and the Coulombic potential between the electrons and the nuclei. If the external field for a system is a laser beam ilumination the dipole aproximation for $\hat{V}_{ext}(t)$ will be as follows

$$\hat{V}_{ext}(t)=\sum_{i=1}^{N}\nu_{ext}(r_i,t) \qquad \text{where} \qquad \nu_{ext}(r_i,t)=Ef(t)\sin(\omega t)\boldsymbol{r}\cdot\boldsymbol{\alpha}-\sum_{\nu=1}^{N_n}\frac{Z_\nu}{|\boldsymbol{r}-\boldsymbol{R}_\nu|} \tag{2.4}$$

The time-dependent Schrödinger equation proves to be a daunting task to solve. Furthermore, solving it through the use of wave function methods consumes a lot of computational resources making it exponentially expensive with the system size . In 1984 20 years after Kohn and Sham (**KS**) DFT theorem[57] , Runge and Gross[134] expanded DFT many body description to time-dependent systems. Time-dependent density functional theory (TDDFT) showed that all observable properties of a many-electron system, beginning in a given initial state Ψ(0), may be extracted from the one-body time-dependent density alone[135].

TDDFT has shown to reduce the system size exponential scaling to a more computationally affordable N^3 scaling[136]. TDDFT theorem proves there is a one to one correlation between the electronic one body density and the external potential of a system evolving from a fixed intial sate Ψ(0). Assuming as in DFT ground state that the KS system exist we calculate the density of a interacting system using the next equation

$$n(\boldsymbol{r},t)=\sum_{j=1}^{N}|\Phi_j(\boldsymbol{r},r)|^2 \tag{2.5}$$

The KS system conforms to the time-dependent Schrödinger equation as follows

$$i\frac{\delta}{\delta t}\Phi(\boldsymbol{r},t)=\hat{H}_{KS}(\boldsymbol{r},t)\Phi(\boldsymbol{r},t) \tag{2.6}$$

The KS hamiltonian is defined by the next equation

$$\hat{H}_{KS} = -\frac{\nabla^2}{2} + \nu_{KS}[n](\boldsymbol{r}, t) \tag{2.7}$$

Similar as in DFT in this new TDDFT formalism de ν_{KS} can be represented as sum of threee terms[136] as seen next

$$\nu_{KS}[n](\boldsymbol{r}, t) = \hat{V}_{ext}(\boldsymbol{r}, t) + \int d^3 r' \frac{n(\boldsymbol{r}', t)}{|\boldsymbol{r} - \boldsymbol{r}'|} + \nu_{xc}[\boldsymbol{n}; \Psi_0, \Phi_0](\boldsymbol{r}, t) \tag{2.8}$$

In the first term we have the external potential described in equation 2.4. The second term belongs to the time-dependent Hartree potential which describes the electron-electron interactions, and the last term in equation 2.8 is the exchange-correlation potential that as in ground state DFT accounts for all the nontrivial many-electron effects. As in DFT the xc is approximated using physical and mathematical arguments[136]. TDDFT uses an adaptation of the LDA and GGA aproximations. The simplest approximation used in TDDFT is the adiabatic aproximation . The "adiabatic" implies that the density at time *t* is tied to a ground state functional[135]. This approximation is shown in the next equation

$$\nu_{XC}^{adiabatic}[n_\uparrow, n_\downarrow](\boldsymbol{r}, t) = \tilde{\nu}_{XC}[n_\uparrow, n_\downarrow] d^3 r n(\boldsymbol{r}) \tag{2.9}$$

In the previous equation the $\tilde{\nu}_{Xc}[n_\uparrow, n_\downarrow]$ is the ground state xc functional. The most widely used TDDFT xc funtional is adiabatic local density approximation (**ALDA**). We can encounter the same problems with ALDA as with LDA. We can change LDA for a GGA or MGGA, but at regions where the electrons are pushed to far from the nuclei, the TDDFT xc functional suffers the same incorrect asymptotic behavior as the DFT functionals.

2.2 Methods

2.2.1 Model construction

As previously reported, we performed a PM6/CHARMM molecular dynamics (MD) simulation for a model of the HbI GlnE7His mutant[96]. This HbI mutant has an active site and experimentally determined properties very similar to myoglobin (Mb). A snapshot from the 1.4 nanosecond (ns) PM6/ MM MD simulation was used as a starting model for investigation into the mechanism of sulfheme formation using a hybrid B3PW91/MM potential energy function. The final sulfheme isomer models were obtained from extensive geometry optimization steps and then used to calculate the electronic transitions for interpreting UV-Vis spectra. The S_A and S_C sulfheme models contained 11,320 atoms. The QM region for the met-aquo sulfheme structures was composed of the entire heme group, the proximal His93, the distal His64, Phe29, Phe43, Phe68, two water molecules and the sulfur atom inserted into the heme group for a total of 144 QM atoms. The QM region was chosen as such to remain consistent with our past studies. Calculations were performed in the lowest energy sextet state in agreement with experimental observations[96].

2.2.2 TDDFT calculations

TDDFT calculations were performed using the geometry optimized sulfheme structures. The size of the QM region for the TDDFT calculations was reduced after performing ZINDO/S[137,138] which revealed that the three phenylalanine (Phe) residues did not have an impact on the calculated results and thus these residues were represented with the MM force field (**see Tables 3 and 4**). The TDDFT calculations were performed using the hybrid B3PW91 functional[89,90,111] and the Ahlrichs def2-TZVP(-f) basis set[85,86] which has shown to provide accurate results when compared to experimental spectra[139–141]. The RIJCOSX approximation with the def2-TZVP/J Coulomb fitting basis set were used[85,86,111] for all models and functionals. M06L, M062X, TPSS0, and B3PW91 (with 50% Hartree

Table 3: QM region size effect on excited states calculations for S_A sulfheme. From https://pubs.acs.org/doi/abs/10.1021/acs.jpcb.7b12393

S_A sulfheme calculated visible bands	
ZINDO/S (QM 144 atoms)	**ZINDO/S (QM 102 atoms)**
754.4	754.2
623.4	621.4
543.9	539.1
516.6	515.7

Table 4: QM region size effect on excited states calculations for S_C sulfheme. From https://pubs.acs.org/doi/abs/10.1021/acs.jpcb.7b12393

S_C sulfheme calculated visible bands	
ZINDO/S (QM 144 atoms)	**ZINDO/S (QM 102 atoms)**
805.8	796.5
638.7	642.8
587.2	583.6
554.5	553.1
550.1	552.6

Fock exchange) functionals were also examined. B3PW91 was shown to be in better agreement with the experimental spectral region of interest (**Figure 25 and 26**). A total of 90 roots were calculated to cover the entire spectral window of interest. Molecular orbitals (MO) with the highest contribution for the electronic transitions were plotted using the Orca's orca_plot program[78,142,143]. The molecular orbitals were plotted using VMD version 1.9[76]. The sign of the plotted molecular orbitals is represented in two colors; red for positive, blue for negative.

2.2.3 Sulfheme Complex Formation and Ultraviolet-Visible Spectroscopy

UV-Vis spectroscopy provides information about the concentration, complex formation, and purity of the protein sample based on the heme group. The Mb protein sample was titrated with potassium ferrocyanide to form the met-aquo Mb complex which was monitored through the formation of its characteristic absorption bands at 407, 505, and 633 nm using an Agilent 8453 UV-Vis spectrophotometer. The experimental Mb protein concentration was 2 mM. Then the protein Mb sample, buffer, hydrogen peroxide solution, Na_2S salt, and $Na_2S_2O_4$ salt were each transferred to small vials (ranging from 300 μL to 1.5 mL) and tightly sealed with a rubber septum. The samples were degassed and then, purged for 15 minutes with 99.0% nitrogen gas (N_2; from Linde) to remove the oxygen present in the sample. H_2O_2 was added to the met-aquo Mb protein to form the ferryl species with subsequent addition of H_2S to form the sulfheme isomers, all performed in anaerobic conditions. The [protein:H_2O_2:H_2S] concentration ratio was [1:3:5].

The sulfMb formation was monitored by evaluating the characteristic absorption bands at 620 and 720 nm at 1, 5 and 30 min[144]. The stopped-flow experiments were carried out with the same sample [1:3:5] concentration ratio using a Olis RSM 1000 UV/Vis[NIR] rapid scanning spectrometer. The stopped-flow spectra were performed from 10 - 500 ms time window with 10 ms time intervals.

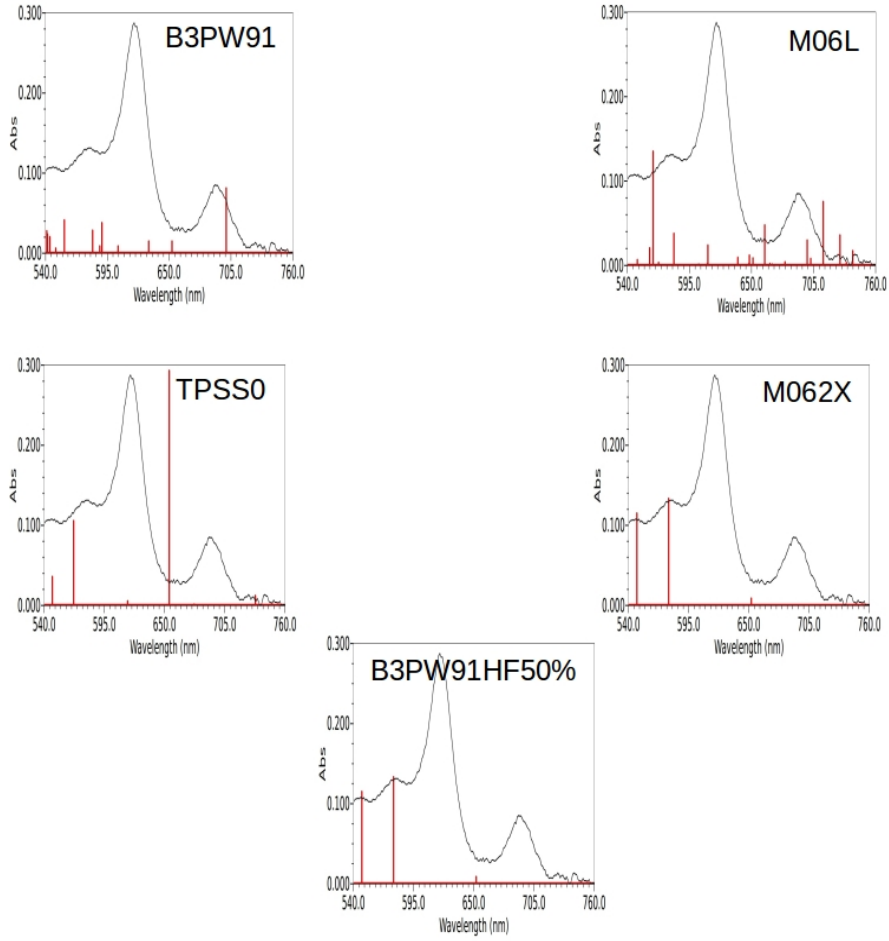

Figure 25: Met-S_A sulfheme TDDFT calculations with different functionals. From https://pubs.acs.org/doi/abs/10.1021/acs.jpcb.7b12393

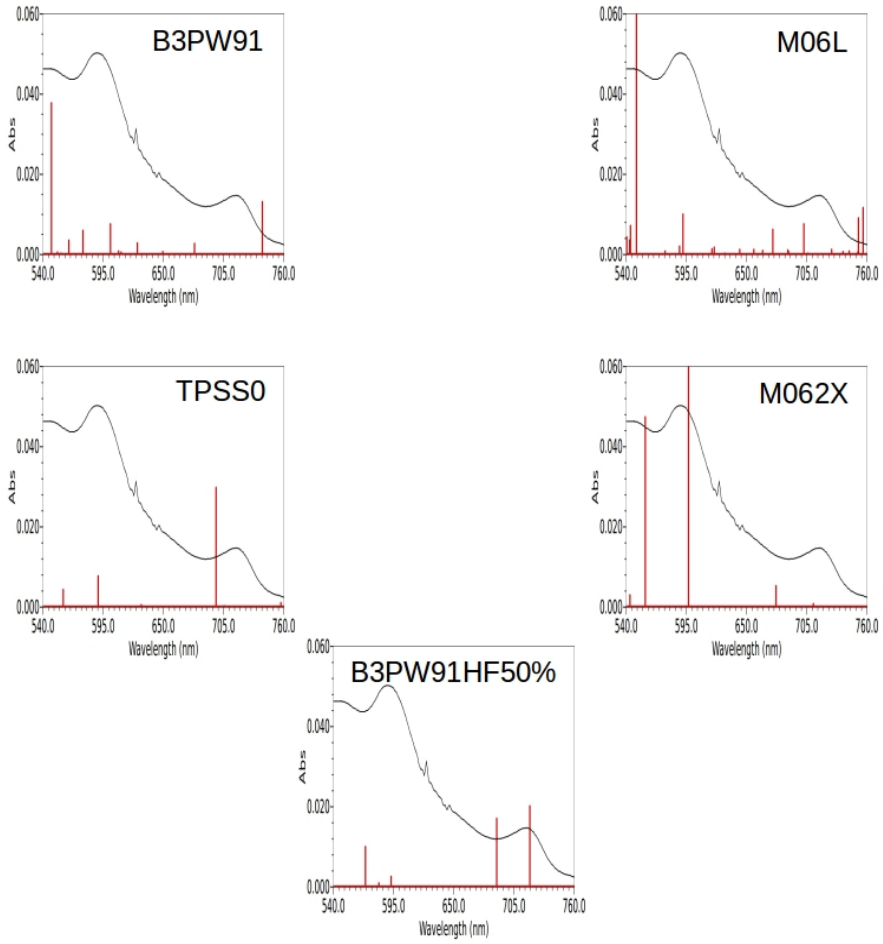

Figure 26: Met-S_C sulfheme TDDFT calculations with different functionals. From https://pubs.acs.org/doi/abs/10.1021/acs.jpcb.7b12393

2.2.4 Sulfheme Complexes UV-Vis Spectra Simulation and Fit.

All of the UV-Vis absorption bands consist of multiple one-electron transitions with varying degrees of orbital mixing. Absorption bands were simulated and fitted to experimental spectra using the Orca's Advance Spectroscopic Analysis (orca_asa) program[142,143,145]. Thus, the experimental spectra at 450 ms, 1 min, 30 min times with a spectral window between 540 to 760 nm were used for spectra fitting.

A sum of Gaussian functions was used for band convolution using the excited state calculated frequencies as reference. UV−visible spectra were convoluted using Gaussian functions with half-widths ranging from approximately 200 cm^{-1} to 1800 cm^{-1}. Because the UV-vis spectrum contains unresolved vibrionic structure which can significantly vary depending on the nature of transition, the assumption of unequal Gaussian bandwidths seems to be a physical one[142,143,145,146]. The smallest number of bands which would give a satisfactory fit to the experimental spectra envelope[147] were used. The values for the band width and transition probability, before and after the fit, are shown in **Tables 5** to **8**. The fits have a calculated mean weighted absolute difference (MWAD) value of 0.00821, and an absolute MWAD of $1x10^{-11}$. The area after 715 nm shows an increase spectral noise. This noise does not affect the fit because it is outside of the visible bands of interest.

Table 5: Table of the calculated excited states bands used from S_A sulfheme isomer to fit experimental spectra at 450ms (before fit). Values for T(x,y,z) as calculated by TDDFT. Values modified by program for data fit. From https://pubs.acs.org/doi/abs/10.1021/acs.jpcb.7b12393

Abs Spectrum via electronic transition electric dipole moments (before fit)						
Calculated State	**Wavenumber (cm^{-1})**	**Wavelength (nm)**	**Band width (cm^{-1})sigma**	**T(x)**	**T(y)**	**T(z)**
1	14266.0	701.0	1.000	-0.4105	0.0986	0.0919
2	15320.9	652.7	1.000	-0.1337	0.1001	0.0579
3	15825.9	631.9	1.000	0.1132	-0.1309	0.0284
4	16539.0	604.6	1.000	0.0979	-0.0182	-0.0802
5	16940.7	590.3	1.000	0.0707	-0.1973	0.1687
6	16995.0	588.4	1.000	-0.0134	0.1006	-0.0760
7	17185.5	581.9	1.000	0.0312	-0.0562	0.2224
8	17958.9	556.8	1.000	0.0960	0.1266	0.2245
9	18208.8	549.2	1.000	0.0968	0.0104	-0.0332
10	18382.5	544.0	1.000	-0.1038	0.1301	-0.0904
11	18456.7	541.8	1.000	-0.1992	0.0398	0.0115
12	18476.8	541.2	1.000	-0.2017	0.0549	0.0688

Table 6: Table of the calculated excited states bands used from S_A sulfheme isomer to fit experimental spectra at 450ms (after fit). From https://pubs.acs.org/doi/abs/10.1021/acs.jpcb.7b12393

Abs Spectrum via electronic transition electric dipole moments (after fit)						
Calculated State	**Wavenumber (cm^{-1})**	**Wavelength (nm)**	**Band width (cm^{-1})sigma**	**T(x)**	**T(y)**	**T(z)**
1	14433.32	692.8	218.87	0.0015	-0.0012	-0.0001
2	16414.32	609.2	1244.67	-0.0027	-0.0007	0.0001
3	16121.92	620.3	249.04	-0.0031	-0.0005	-0.0013
4	16565.34	603.7	2073.2	-0.0012	0.0012	0.0004
5	16992.59	588.5	601.94	0.002	0.0019	-0.0005
6	17983.75	556.1	1568.1	0.0009	0.0000	-0.0003
7	15086.31	662.9	2840.07	0.0011	0.0002	-0.0002
8	18296.22	546.6	1325.98	0.0016	0.0010	-0.0007
9	20467.72	488.6	1394.21	-0.0014	0.0013	0.0007
10	20112	497.2	1929.22	0.001	0.0048	0.0004
11	19991.38	500.2	819.78	-0.0032	0.0018	-0.0003
12	18102.67	552.4	2140.11	-0.0001	0.0016	0.0006

Table 7: Table of the calculated excited states bands used from S_C sulfheme isomer to fit experimental spectra at 30min (before fit). Values for T(x,y,z) as calculated by TDDFT. Values modified by program for data fit. From https://pubs.acs.org/doi/abs/10.1021/acs.jpcb.7b12393

Abs Spectrum via electronic transition electric dipole moments (before fit)						
Calculated State	**Wavenumber (cm^{-1})**	**Wavelength (nm)**	**Band width (cm^{-1})sigma**	**T(x)**	**T(y)**	**T(z)**
1	13503.9	740.5	1.000	0.1372	-0.1366	-0.0297
2	14741.0	678.4	1.000	-0.0582	0.0652	-0.0440
3	15398.0	649.4	1.000	0.0896	-0.1266	0.1195
4	15968.4	626.2	1.000	0.0118	-0.0626	0.0498
5	16353.3	611.5	1.000	0.0074	-0.0871	0.0428
6	16419.3	609.0	1.000	-0.0106	0.1243	-0.2894
7	17347.7	576.4	1.000	0.1138	0.1167	0.2181
8	17741.7	563.6	1.000	-0.0951	0.1448	-0.1102
9	17975.7	556.3	1.000	-0.0166	0.0107	0.0408
10	18259.6	547.7	1.000	-0.5809	0.2765	0.1976
11	19636.6	509.3	1.000	0.2744	-0.0802	0.0804
12	19743.5	506.5	1.000	-0.0969	-0.1012	0.1173
13	19862.1	503.5	1.000	-1.0450	0.2696	0.4329

.

Table 8: Table of the calculated excited states bands used from S_C sulfheme isomer to fit experimental spectra at 30min (after fit). From https://pubs.acs.org/doi/abs/10.1021/acs.jpcb.7b12393

Abs Spectrum via electronic transition electric dipole moments (after fit)						
Calculated State	**Wavenumber (cm^{-1})**	**Wavelength (nm)**	**Band width (cm-1)sigma**	**T(x)**	**T(y)**	**T(z)**
1	13917.1	718.5	295.1	-0.0008	0.0001	0.0001
2	14575.1	686.1	736.0	0.0000	-0.0011	0.0002
3	15917.9	628.2	806.9	0.0009	-0.0004	0.0004
4	19303.0	518.1	662.9	0.0002	0.0002	0.0002
5	16414.3	609.2	941.6	-0.0007	-0.0006	0.0013
6	16845.9	593.6	410.1	0.0010	-0.0005	0.0006
7	17554.3	569.7	1023.9	-0.0005	-0.0007	-0.0005
8	18826.4	531.2	4474.2	0.0001	0.0010	0.0001
9	18032.7	554.5	599.2	-0.0009	-0.0005	-0.0002
10	20366.0	491.0	1254.4	0.0000	-0.0004	-0.0003
11	20440.8	489.2	1119.4	-0.0008	-0.0002	-0.0001
12	22326.9	447.9	1135.3	0.0001	-0.0018	0.0002
13	19297.84	518.2	1669.0	-0.0012	0.0031	-0.0007

2.3 Results and Discussion

2.3.1 Sulfheme electronic ground state molecular orbitals

The electronic structure of the highest occupied molecular orbitals (HOMO) for the S_A and S_C sulfheme isomers provides insight into the nature of their electronic properties. **Figure 27** shows the classical electron density of the a_{1u} and a_{2u} HOMO orbitals for the heme molecule under a D_{4h} symmetry described by the four orbital model[130–132] and the analogous HOMO orbitals for the S_A sulfheme isomer (three-membered ring). In the heme and S_A isomer, the a_{1u} orbital density symmetrically dwells around the pyrrole rings carbons, while the a_{2u} orbital density distribution is delocalized over the pyrrole nitrogen atoms and the meso carbons. The a_{1u} orbitals in both cases have a similar pyrrole orbital density while the differences center on pyrrole B in the S_A isomer at the site of sulfur insertion. An increase in electron density around this pyrolytic structure was observed. Nevertheless, the a_{1u} orbital of the sulfheme isomer reveals a contribution from a sulfur *p* orbital which is conjugated with the heme π system and influences the HOMO energies. **Figure 28** shows the calculated HOMO a_{1u} and a_{2u} orbital energies for the met-aquo heme (-6.501 eV, -6.453 eV), met-aquo S_A (- 6.520 eV, -6.812 eV), and met-aquo S_C (-6.316 eV, -6.683 eV) species. The heme contains an a_{2u} orbital with 0.048 eV higher energy than the a_{1u} orbital[130–132]. Changes to the a_{1u} and a_{2u} HOMO ordering and energies results from the sulfur insertion into the heme pyrrole B. In both S_A and S_C sulfheme isomers, there is a substantial decrease in the energy of the a_{2u} orbitals when compared to the unmodified heme group.

The energy of the a_{2u} orbitals are -0.291 eV and -0.368 eV lower in energy than the a_{1u} orbitals for S_A and S_C, respectively. Compared to the heme group, the energy of the a_{1u} orbital energy is lower in both S_A and S_C complexes but the a_{2u} orbital is always higher in energy. The formation of the S_A isomer decreases the a_{1u} and a_{2u} orbitals energy by -0.020 eV and -0.359 , compared to the unmodified heme,

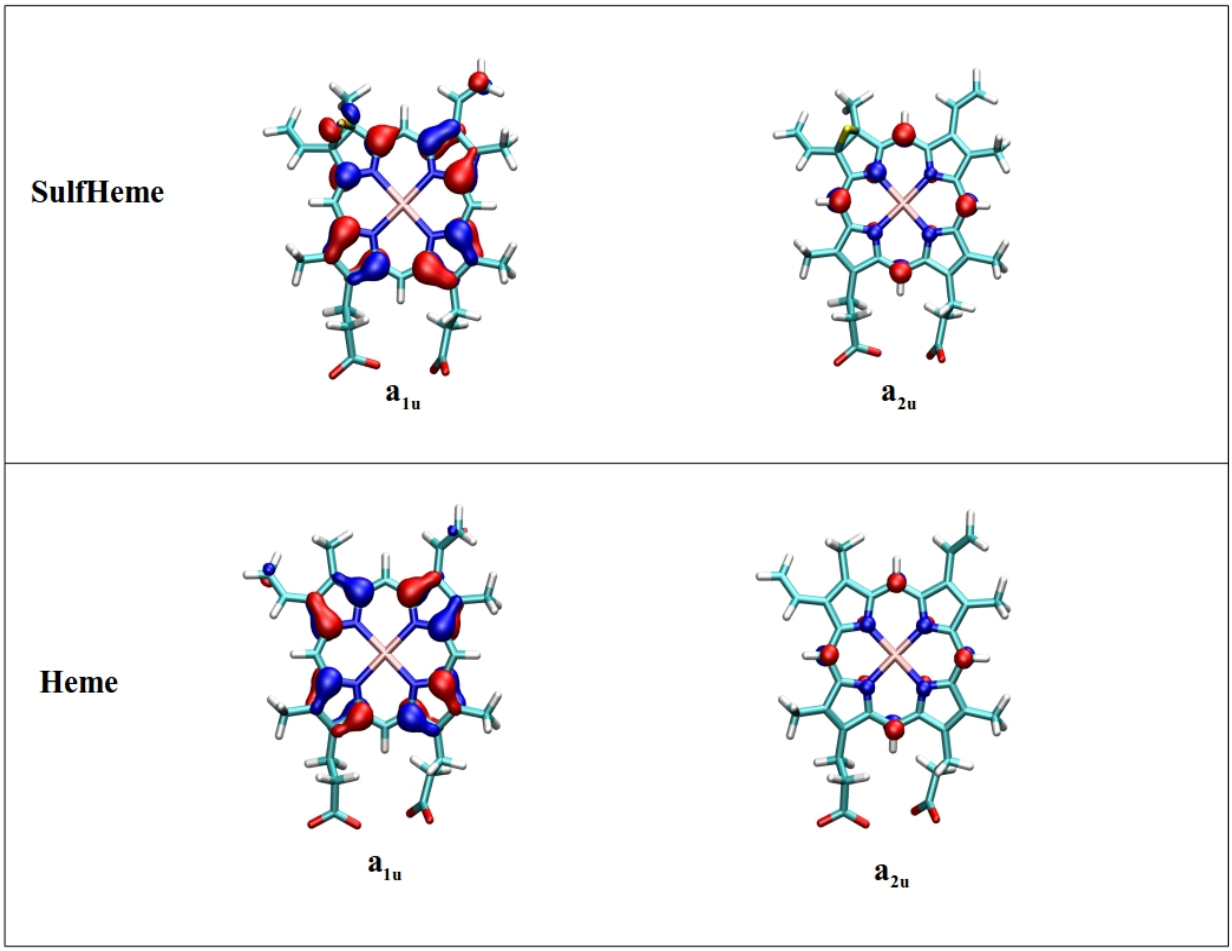

Figure 27: Heme and Sufheme HOMO (a_{1u} and a_{2u}) orbitals. Orbital sign represented by red and blue colors. Red for positive sign, and blue for negative. From https://pubs.acs.org/doi/abs/10.1021/acs.jpcb.7b12393

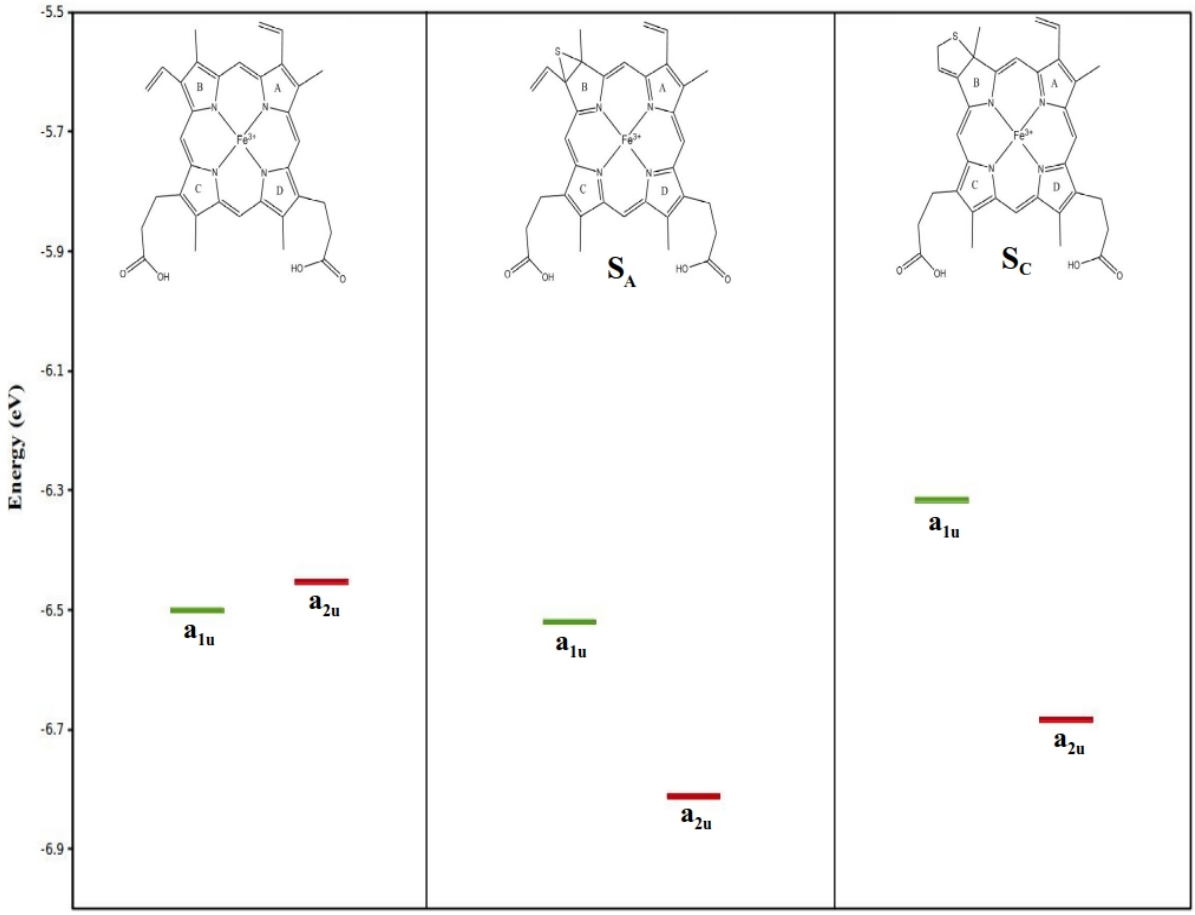

Figure 28: HOMO (a_{1u} and a_{2u}) orbitals energy for the Heme and Sulfheme A and C. From https://pubs.acs.org/doi/abs/10.1021/acs.jpcb.7b12393

respectively. The energy decrease of these orbitals is due to the electron-withdrawing effect of the sulfur insertion which stabilizes these orbitals. In addition, the overlap of the sulfur *p* orbital with the heme π system increases the energy difference between the a_{1u} and the a_{2u} molecular orbitals. The electron density pull out away from the iron center suggests a reduction of the back-bonding effects. SulfMb experiments show an affinity for CO about 1,500 times lower than the unmodified heme, and increases the CO normal mode frequency (stronger C-O bond) by 10 cm^{-1} [39]. The decrease in O_2 and CO affinity of sulfmyoglobin when compared to myoglobin is suggested to be assigned to the electron-density withdraw from the heme iron[39]. The decrease in the a_{2u} orbital energy is similar to the effect of withdrawing groups of pyrrole beta substitution in metal meso-tetraphenylporphyrins[148].

Interestingly, calculations indicate that the a_{1u} and a_{2u} orbital energies of S_C are higher than those of S_A by 0.205 eV and 0.129 eV, respectively. This increase in energy is due to the formation of a more planar sulfheme structure going from the three-membered to a five-membered ring that incorporates the 4-vinyl group and creating an abduct that is now electron-donating. Furthermore, the increased planarity of the sulfheme facilitates a stronger coupling between the sulfur *p* orbital and the heme π system. NMR experiments indicate that the 4-vinyl group of the heme is not necessary for the initial formation of the S_A sulfheme isomer, though clearly this group is required for formation of the S_C sulfheme isomer[43–45,47,48,96,120]. Thus, the electronic properties of the sulfheme adduct, specifically, the changes in the pyrrolic β ring have a considerable effect on the energy of the heme HOMO orbitals modulating the separation energy between the a_{1u} and a_{2u} orbitals[148].

2.3.2 S_A, S_B, and S_C sulfheme electronic excitations

Given a heme with D_{4h} symmetry, the electronic excitations from the HOMO a_{1u} and a_{2u} molecular orbitals to the e_g LUMO molecular orbitals give rise to what is termed the B and Q bands. However, due to the degenerate nature of these former states, the π to π* (a_{1u}/a_{2u} to e_g) excitations

produce two doubly degenerate excited states that undergo configuration interaction to give the corresponding B and the Q bands[130,131,148]. Yet, the electronic sulfheme absorption spectrum more closely resembles those of a metallochlorin structure which has a lower C_{2v} symmetry and an increase in the number of visible electronic bands. The sulfur insertion changes the heme group symmetry to a C_{2v} symmetry. This symmetry modification results in the $a_{1u}(\pi)$ HOMO changing to $a_2(\pi)$, and the $a_{2u}(\pi)$ changing to $a_1(\pi)$. In addition, the e_g LUMO changes to a combination of $b_1(\pi^*$ and $d_{xz})$ and $b_2(d_{yz})$ orbitals.

The MO energy diagram shown in **Figure 29** describes the calculated 740/615/619 nm (S_B), 701/631/605 nm (S_A), and 741/649/626 nm (S_C) electronic transitions for the sulfheme structures. For each S_B, S_A, and S_C isomer model, the energies associated with transitions in the 600 nm and 700 nm regions are calculated based on a set of MOs, shown in **Tables 9** to **17**. The S_B electronic transitions reflect the higher oxidation state of the transient HS-Fe(IV)=O intermediate (**Figure 23**). The higher oxidation state decreases the energy of the $1a_2/a_1$ MOs and increases the energy of the $2a_2$ MO compared to the ground state π MOs in the Fe(III) S_A and S_C derivatives (**Figure 29**). The electronic transitions in the transient S_B intermediate are classified as π to π* and π to d_π (d_{xz} and d_{yz}) excitations. In addition, the ordering of the d_{xz} and d_{yz} LUMOs in the S_B intermediate are reversed when compared with the S_A and S_C derivatives suggesting that the differences in iron oxidation states [(Fe(IV) versus Fe(III)] and structure are the cause. Upon ring closure in the S_A and S_C sulfheme structures, the π S_B HOMO orbitals ($1a_2$ and $2a_2$) collapse into the degenerate π a_2 orbital, while the π a_1 orbital remains unchanged. As discussed earlier, the differences between the calculated 701, 631 and 605 nm (S_A), and 741, 649, and 626 nm (S_C) absorption peaks for the sulfheme structures are due to whether the abduct is electron-withdrawing or electron-donating and is in good agreement with the experimental sulfheme spectra.

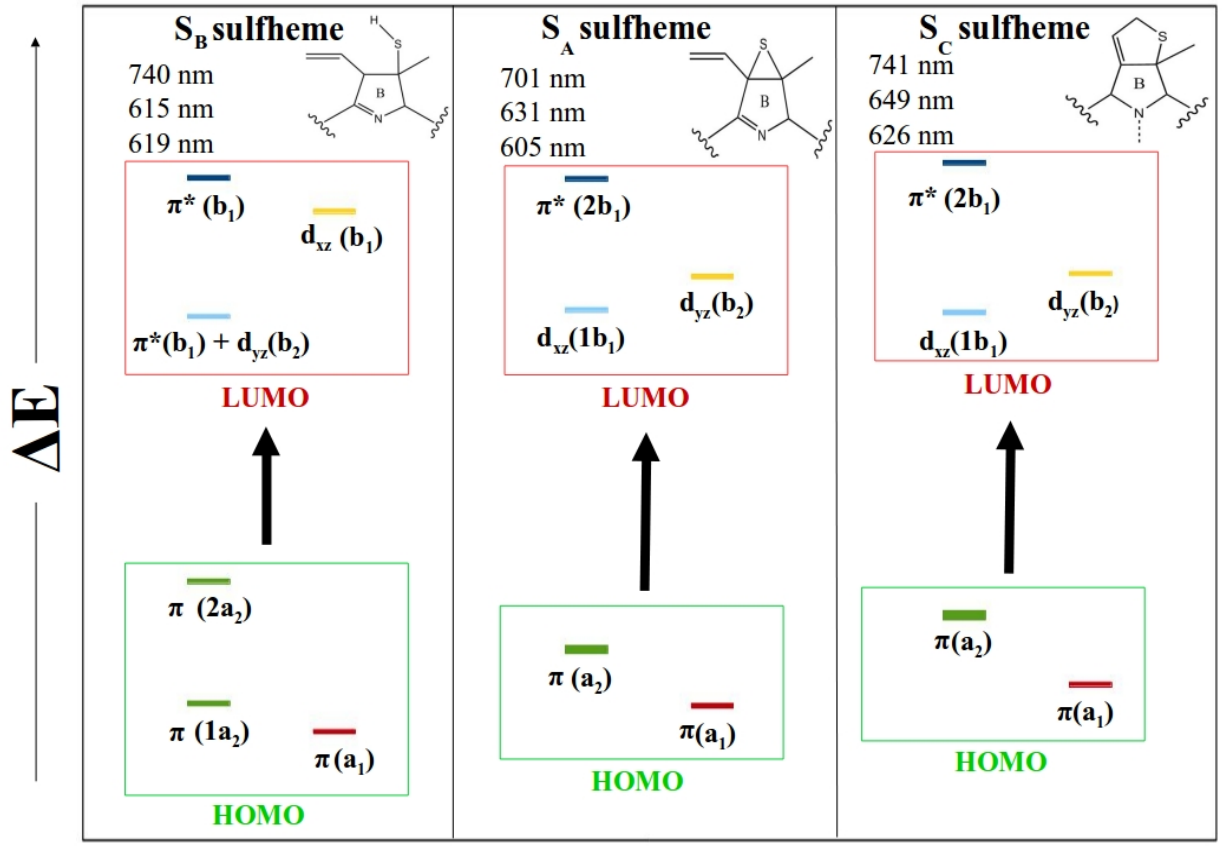

Figure 29: Sulfheme species excited state MO admixed transitions. MOs inside the green square are the HOMO orbitals and the MOs inside the red square are the LUMO orbitals. On top of the red square are the calculated excited states visible region transitions wavelengths for each sulfheme isomer. In parenthesis is the MO symmetry following the C_{2v} point group symmetry approximation for the sulfheme specie. From https://pubs.acs.org/doi/abs/10.1021/acs.jpcb.7b12393

Table 9: Molecular orbitals contributions for the S_A sulfheme isomer calculated 701 nm band. From https://pubs.acs.org/doi/abs/10.1021/acs.jpcb.7b12393

S_A Transition energy= 14266 cm^{-1} (701 nm)		
HOMO	**LUMO**	**MO transition contribution**
224a	225a	0.57608589
223a	226a	0.01935947
222a	227a	0.00196298
221a	228a	0.00086651
220a	229a	0.00049331
219a	230a	0.00021193
219b	220b	0.36699871
218b	221b	0.02736797
217b	222b	0.00178218
216b	223b	0.00153716
215b	224b	0.00068584
214b	225b	0.00044714
213b	226b	0.00028528
212b	227b	0.00023077
211b	228b	0.00018380
210b	229b	0.00014370
209b	230b	0.00012406
208b	231b	0.00011410

Table 10: Molecular orbitals contributions for the S_A sulfheme isomer calculated 631 nm band. From https://pubs.acs.org/doi/abs/10.1021/acs.jpcb.7b12393

S_A Transition energy= 15825.9 cm^{-1} (631 nm)		
HOMO	**LUMO**	**MO transition contribution**
224a	225a	0.24081286
223a	226a	0.03634291
222a	227a	0.00216056
221a	228a	0.00072595
220a	229a	0.00053617
219a	230a	0.00018082
218a	231a	0.00011741
219b	220b	0.57394365
218b	221b	0.11979362
217b	222b	0.01261573
216b	223b	0.00795755
215b	224b	0.00155223
214b	225b	0.00088177
213b	226b	0.00045407
212b	227b	0.00031309
211b	228b	0.00021045
210b	229b	0.00019229
209b	230b	0.00015802
208b	231b	0.00011461

Table 11: Molecular orbitals contributions for the S_A sulfheme isomer calculated 605 nm band. From https://pubs.acs.org/doi/abs/10.1021/acs.jpcb.7b12393

S_A Transition energy= 16539 cm^{-1} (605 nm)		
HOMO	**LUMO**	**MO transition contribution**
224a	225a	0.37831522
223a	226a	0.02154356
222a	227a	0.00129827
221a	228a	0.00027620
220a	229a	0.00019906
219a	230a	0.00018069
219b	220b	0.23522525
218b	221b	0.16863265
217b	222b	0.15748805
216b	223b	0.03415830
215b	224b	0.00071819
214b	225b	0.00041861
213b	226b	0.00025285
212b	227b	0.00012190

Table 12: Molecular orbitals contributions for the S_C sulfheme isomer calculated 740 nm band. From https://pubs.acs.org/doi/abs/10.1021/acs.jpcb.7b12393

S_C Transition energy= 13503.9 cm^{-1} (740 nm)		
HOMO	**LUMO**	**MO transition contribution**
224a	225a	0.57567534
223a	226a	0.01438562
222a	227a	0.00221065
221a	228a	0.00106437
220a	229a	0.00038724
219a	230a	0.00033440
218a	231a	0.00015456
219b	220b	0.38052266
218b	221b	0.01601190
217b	222b	0.00279476
216b	223b	0.00210511
215b	224b	0.00165211
214b	225b	0.00051126
213b	226b	0.00026313
212b	227b	0.00020330
211b	228b	0.00018292
210b	229b	0.00015555
209b	230b	0.00013678
208b	231b	0.00012576

Table 13: Molecular orbitals contributions for the S_C sulfheme isomer calculated 626 nm band. From https://pubs.acs.org/doi/abs/10.1021/acs.jpcb.7b12393

S_C Transition energy= 15968.4 cm^{-1} (626 nm)		
HOMO	**LUMO**	**MO transition contribution**
224a	225a	0.19608358
223a	226a	0.00458550
222a	227a	0.00135390
221a	228a	0.00040313
220a	229a	0.00033886
219a	230a	0.00013970
218a	231a	0.00012703
219b	220b	0.44703798
218b	221b	0.27952384
217b	222b	0.06575867
216b	223b	0.00150112
215b	224b	0.00092323
214b	225b	0.00050136
213b	226b	0.00033482
212b	227b	0.00020869
211b	228b	0.00010368

Table 14: Molecular orbitals contributions for the S_C sulfheme isomer calculated 612 nm band. From https://pubs.acs.org/doi/abs/10.1021/acs.jpcb.7b12393

S_C Transition energy= 16353.3 cm^{-1} (612 nm)		
HOMO	**LUMO**	**MO transition contribution**
224a	225a	0.04951839
223a	226a	0.00408431
222a	227a	0.00079414
221a	228a	0.00017953
219b	220b	0.71349161
218b	221b	0.17062127
217b	222b	0.05593718
216b	223b	0.00249174
215b	224b	0.00136979
214b	225b	0.00038627
213b	226b	0.00022740
212b	227b	0.00019011
211b	228b	0.00010661

Table 15: Molecular orbitals contributions for the S_B sulfheme isomer calculated 742 nm band. From https://pubs.acs.org/doi/abs/10.1021/acs.jpcb.7b12393

S_B Transition energy= 13481.7 cm^{-1} (742 nm)		
HOMO	**LUMO**	**MO transition contribution**
223a	224a	0.51448474
222a	225a	0.01823352
221a	226a	0.00194716
220a	227a	0.00124938
219a	228a	0.00077796
218a	229a	0.00058481
217a	230a	0.00029862
216a	231a	0.00022319
215a	232a	0.00018395
214a	233a	0.00016523
213a	234a	0.00014548
212a	235a	0.00014025
211a	236a	0.00010342
220b	221b	0.36947748
219b	222b	0.07336438
218b	223b	0.00841428
217b	224b	0.00352258
216b	225b	0.00150088
215b	226b	0.00085403
214b	227b	0.00059467
213b	228b	0.00040014
212b	229b	0.00026496
211b	230b	0.00023454
210b	231b	0.0001985
209b	232b	0.00018906
208b	233b	0.00017441
207b	234b	0.00014121
206b	235b	0.00010586

Table 16: Molecular orbitals contributions for the S_B sulfheme isomer calculated 619 nm band. From https://pubs.acs.org/doi/abs/10.1021/acs.jpcb.7b12393

S_B Transition energy= 16153.5 cm^{-1} (619 nm)		
HOMO	**LUMO**	**MO transition contribution**
223a	224a	0.05742923
222a	225a	0.01521334
221a	226a	0.00414337
220a	227a	0.00342812
219a	228a	0.00056707
218a	229a	0.00038074
217a	230a	0.00014789
216a	231a	0.00011549
220b	221b	0.59203805
219b	222b	0.23257271
218b	223b	0.08051981
217b	224b	0.01010287
216b	225b	0.00083838
215b	226b	0.00055893
214b	227b	0.00035458
213b	228b	0.00025575
212b	229b	0.00016413

Table 17: Molecular orbitals contributions for the S_B sulfheme isomer calculated 615 nm band. From https://pubs.acs.org/doi/abs/10.1021/acs.jpcb.7b12393

S_B Transition energy= 16251.8 cm^{-1} (615 nm nm)		
HOMO	**LUMO**	**MO transition contribution**
223a	224a	0.91587685
222a	225a	0.00446121
221a	226a	0.00148241
220a	227a	0.00030341
219a	228a	0.00022116
220b	221b	0.03792554
219b	222b	0.02594335
218b	223b	0.01144494
217b	224b	0.00148446
216b	225b	0.00024469
215b	226b	0.00010994

2.3.3 Molecular orbitals that contribute to the absorption spectra for S_A, S_B, S_C isomers

The general HOMO to LUMO transitions representing the S_A, S_B, and S_C isomers in **Figure 29** are described more quantitatively in **Figures 30**, **31** and **32**, respectively, as HOMO alpha (HOMOA) to LUMO alpha (LUMOA), HOMO beta, (HOMOB) to LUMO beta (LUMOB) and next-HOMO to next-LUMO. The MOs responsible for the electronic transitions of the S_A sulfheme are shown in **Figure 30**. The α HOMO (HOMOA) and β HOMO (HOMOB) primarily differ in sign. Both MOs reveal the presence of the sulfur *p* orbital, but next-HOMO lacks this contribution. The π system of the heme and the iron d_{xz}/d_{yz} orbitals constitute the α LUMO (LUMOA), β LUMO (LUMOB) and next-LUMO, respectively. The calculations indicate that the most prominent electronic excitations are associated with the 701, 631, and 605 nm absorption bands. The 701 nm absorption band is primarily a combination of (HOMOA - LUMOA) (0.57) + (HOMOB-LUMOB) (0.37). Therefore, the 701 nm band has characteristics of a classical π to π* transition coupled to charge transfer from the porphyrin ring to the iron atom. The 631 nm absorption band is composed by (HOMOA-LUMOA) (0.24) + (HOMOB-LUMOB) (0.57) + (netxHOMOB–nextLUMOB) (0.11). This transition is associated with charge transfer from the porphyrin ring to the d_{xz} and d_{yz} orbitals of the iron atom with a relatively small contribution of the π to π* transition. Finally, the 605 nm band arises from a combination of (HOMOA-LUMOA)(0.37) + (HOMOB-LUMOB)(0.24) + (nextHOMOB-nextLUMOB)(0.16), which also involves charge transfer from the porphyrin ring to the d_π orbitals, d_{xz} and d_{yz}, of the iron atom with a relatively small contribution of the π to π* transition.

The MOs responsible for the electronic transitions of the S_c isomer are shown in **Figure 31** for the most prominent bands at 740, 626 and 601 nm. The 740 nm absorption band is characterized by the transitions (HOMOA - LUMOA) (0.58) + (HOMOB-LUMOB) (0.38), which is very similar to the 701 nm band of S_A. The 626 nm band is defined by the transitions (HOMOA-LUMOA) (0.20) + (HOMOB-

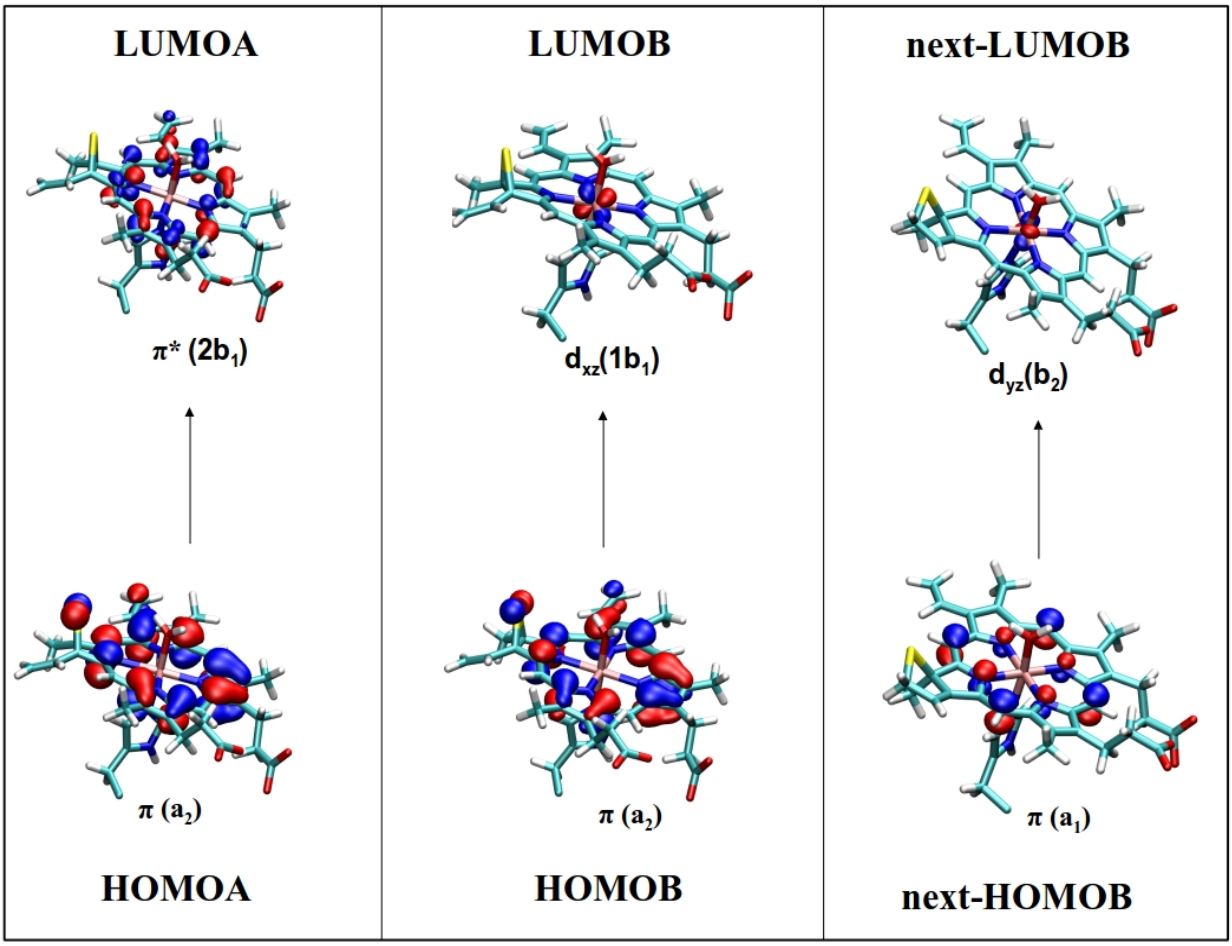

Figure 30: Met-S_A sulfheme MO involve in the transitions of the 701 nm, 631 nm band and 609 nm. The 701 nm band transition is primarily from (HOMOA -LUMOA)(0.57) + (HOMOB-LUMOB)(0.37). The 631 nm band is formed of transitions (HOMOB-LUMOB)(0.57) + (HOMOA-LUMOA)(0.24) + (nextHOMOB–next LUMOB)(0.11). The 605 nm band is formed of transitions (HOMOA-LUMOA) (0.37)+(HOMOB-LUMOB)(0.24) + (nextHOMOB–nextLUMOB)(0.16). From https://pubs.acs.org/doi/abs/10.1021/acs.jpcb.7b12393

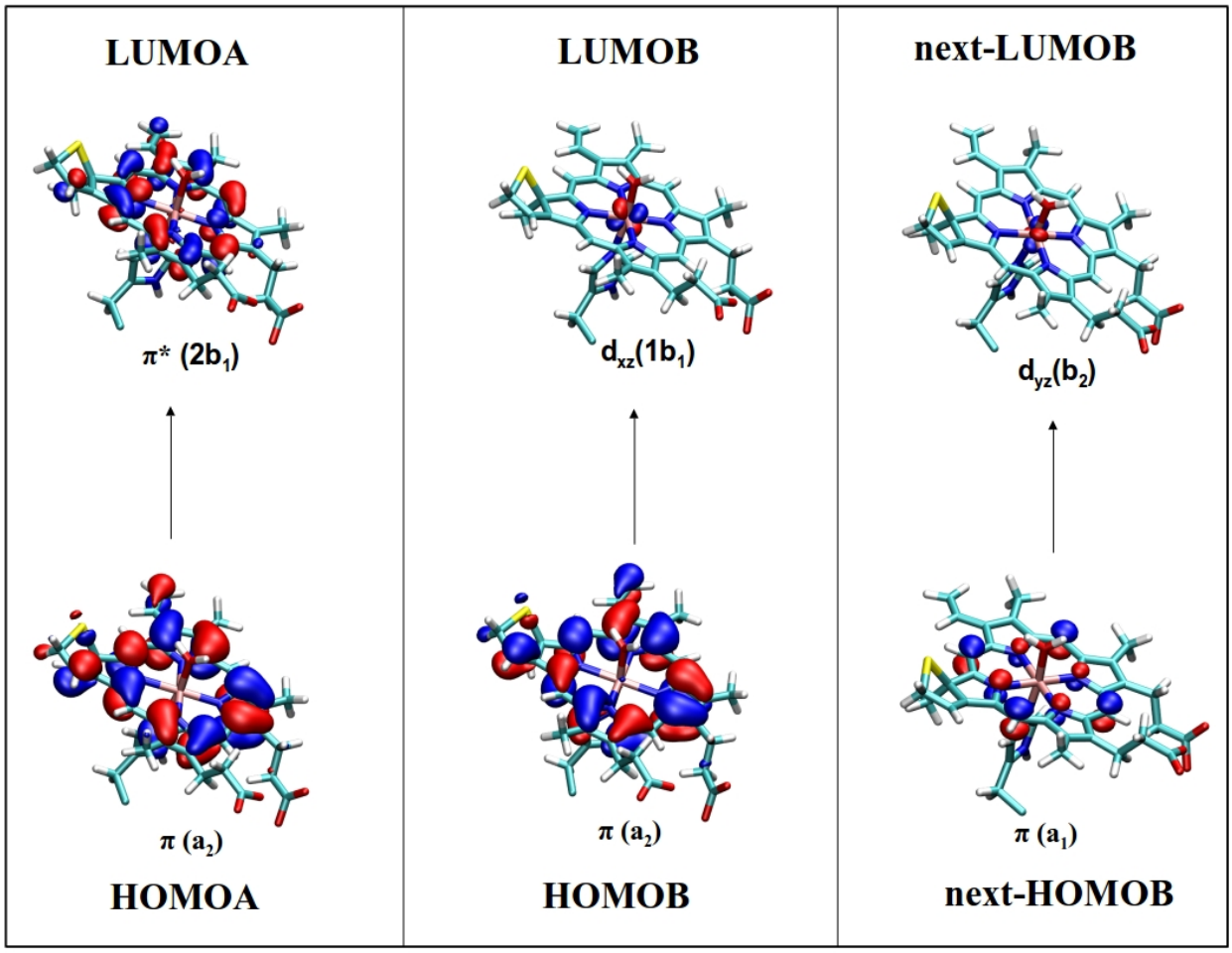

Figure 31: Met-S_C sulfheme MO involve in the transitions of the 740 nm, 626 nm and 612 bands. The 740 nm band characterize (HOMOA - LUMOA) (0.58) + (HOMOB-LUMOB) (0.38), The 626 nm band transitions include (HOMOB-LUMOB(0.44))+(next-HOMOB-next-LUMO(0.28))+(HOMOA-LUMOA(0.20). Finally, the 612 nm transitions include (HOMOB-LUMOB(0.34))+(nextHOMOB-nextLUMOB(0.27))+(HOMOA-LUMOA(0.28)). From https://pubs.acs.org/doi/abs/10.1021/acs.jpcb.7b12393

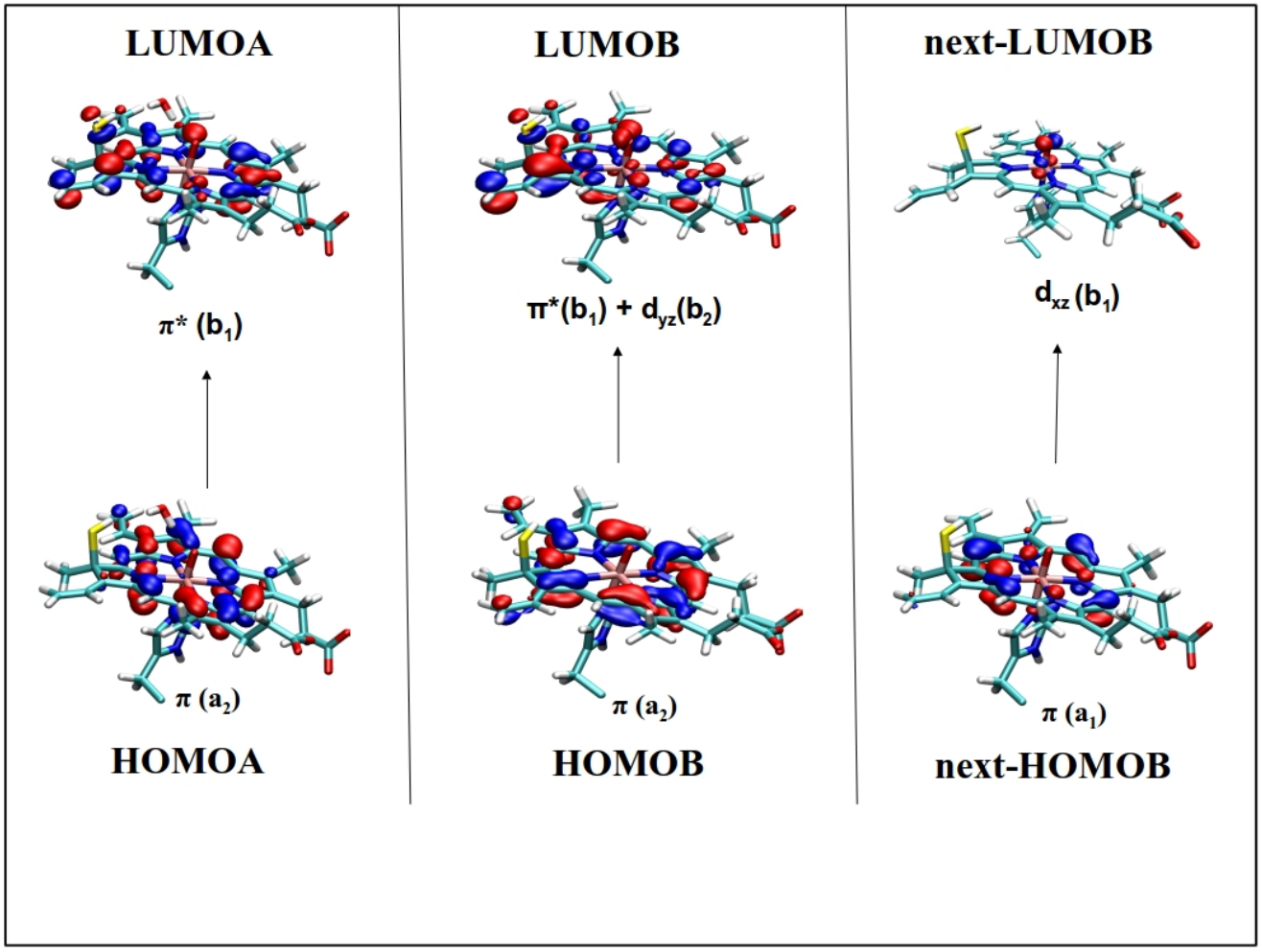

Figure 32: CompII-S_B sulfheme MO involve in the transitions of 742 nm, 619 nm and 615 nm. The 742 nm band is formed of transitions (HOMOB-LUMOB)(0.37) + (HOMOA -LUMOA)(0.51). The 619 nm band is formed of transitions (HOMOB-LUMOB)(0.59) + (next HOMOB-next LUMOB)(0.23). 615 nm band is primary composed of a transition of (HOMOA -LUMOA)(0.92). From https://pubs.acs.org/doi/abs/10.1021/acs.jpcb.7b12393

LUMOB) (0.44) + (nextHOMOB-nextLUMOB) (0.28). The 601 nm band is formed by the transitions (HOMOA-LUMOA (0.28) + (HOMOB-LUMOB) (0.34) + (next-HOMOB-next-LUMOB) (0.27), which is also associated with a charge transfer from the porphyrin ring to heme iron the d_π orbitals (d_{xz} and d_{yz}) with a relatively small contribution of the π to π*. **Figure 32**, shows the MO transitions for the transient HS-Fe(IV)=O or S_B sulfheme structure, which in principle can be detected directly only at times shorter than nanoseconds. The HOMOA (a_2) orbital is similar in shape to those of other sulfheme structures and also contains a contribution to this MO from a sulfur *p* orbital. The relevant contrast between S_B (characterized as a ring opened episulfide) and the S_A and S_C structures (episulfide three member and five ring, respectively) is the lack of a strong charge transfer from the heme and sulfur *p* orbitals to the metal d_π system suggesting that ring closure in S_A and S_C structures is necessary for such process.

2.3.4 Experimental and theoretically generated sulfheme (S_A and S_C) visible spectra.

The frequency of the characteristic visible Q band depends on the structure of the sulfheme isomer, the iron oxidation state, pH, and reactant concentrations. For example, isolated deoxy sulfheme S_AMb, S_BMb and S_CMb showed electronic transitions at 618, 618 nm and 636 nm while the met sulfheme derivatives showed electronic transitions at 718, 720 nm and 736 nm, respectively[47]. In real time experiments, broad bands are observed whose shape, intensity and frequency depends on the time of reaction. The observable experimental transitions of sulfMb after 450 ms and 1, 5, and 30 minutes are shown in **Figure 33**. The dynamic nature of the spectra complicates assigning the contribution from each sulfheme isomeric structure. Due to this complex spectra, the S_AMb, S_BMb and S_CMb isomeric structures have only been identified by NMR spectroscopy in their isolated Fe(III)CN complexes[47]. Thus, to determine the contribution of each stable S_AMb and S_CMb product to the observable visible spectra, the calculated theoretical spectrum was fitted to the experimental transition for each isomer

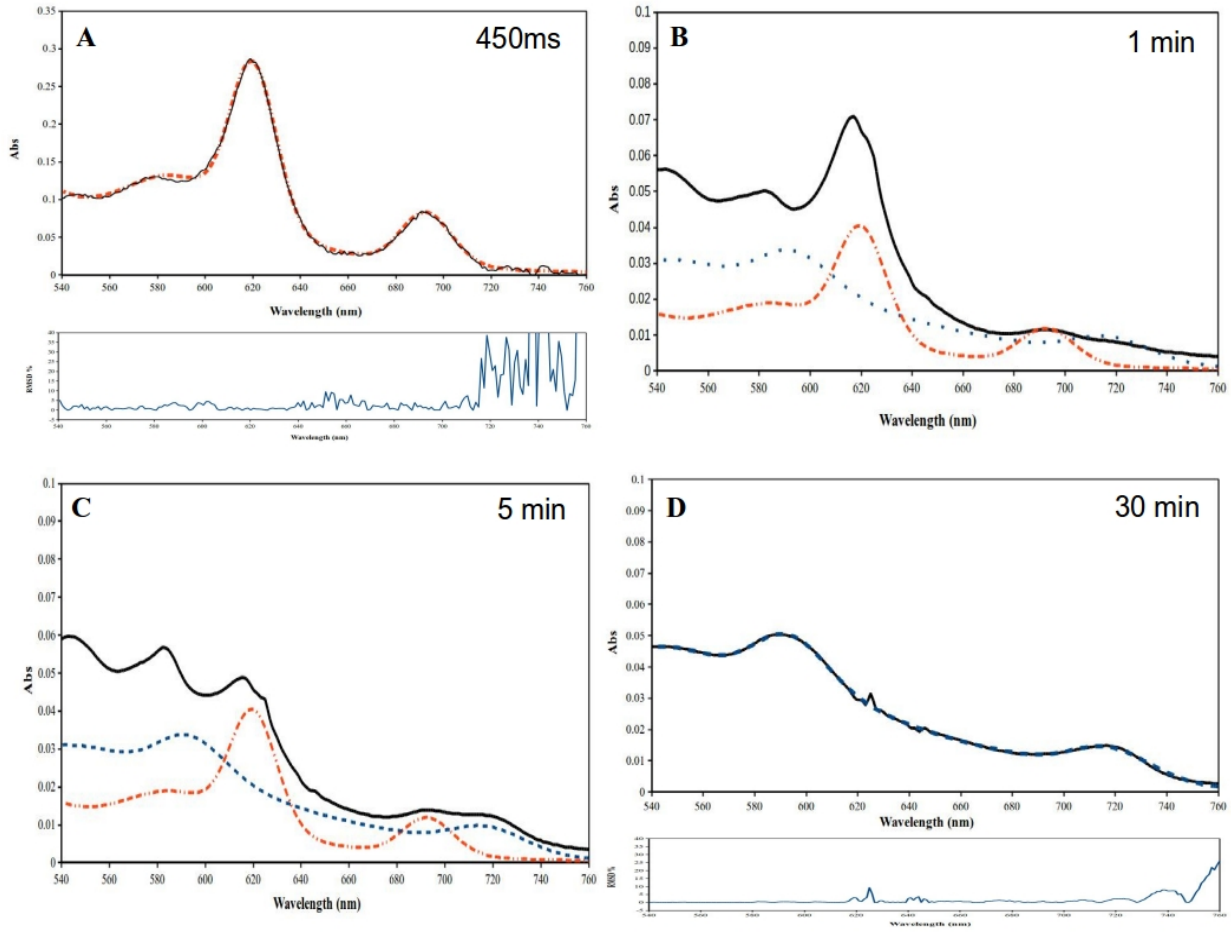

*Figure 33: Sulfheme visible region experimental and simulated fitted spectra. Experimental sulfheme formation spectra (black solid line), S_A simulated spectrum (red-dotted line), and S_C simulated spectrum (blue-dotted line). (**A**) Spectra at 450 ms , (**B**) after 1 min, (**C**) after 5 min, and (**D**) after 30 min. From* https://pubs.acs.org/doi/abs/10.1021/acs.jpcb.7b12393

using the calculated frequencies from **Tables 5** to **8**. The experimental sulfMb spectrum 450 ms after the chemical reaction and the fitted S_A theoretical spectrum is shown in **Figure 34A**. Three predominant transitions at 693, 620 and 588 nm fit with the experimental absorption peaks at 693, 619 and 580 nm. The UV-Vis absorption spectra indicate that at times shorter than one second, the S_A isomer dominates then after that time it is followed by an increase in signal from the S_C isomer.

The absorption spectrum after 30 min along with the S_C calculated theoretical spectrum is shown in **Figure 34B**. Two predominant and sharp transitions are observed at 718 and 593 nm, together with a group of very broad bands at 613, 626 and 682 nm that fit with the experimental bands centered at 720 nm and 593 nm. Taken together, the absorption spectrum is best characterized as coming from a mixture of S_A and S_C isomers with the dominant electronic transitions associated with π to π^* and π to d_π molecular orbitals (**Figure 33C**).

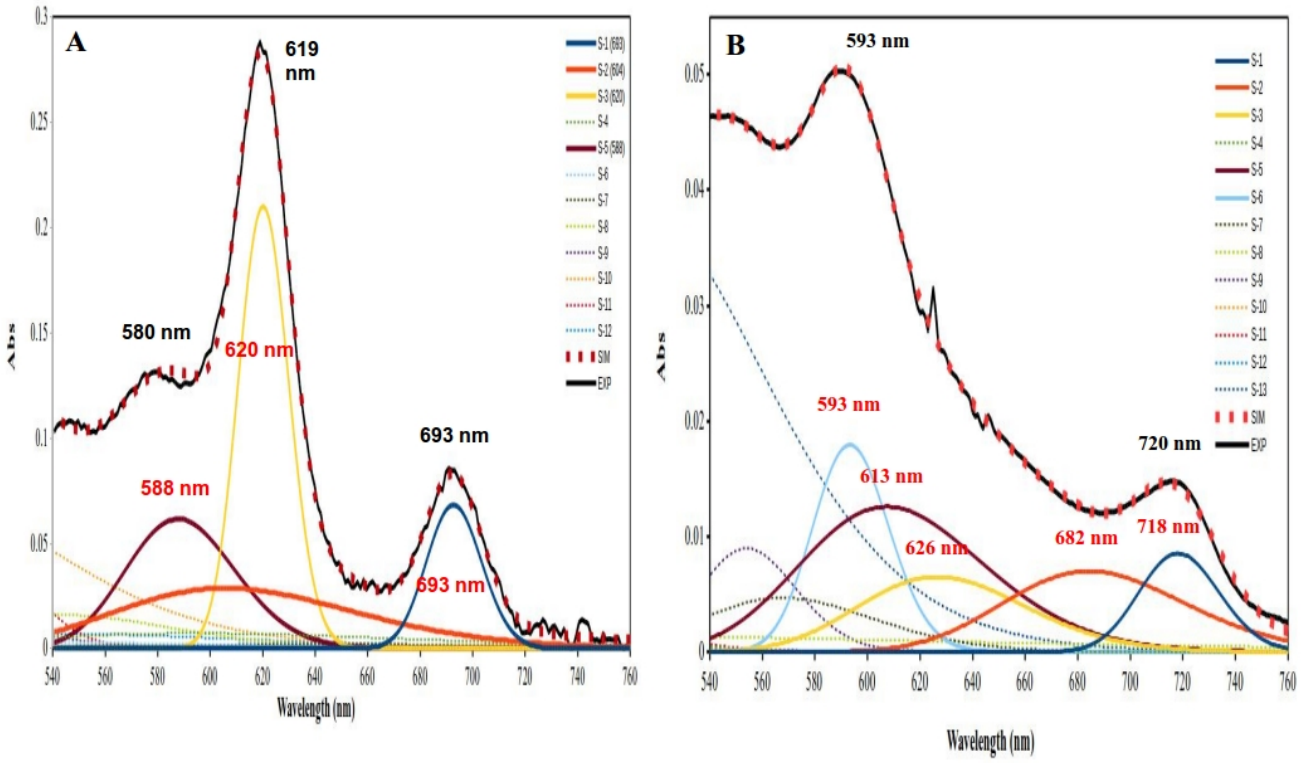

*Figure 34: S_A **(A)** and S_C **(B)** sulfheme simulated spectra fitted to experimental spectra. Experimental wavelength in black and fitted complete spectrum in dotted red. Calculated individual excited state bands in colored solid lines. From https://pubs.acs.org/doi/abs/10.1021/acs.jpcb.7b12393*

2.4 Conclusions

The reactions of Mb or Hb with H_2O_2 and H_2S generates sulfheme isomers S_A and S_C which are responsible for the characteristic visible absorption spectra present in the 600 and 700 nm regions. The TDDFT/MM calculations reveal that the ground state orbitals of sulfheme isomers are modulated by the interplay between the electron withdrawing and electron donating properties of the peripheral groups controlling the separation energy between the a_{1u} and a_{2u} orbitals.

Table 18 summarizes the experimental, calculated, and fitted wavelengths for the S_A and S_C isomers associated with the HOMO-LUMO transitions and characterized by π to π* excitations and by charge transfer (CT) from π to d_π (d_{yz}, d_{xz}) orbitals. These results provide clear indications of sulfheme formation: (1) Experimentally, the absorption maxima are function of the observation time and interplay between the S_A and S_C isomers concentrations, the Sc isomer dominating at longer observation times (2) the 700 nm region of the spectrum is dominated by a mixture of MOs characterized by π to π* transitions, while 600 nm region is dominated by the mixture of MOs characterized by charge transfer from π to d_π (d_{yz}, d_{xz}) transition and indicating that the S_A and S_C isomers have components of a deoxy-like derivative. This result also suggests that oxidation state changes from Fe(III) met-sulfMb to Fe(II) deoxy-sulfMb would place the additional electron into the d_π (d_{yz}, d_{xz}) MOs leading to the appearance of an unique 620 nm band for the deoxy sulfheme derivatives.

*Table 18: The band frequency change between the S_A sulfheme and S_C sulfheme isomers. 1. Principal contribution 2. Secondary contribution * Experimental isolated sulfheme visible bands from chatfield et al.[47] From https://pubs.acs.org/doi/abs/10.1021/acs.jpcb.7b12393*

S_A sulfheme isomer			**S_C sulfheme isomer**			**Type of transition**
Exp. Wavelength (nm)	*Calc. Wavelength (nm)*	*Fit Wavelength (nm)*	*Exp. Wavelength (nm)*	*Calc. Wavelength (nm)*	*Fit Wavelength (nm)*	
693 (718*)	701	693	720 (736*)	741	718	1. π-π* 2. CT(π-d_π)
619 (618*)	631	620		649	682	1. CT(π-d_π) 2. π-π*
613	605	604	618 (636*)	626	626	1. CT(π-d_π) 2. π-π*
580	590	588	593	612	613	1. CT(π-d_π) 2. π-π*

References

(1) Williams, R. J. P. Iron in Evolution. *FEBS Lett.* **2012**, *586* (5), 479–484.

(2) Pantopoulos, K.; Porwal, S. K.; Tartakoff, A. M.; Devireddy, L. Mechanisms of Mammalian Iron Homeostasis. *Biochemistry* **2012**.

(3) Ali, M. E.; Sanyal, B.; Oppeneer, P. M. Electronic Structure, Spin-States, and Spin-Crossover Reaction of Heme-Related Fe-Porphyrins: A Theoretical Perspective. *J. Phys. Chem. B* **2012**, *116* (20), 5849–5859.

(4) Kraus, D.; Wittenberg, J.; Lu, J.; Wittenbergs, B. Hemoglobins of the Lucina Pectinatu/Bacteria Symbiosis I. AN ELECTRON PARAMAGNETIC RESONANCE AND OPTICAL SPECTRAL STUDY OF THE FERRIC PROTEINS. *J. Biol. Chem.* **1990**, *265* (27), 16043–16053.

(5) Flögel, U.; Gödecke, A.; Klotz, L.-O.; Schrader, J. Role of Myoglobin in the Antioxidant Defense of the Heart. *FASEB J.* **2004**, *18* (10), 1156–1158.

(6) Hendgen-Cotta, U. B.; Flögel, U.; Kelm, M.; Rassaf, T. Unmasking the Janus Face of Myoglobin in Health and Disease. *J. Exp. Biol.* **2010**, *213* (Pt 16), 2734–2740.

(7) Cotton, F. A.; Wilkinson, G.; Murillio, C. A.; Bochmann, M. *Advanced Inorganic Chemistry*; Wiley, J., Sons, Eds.; null; Wiley, 1999; Vol. null.

(8) Seib, K. L.; Wu, H.-J.; Kidd, S. P.; Apicella, M. a; Jennings, M. P.; McEwan, A. G. Defenses against Oxidative Stress in Neisseria Gonorrhoeae: A System Tailored for a Challenging Environment. *Microbiol. Mol. Biol. Rev.* **2006**, *70* (2), 344–361.

(9) Kühnel, K.; Derat, E.; Terner, J.; Shaik, S.; Schlichting, I. Structure and Quantum Chemical Characterization of Chloroperoxidase Compound 0, a Common Reaction Intermediate of Diverse Heme Enzymes. *Proc. Natl. Acad. Sci. U. S. A.* **2007**, *104* (1), 99–104.

(10) van Dalen, C. J.; Kettle, a J. Substrates and Products of Eosinophil Peroxidase. *Biochem. J.* **2001**, *358* (Pt 1), 233–239.

(11) Zámocký, M.; Dunand, C. Divergent Evolutionary Lines of Fungal Cytochrome c Peroxidases Belonging to the Superfamily of Bacterial, Fungal and Plant Heme Peroxidases. *FEBS Lett.* **2006**, *580* (28–29), 6655–6664.

(12) Carlsson, G. H.; Nicholls, P.; Svistunenko, D.; Berglund, G. I.; Hajdu, J. Complexes of Horseradish Peroxidase with Formate, Acetate, and Carbon Monoxide. *Biochemistry* **2005**, *44* (2), 635–642.

(13) Farzana, S.; Ganesh, V.; Berchmans, S. A Sensing Platform for Direct Electron Transfer Study of Horseradish Peroxidase. *J. Electrochem. Soc.* **2013**, *160* (9), H573–H580.

(14) Chelikani, P.; Fita, I.; Loewen, P. C. Diversity of Structures and Properties among Catalases. *Cell. Mol. Life Sci.* **2004**, *61* (2), 192–208.

(15) Poulos, T. L.; Kraut, J. The Stereochemistry of Peroxidase Catalysis. *J. Biol. Chem.* **1980**, *255* (17), 8199–8205.

(16) Hersleth, H. H.-P.; Uchida, T.; Røhr, Å.; Røhr, A. K.; Teschner, T.; Schünemann, V.; Kitagawa, T.; Trautwein, A. X.; Görbitz, C. H.; Andersson, K. K. Crystallographic and Spectroscopic Studies of Peroxide-Derived Myoglobin Compound II and Occurrence of Protonated FeIV–O. *J. Biol. Chem.* **2007**, *282* (32), 23372–23386.

(17) Shintaku, M.; Matsuura, K.; Yoshioka, S.; Takahashi, S.; Ishimori, K.; Morishima, I. Absence of a Detectable Intermediate in the Compound I Formation of Horseradish Peroxidase at Ambient Temperature. *J. Biol. Chem.* **2005**, *280* (49), 40934–40938.

(18) Prasad, S.; Mitra, S. Substrate Modulates Compound I Formation in Peroxide Shunt Pathway of Pseudomonas Putida Cytochrome P450cam. *Biochem. Biophys. Res. Commun.* **2004**, *314* (2), 610–614.

(19) Vinogradov, S. N.; Hoogewijs, D.; Bailly, X.; Arredondo-Peter, R.; Gough, J.; Dewilde, S.; Moens, L.; Vanfleteren, J. R. A Phylogenomic Profile of Globins. *BMC Evol. Biol.* **2006**, *6*, 31.

(20) Ordway, G. a; Garry, D. J. Myoglobin: An Essential Hemoprotein in Striated Muscle. *J. Exp. Biol.* **2004**, *207* (Pt 20), 3441–3446.

(21) Evans, S. V; Brayer, G. D. High-Resolution Study of the Three-Dimensional Structure of Horse Heart Metmyoglobin. *J. Mol. Biol.* **1990**, *213* (4), 885–897.

(22) Flögel, U.; Merx, M. W.; Godecke, a; Decking, U. K.; Schrader, J. Myoglobin: A Scavenger of Bioactive NO. *Proc. Natl. Acad. Sci. U. S. A.* **2001**, *98* (2), 735–740.

(23) Wan, L.; Twitchett, M. B.; Eltis, L. D.; Mauk, a G.; Smith, M. In Vitro Evolution of Horse Heart Myoglobin to Increase Peroxidase Activity. *Proc. Natl. Acad. Sci. U. S. A.* **1998**, *95* (22), 12825–12831.

(24) De Jesús-Bonilla, W.; Ramírez-Meléndez, E.; Cerda, J.; López-Garriga, J. Evidence for Nonhydrogen Bonded Compound II in Cyclic Reaction of Hemoglobin I from Lucina Pectinata with Hydrogen Peroxide. *Biopolymers* **2002**, *67* (3), 178–185.

(25) De Jesús-Bonilla, W.; Cortés-Figueroa, J. E.; Souto-Bachiller, F. a; Rodríguez, L.; López-Garriga, J. Formation of Compound I and Compound II Ferryl Species in the Reaction of Hemoglobin I from Lucina Pectinata with Hydrogen Peroxide. *Arch. Biochem. Biophys.* **2001**, *390* (2), 304–308.

(26) Alayash, a I.; Ryan, B. a; Eich, R. F.; Olson, J. S.; Cashon, R. E. Reactions of Sperm Whale Myoglobin with Hydrogen Peroxide. Effects of Distal Pocket Mutations on the Formation and

Stability of the Ferryl Intermediate. *J. Biol. Chem.* **1999**, *274* (4), 2029–2037.

(27) Egawa, T.; Shimada, H.; Ishimura, Y. Formation of Compound I in the Reaction of Native Myoglobins with Hydrogen Peroxide. *J. Biol. Chem.* **2000**, *275* (45), 34858–34866.

(28) Zhang, R.; Newcomb, M. Laser Flash Photolysis Generation of High-Valent Transition Metal-Oxo Species: Insights from Kinetic Studies in Real Time. *Acc. Chem. Res.* **2008**, *41* (3), 468–477.

(29) Olson, K. R.; Deleon, E. R.; Gao, Y.; Hurley, K.; Sadauskas, V.; Batz, C.; Stoy, G. F. Thiosulfate: A Readily Accessible Source of Hydrogen Sulfide in Oxygen Sensing. *Am. J. Physiol. Regul. Integr. Comp. Physiol.* **2013**, *305* (6), R592-603.

(30) Predmore, B. L.; Lefer, D.; Gojon, G. Hydrogen Sulfide in Biochemistry and Medicine. *Antioxid. Redox Signal.* **2012**, No. ja, 1–80.

(31) Wang, K.; Ahmad, S.; Cai, M.; Rennie, J.; Fujisawa, T.; Crispi, F.; Baily, J.; Miller, M. R.; Cudmore, M.; Hadoke, P. W. F.; et al. Dysregulation of Hydrogen Sulfide Producing Enzyme Cystathionine γ-Lyase Contributes to Maternal Hypertension and Placental Abnormalities in Preeclampsia. *Circulation* **2013**, *127* (25), 2514–2522.

(32) Noor, M.; Beutler, E. Acquired Sulfhemoglobinemia. An Underreported Diagnosis? *West. J. Med.* **1998**, *169* (6), 386–389.

(33) Harangi, M.; Mátyus, J.; Nagy, E.; Nagy, E.; Paragh, G.; Balla, J.; Oláh, A. V. Identification of Sulfhemoglobinemia after Surgical Polypectomy. *Clin. Toxicol.* **2007**, *45* (2), 189–192.

(34) Gharahbaghian, L.; Massoudian, B.; Dimassa, G. Methemoglobinemia and Sulfhemoglobinemia in Two Pediatric Patients after Ingestion of Hydroxylamine Sulfate. *West. J. Emerg. Med.* **2009**, *10* (3), 197–201.

(35) Saeedi, A.; A., N.; A., M.-B. Effects of Long-Term Exposure to Hydrogen Sulfide on Human Red Blood Cells. *Int. J. Occup. Environ. Med.* **2015**, *6* (1), 20–25.

(36) Whiteman, M.; Le Trionnaire, S.; Chopra, M.; Fox, B.; Whatmore, J. Emerging Role of Hydrogen Sulfide in Health and Disease: Critical Appraisal of Biomarkers and Pharmacological Tools. *Clin. Sci.* **2011**, *121* (11), 459–488.

(37) Szabõ, C. Hydrogen Sulphide and Its Therapeutic Potential. *Nat. Rev. Drug Discov.* **2007**, *6* (11), 917–935.

(38) Perna, A. F.; Luciano, M. G.; Ingrosso, D.; Pulzella, P.; Sepe, I.; Lanza, D.; Violetti, E.; Capasso, R.; Lombardi, C.; De Santo, N. G. Hydrogen Sulphide-Generating Pathways in Haemodialysis Patients: A Study on Relevant Metabolites and Transcriptional Regulation of Genes Encoding for Key Enzymes. *Nephrol. Dial. Transplant.* **2009**, *24* (12), 3756–3763.

(39) Berzofsky, J. A.; Peisach, J.; Alben, J. O. Sulfheme Proteins. III. Carboxysulfmyoglobin: The Relation between Electron Withdrawal from Iron and Ligand Binding. *J. Biol. Chem.* **1972**, *247* (12), 3774–3782.

(40) Carrico, R. J.; Blumberg, W. E.; Peisach, J. The Reversible Binding of Oxygen to Sulfhemoglobin. *J. Biol. Chem.* **1978**, *253* (20), 7212–7215.

(41) Nicholls, P. The Formation and Properties of Sulphmyoglobin and Sulphcatalase. *Biochem. J.* **1961**, *81* (2), 374–383.

(42) Berzofsky, J. A., Peisach, J., & Blumberg, W. E. Sulfheme Proteins I. Optical and Magnetic Properties of Sulfmyoglobin and Its Derivatives. *J. Biol. Chem.* **1971**, *246* (10), 3367–3377.

(43) Chatfield, M. J.; La Mar, G. N.; Balch, A. L.; Lecomte, J. T. J. Multiple Forms of Sulfmyoglobin as Detected by 1H Nuclear Magnetic Resonance Spectroscopy. *Biochem. Biophys. Res. Commun.* **1986**, *135* (1), 309–315.

(44) Bondoc, L. L.; Chau, M.-H.; Price, M. A.; Timkovich, R. Structure of a Stable Form of Sulfheme. *Biochemistry* **1986**, *25* (1978), 8458–8466.

(45) Timkovich, R.; Vavra, M. R. Proton NMR Spectroscopy of Sulfmyoglobin. **1985**, *24* (1985), 5189–5196.

(46) Berzofsky, J.; Peisach, J.; Blumberg, W.; Berzofsky, J. A., Peisach, J., & Blumberg, W. E. Sulfheme Proteins II. THE REVERSIBLE OXYGENATION OF FERROUS SULFMYOGLOBIN. *J. Biol. Chem.* **1971**, *246* (23), 7366–7372.

(47) Chatfield, M.; Mar, G. La. Proton NMR Characterization of Isomeric Sulfmyoglobins: Preparation, Interconversion, Reactivity Patterns, and Structural Features. *Biochemistry* **1987**, *26* (22), 6939–6950.

(48) Chatfield, M. J.; La Mar, G. N.; Lecomte, J. T. J.; Balch, A. L.; Smith, K. M.; Langry, K. C. Identification of the Altered Pyrrole in Sulfmyoglobin and an Extractable Sulfhemin: Participation of the 4-Vinyl Group in the Saturation of the Pyrrole in One Form of Sulfmyoglobin. *J. Am. Chem. Soc.* **1986**, *108* (22), 7108–7110.

(49) Scharberg, M. A.; La Mar, G. N. Sulfmyoglobin Derived from Deuterohemin Reconstituted Protein. 1. Structure of the Initial Complex Based on the Mechanism of Formation of Subsequent Reaction Products. *J. Am. Chem. Soc.* **1993**, *115* (15), 6513–6521.

(50) Scharberg, M. A.; La Mar, G. N. Sulfmyoglobin Derived from Deuterohemin Reconstituted Protein. 2. Molecular and Electronic Structure Determination of Two Extracted Prosthetic Groups. *J. Am. Chem. Soc.* **1993**, *115* (15), 6522–6528.

(51) Chatfield, M. J.; La Mar, G. N.; Balch, A. L.; Smith, K. M.; Parish, D. W.; LePage, T. J. Proton NMR Study of the Influence of Heme Vinyl Groups on the Formation of the Isomeric Forms of

Sulfmyoglobin. *FEBS Lett.* **1986**, *206* (2), 343–346.

(52) Slater, J. C. A Simplification of the Hartree-Fock Method. *Phys. Rev.* **1951**, *81* (3), 385–390.

(53) Lieb, E. H.; Simon, B. The Hartree-Fock Theory for Coulomb Systems. *Stab. Matter From Atoms to Stars Fourth Ed.* **2005**, *194*, 303–312.

(54) Szabo, A.; Ostlund, N. S. *Modern Quantum Chemistry: Introduction to Advanced Electronic Structure Theory*; 1996.

(55) Møller, C.; Plesset, M. S. Note on an Approximation Treatment for Many-Electron Systems. *Phys. Rev.* **1934**, *46* (7), 618–622.

(56) Foulkes, W. M. C.; Mitas, L.; Needs, R. J.; Rajagopal, G. Quantum Monte Carlo Simulations of Solids. *Rev. Mod. Phys.* **2001**, *73* (1), 33–83.

(57) Hohenberg, P., Kohn, W. Inhomogeneous Electron Gas. *Phys. Rev. B* **1964**, *136* (3B), 864–871.

(58) Kohn, W.; Sham, L. J. Self-Consistent Equations Including Exchange and Correlation Effects. *Phys. Rev.* **1965**, *140* (4A).

(59) Thomas, L. H. The Calculation of Atomic Fields. *Math. Proc. Cambridge Philos. Soc.* **1927**, *23* (5), 542–548.

(60) Dirac, P. A. M. Note on Exchange Phenomena in the Thomas Atom. *Math. Proc. Cambridge Philos. Soc.* **1930**, *26* (3), 376–385.

(61) Yin, Z. Microscopic Mechanisms of Magnetism and Superconductivity Studied from First Principle Calculations, Peking University, 2009.

(62) Becke, A. D. Perspective: Fifty Years of Density-Functional Theory in Chemical Physics. *J. Chem. Phys.* **2014**, *140* (18), 18A301.

(63) Perdew, J. P.; Kurth, S. Density Functionals for Non-Relativistic Coulomb Systems in the New Century. **2003**, 1–55.

(64) Perdew, J. P. Density-Functional Approximation for the Correlation Energy of the Inhomogeneous Electron Gas. *Phys. Rev. B* **1986**, *33* (12), 8822–8824.

(65) Perdew, J. P.; Burke, K.; Ernzerhof, M. Generalized Gradient Approximation Made Simple. *Phys. Rev. Lett.* **1996**, *77* (18), 3865–3868.

(66) Becke, A. D. Density□functional Thermochemistry. III. The Role of Exact Exchange. *J. Chem. Phys.* **1993**, *98* (7), 5648–5652.

(67) Rizzi, M.; Wittenberg, J. B.; Coda, A.; Ascenzi, P.; Bolognesi, M. Structural Bases for Sulfide Recognition in Lucina Pectinata Hemoglobin I. *J. Mol. Biol.* **1996**, *258* (1), 1–5.

(68) Brooks, B. R.; Brooks, C. L.; Mackerell, A. D.; Nilsson, L.; Petrella, R. J.; Roux, B.; Won, Y.;

Archontis, G.; Bartels, C.; Boresch, S.; et al. CHARMM: The Biomolecular Simulation Program. *J. ...* **2009**, *30* (10), 1545–1614.

(69) Mackerell, A. D. Empirical Force Fields for Biological Macromolecules: Overview and Issues. *J. Comput. Chem.* **2004**, *25* (13), 1584–1604.

(70) MacKerell, A. D.; Feig, M.; Brooks, C. L. Improved Treatment of the Protein Backbone in Empirical Force Fields. *J. Am. Chem. Soc.* **2004**, *126* (3), 698–699.

(71) Jorgensen, W. L., Chandrasekhar, J., Madura, J. D., Impey, R. W., & Klein, M. L. Comparison of Simple Potential Functions for Simulating Liquid Water. *J. Chem. Phys.* **1983**, *79* (2), 926–935.

(72) Autenrieth, F.; Tajkhorshid, E.; Baudry, J.; Luthey-Schulten, Z. Classical Force Field Parameters for the Heme Prosthetic Group of Cytochrome C. *J. Comput. Chem.* **2004**, *25* (13), 1613–1622.

(73) Darden, T.; York, D.; Pedersen, L. Particle Mesh Ewald: An N·log(N) Method for Ewald Sums in Large Systems. *J. Chem. Phys.* **1993**, *98* (12), 10089.

(74) Ryckaert, J.; Ciccotti, G.; Berendsen, H. Numerical Integration of the Cartesian Equations of Motion of a System with Constraints: Molecular Dynamics of n-Alkanes. *J. Comput. Phys.* **1977**, *341*.

(75) Stewart, J. J. P. Optimization of Parameters for Semiempirical Methods V: Modification of NDDO Approximations and Application to 70 Elements. *J. Mol. Model.* **2007**, *13* (12), 1173–1213.

(76) Humphrey, W.; Dalke, a; Schulten, K. VMD: Visual Molecular Dynamics. *Journal of molecular graphics*. February 1996, pp 33–38, 27–28.

(77) Kristóf, T.; Liszi, J. Effective Intermolecular Potential for Fluid Hydrogen Sulfide. *J. Phys. Chem. B* **1997**, *101* (28), 5480–5483.

(78) Neese, F. The ORCA Program System. *Wiley Interdiscip. Rev. Comput. Mol. Sci.* **2012**, *2* (1), 73–78.

(79) Wu, R.; Wang, S.; Zhou, N.; Cao, Z.; Zhang, Y. A Proton-Shuttle Reaction Mechanism for Histone Deacetylase 8 and the Catalytic Role of Metal Ions. *J Am Chem Soc* **2010**, *132* (27), 9471–9479.

(80) Rosta, E.; Nowotny, M.; Yang, W.; Hummer, G. Catalytic Mechanism of RNA Backbone Cleavage by Ribonuclease H from Quantum Mechanics/Molecular Mechanics Simulations. *J. Am. Chem. Soc.* **2011**, *133* (23), 8934–8941.

(81) Perdew, J. P.; Zunger, A. Self-Interaction Correction to Density-Functional Approximations for Many-Electron Systems. *Phys. Rev. B* **1981**, *23* (10), 5048–5079.

(82) Becke, A. D. Density-Functional Exchange-Energy Approximation with Correct Asymptotic

Behavior. *Phys. Rev. A* **1988**, *38* (6), 3098–3100.

(83) Schäfer, A.; Huber, C.; Ahlrichs, R. Fully Optimized Contracted Gaussian Basis Sets of Triple Zeta Valence Quality for Atoms Li to Kr. *J. Chem. Phys.* **1992**, *97* (4), 2571–2577.

(84) Schäfer, A.; Huber, C.; Ahlrichs, R. Fully Optimized Contracted Gaussian Basis Sets of Triple Zeta Valence Quality for Atoms Li to Kr. *J. Chem. Phys.* **1994**, *100* (8), 5829–5835.

(85) Eichkorn, K.; Treutler, O.; Ohm, H.; Haser, M.; Ahlrichs, R. Auxiliary Basis-Sets to Approximate Coulomb Potentials . *Chem. Phys. Lett.* **1995**, *240* (4), 283–289.

(86) Eichkorn, K.; Weigend, F.; Treutler, O.; Ahlrichs, R. Auxiliary Basis Sets for Main Row Atoms and Transition Metals and Their Use to Approximate Coulomb Potentials. *Theor. Chem. Accounts Theory, Comput. Model.* **1997**, *97* (1–4), 119–124.

(87) Martin, J. M. L.; Sundermann, A. Correlation Consistent Valence Basis Sets for Use with the Stuttgart-Dresden-Bonn Relativistic Effective Core Potentials: The Atoms Ga-Kr and In-Xe. *J. Chem. Phys.* **2001**, *114* (8), 3408–3420.

(88) Dolg, M.;Wedig, H;Stoll;Preuss, H. Energy Adjusted Ab Initio Pseudopotentials for the First Row Transition Elements. *J. Chem. Phys.* **1987**, *86* (2), 866–872.

(89) Perdew, J. P.; Wang, Y.; Carlo, M. Pair-Distribution Function and Its Coupling-Constant Average for the Spin-Polarized Electron Gas. *Phys. Rev. B* **1992**, *46* (20), 947–954.

(90) Becke, A. D. Density□functional Thermochemistry. III. The Role of Exact Exchange. *J. Chem. Phys.* **1993**, *98* (7), 5648–5652.

(91) Römelt, M.; Ye, S.; Neese, F. Calibration of Modern Density Functional Theory Methods for the Prediction of 57Fe Mössbauer Isomer Shifts: Meta-GGA and Double-Hybrid Functionals. *Inorg. Chem.* **2009**, *48* (3), 784–785.

(92) Bolognesi, M.; Rosano, C.; Losso, R.; Borassi, a; Rizzi, M.; Wittenberg, J. B.; Boffi, a; Ascenzi, P. Cyanide Binding to Lucina Pectinata Hemoglobin I and to Sperm Whale Myoglobin: An x-Ray Crystallographic Study. *Biophys. J.* **1999**, *77* (2), 1093–1099.

(93) Schotte, F.; Lim, M.; Jackson, T. a; Smirnov, A. V; Soman, J.; Olson, J. S.; Phillips, G. N.; Wulff, M.; Anfinrud, P. a. Watching a Protein as It Functions with 150-Ps Time-Resolved x-Ray Crystallography. *Science* **2003**, *300* (5627), 1944–1947.

(94) Bourgeois, D.; Vallone, B.; Schotte, F.; Arcovito, A.; Miele, A. E.; Sciara, G.; Wulff, M.; Anfinrud, P.; Brunori, M. Complex Landscape of Protein Structural Dynamics Unveiled by Nanosecond Laue Crystallography. *Proc. Natl. Acad. Sci.* **2003**, *100* (15), 8704–8709.

(95) Salter, M. D.; Blouin, G. C.; Soman, J.; Singleton, E. W.; Dewilde, S.; Moens, L.; Pesce, A.; Nardini, M.; Bolognesi, M.; Olson, J. S. Determination of Ligand Pathways in Globins: Apolar

Tunnels versus Polar Gates. *J. Biol. Chem.* **2012**, *287* (40), 33163–33178.

(96) Arbelo-Lopez, H. D.; Simakov, N. A.; Smith, J. C.; Lopez-Garriga, J.; Wymore, T. Homolytic Cleavage of Both Heme-Bound Hydrogen Peroxide and Hydrogen Sulfide Leads to the Formation of Sulfheme. *J. Phys. Chem. B* **2016**, *120* (30), 7319–7331.

(97) Elber, R. Ligand Diffusion in Globins: Simulations versus Experiment. *Curr. Opin. Struct. Biol.* **2010**, *20* (2), 162–167.

(98) Ruscio, J. Z.; Kumar, D.; Shukla, M.; Prisant, M. G.; Murali, T. M.; Onufriev, A. V. Atomic Level Computational Identification of Ligand Migration Pathways between Solvent and Binding Site in Myoglobin. *Proc. Natl. Acad. Sci. U. S. A.* **2008**, *105* (27), 9204–9209.

(99) Libardi, S. H.; Pindstrup, H.; Cardoso, D. R.; Skibsted, L. H. Reduction of Ferrylmyoglobin by Hydrogen Sulfide. Kinetics in Relation to Meat Greening. *J. Agric. Food Chem.* **2013**.

(100) Choe, Y. S.; De Montellano, P. R. O. Differential Additions to the Myoglobin Prosthetic Heme Group: Oxidative γ-Meso Substitution by Alkylhydrazines. *J. Biol. Chem.* **1991**, *266* (13), 8523–8530.

(101) Colas, C.; Ortiz De Montellano, P. R. Autocatalytic Radical Reactions in Physiological Prosthetic Heme Modification. *Chem. Rev.* **2003**, *103* (6), 2305–2332.

(102) Maltempo, M. M.; Ohlsson, P. I.; Paul, K. G.; Petersson, L.; Ehrenberg, A. Electron Paramagnetic Resonance Analyses of Horseradish Peroxidase in Situ and after Purification. *Biochemistry* **1979**, *18* (14), 2935–2941.

(103) Derat, E.; Shaik, S.; Rovira, C.; Vidossich, P.; Alfonso-Prieto, M. The Effect of a Water Molecule on the Mechanism of Formation of Compound 0 in Horseradish Peroxidase. *J. Am. Chem. Soc.* **2007**, *129* (20), 6346–6347.

(104) Vidossich, P.; Fiorin, G.; Alfonso-Prieto, M.; Derat, E.; Shaik, S.; Rovira, C. On the Role of Water in Peroxidase Catalysis: A Theoretical Investigation of HRP Compound i Formation. *J. Phys. Chem. B* **2010**, *114* (15), 5161–5169.

(105) Peng, D.; Ogura, H.; Zhu, W.; Ma, L.-H.; Evans, J. P.; Ortiz de Montellano, P. R.; La Mar, G. N. Coupling of the Distal Hydrogen Bond Network to the Exogenous Ligand in Substrate-Bound, Resting State Human Heme Oxygenase. *Biochemistry* **2009**, *48* (47), 11231–11242.

(106) Sharma, P. K.; Kevorkiants, R.; De Visser, S. P.; Kumar, D.; Shaik, S. Porphyrin Traps Its Terminator! Concerted and Stepwise Porphyrin Degradation Mechanisms Induced by Heme-Oxygenase and Cytochrome P450. *Angew. Chemie - Int. Ed.* **2004**, *43* (9), 1129–1132.

(107) Ling, Y.; Davidson, V. L.; Zhang, Y. Unprecedented Fe(IV) Species in a Diheme Protein MauG: A Quantum Chemical Investigation on the Unusual M??Ssbauer Spectroscopic Properties. *J. Phys. Chem. Lett.* **2010**, *1* (19), 2936–2939.

(108) Chatfield, M. J.; La Mar, G. N.; Smith, K. M.; Leung, H. K.; Pandey, R. K. Identification of the Altered Pyrrole in the Isomeric Sulfmyoglobins: Hyperfine Shift Patterns as Indicators of Rine Saturation in Ferric Chlorins. *Biochemistry* **1988**, *27* (5), 1500–1507.

(109) Geoghegan, K. F.; Varghese, A. H.; Feng, X.; Bessire, A. J.; Conboy, J. J.; Ruggeri, R. B.; Ahn, K.; Spath, S. N.; Filippov, S. V; Conrad, S. J.; et al. Deconstruction of Activity-Dependent Covalent Modification of Heme in Human Neutrophil Myeloperoxidase by Multistage Mass Spectrometry (MS(4)). *Biochemistry* **2012**, *51* (10), 2065–2077.

(110) Evans, S. V; Sishta, B. P.; Mauk, a G.; Brayer, G. D. Three-Dimensional Structure of Cyanomet-Sulfmyoglobin C. *Proc. Natl. Acad. Sci. U. S. A.* **1994**, *91* (11), 4723–4726.

(111) Khvostichenko, D.; Choi, A.; Boulatov, R. Density Functional Theory Calculations of the Lowest Energy Quintet and Triplet States of Model Hemes Role of Functional Basis Set and Zero Point Energy Corrections. *J. Phys. Chem. A* **2008**, *112*, 3700–3711.

(112) Hoppe-Seyler, F. Ueber Das Verhalten Des Blutfarbstoffes Im Spectrum Des Sonnenlichtes. *Virchows Arch* **1862**, *23*, 446–449.

(113) Hoppe-Seyler, F. Einwirkung Des Schwefelwasserstoffgases Auf Das Blut. Zentralbl. *Med Wiss* **1863**, *1*, 433–434.

(114) Keilin, D. On the Combination of Methaemoglobin with H2S. *Proc. R. Soc.* **1933**, *113*, 393–404.

(115) Michel, H. A Study of Sulfhemoglobin. *J. Biol. Chem.* **1938**, *126* (1), 323–348.

(116) Pietri, R.; Lewis, A.; León, R. G.; Casabona, G.; Kiger, L.; Yeh, S.-R.; Fernandez-Alberti, S.; Marden, M. C.; Cadilla, C. L.; López-Garriga, J. Factors Controlling the Reactivity of Hydrogen Sulfide with Hemeproteins. *Biochemistry* **2009**, *48* (22), 4881–4894.

(117) Johnson, E. A. The Reversion to Haemoglobin of Sulphhaemoglobin and Its Coordination Derivatives. *BBA - Protein Struct.* **1970**, *207* (1), 30–40.

(118) Berzofsky, J. A., Peisach, J., & Blumberg, W. E. Sulfheme Proteins II. The Reversible Oxygenation of Ferrous Sulfmyoglobin. *J. Biol. Chem.* **1971**, *246* (23), 7366–7372.

(119) Andersson, L.; Loehr, T.; Lim, A.; Mauk, A. Sulfmyoglobin. Resonance Raman Spectroscopic Evidence for an Iron-Chlorin Prosthetic Group. *J. Biol. ...* **1984**, *259* (24), 15340–15349.

(120) Chatfield, M.; La Mar, G. 1H Nuclear Magnetic Resonance Study of the Prosthetic Group in Sulfhemoglobin. *Arch. Biochem. Biophys.* **1992**, *295* (2), 289–296.

(121) Román-Morales, E.; Pietri, R.; Ramos-Santana, B.; Vinogradov, S. N.; Lewis-Ballester, A.; López-Garriga, J. Structural Determinants for the Formation of Sulfhemeprotein Complexes. *Biochem. Biophys. Res. Commun.* **2010**, *400* (4), 489–492.

(122) Pietri, R.; Román-Morales, E.; López-Garriga, J. Hydrogen Sulfide and Hemeproteins:

Knowledge and Mysteries. *Antioxidants redox Signal.* **2011**, *15*, 393–404.

(123) Ríos-González, B. B.; Román-Morales, E. M.; Pietri, R.; López-Garriga, J. Hydrogen Sulfide Activation in Hemeproteins: The Sulfheme Scenario. *J. Inorg. Biochem.* **2014**, *133*, 78–86.

(124) Padovani, D.; Hessani, A.; Castillo, F. T.; Liot, G.; Andriamihaja, M.; Lan, A.; Pilati, C.; Blachier, F.; Sen, S.; Galardon, E.; et al. Sulfheme Formation during Homocysteine S-Oxygenation by Catalase in Cancers and Neurodegenerative Diseases. *Nat. Commun.* **2016**, *7*, 13386.

(125) Nakamura, S.; Nakamura, M.; Yamazaki, I.; Morrison, M. Reactions of Ferryl Lactoperoxidase (Compound II) with Sulfide and Sulfhydryl Compounds. *J. Biol. Chem.* **1984**, *259* (11), 7080–7085.

(126) Bostelaar, T.; Vitvitsky, V.; Kumutima, J.; Lewis, B. E.; Yadav, P. K.; Brunold, T. C.; Filipovic, M.; Lehnert, N.; Stemmler, T. L.; Banerjee, R. Hydrogen Sulfide Oxidation by Myoglobin. *J. Am. Chem. Soc.* **2016**, *138* (27), 8476–8488.

(127) Vitvitsky, V., Yadav, P. K., Kurthen, A., Banerjee, R. Sulfide Oxidation by a Noncanonical Pathway in Red Blood Cells Generates Thiosulfate and Polysulfides. *J. Biol. Chem.* **2015**, *290*, 8310–8320.

(128) Li, S., Hong, M. Protonation, Tautomerization, and Rotameric Structure of Histidine: A Comprehensive Study by Magic-Angle-Spinning Solid-State NMR. *J. Am. Chem. Soc.* **2011**, *133*, 1534–1544.

(129) Shimahara, H. Tautomerism of Histidine 64 Associated with Proton Transfer in Catalysis of Carbonic Anhydrase. *J. Biol. Chem.* **2007**, *282*, 9646–9656.

(130) Gouterman, M. Spectra of Porphyrins. *J. Mol. Spectrosc.* **1961**, *6*, 138–163.

(131) Gouterman, M.; Wagnière, G. H.; Snyder, L. C. Spectra of Porphyrins: Part II. Four Orbital Model. *J. Mol. Spectrosc.* **1963**, *11* (1), 108–127.

(132) Ceulemans, a.; Oldenhof, W.; Gorller-Walrand, C.; Vanquickenborne, L. G. Gouterman's "Four-Orbital" Model and the MCD Spectra of High-Symmetry Metalloporphyrins. *J. Am. Chem. Soc.* **1986**, *108* (6), 1155–1163.

(133) Zerner, M.; Gouterman, M.; Kobayashi, H. Porphyrins. *Theor. Chim. Acta* **1966**, *6* (5), 363–400.

(134) Runge, E.; Gross, E. K. U. Density-Functional Theory for Time-Dependent Systems. *Phys. Rev. Lett.* **1984**, *52* (12), 997–1000.

(135) Marques, M. A. L.; Maitra, N. T.; Nogueira, F. M. S.; Gross, E. K. U.; Rubio, A. Introduction to TDDFT. In *Fundamentals of Time-Dependent Density Functional Theory*; Springer, Berlin, Heidelberg, 2012; Vol. 837, pp 53–99.

(136) Marques, M. A. L.; Gross, E. K. U. Time-Dependent Density Functional Theory. *Annu. Rev. Phys. Chem.* **2004**, *55* (1), 427–455.

(137) Cory, M. G.; Zerner, M. C. Metal-Ligand Exchange Coupling in Transition-Metal Complexes. *Chem. Rev.* **1991**, *91* (5), 813–822.

(138) Anderson, W. P.; Cundari, T. R.; Zerner, M. C. An Intermediate Neglect of Differential Overlap Model for Second□row Transition Metal Species. *Int. J. Quantum Chem.* **1991**, *39* (1), 31–45.

(139) Bhattacharya, S. Ab Initio and TDDFT Investigations on Charge Transfer Transition for the O-Chloranil/Aniline Complex in Gas Phase. *Chem. Phys. Lett.* **2007**, *446* (1–3), 199–205.

(140) Latouche, C.; Palazzetti, F.; Skouteris, D.; Barone, V. High-Accuracy Vibrational Computations for Transition-Metal Complexes Including Anharmonic Corrections: Ferrocene, Ruthenocene, and Osmocene as Test Cases. *J. Chem. Theory Comput.* **2014**, *10* (10), 4565–4573.

(141) Guillaumont, D.; Nakamura, S. Calculation of the Absorption Wavelength of Dyes Using Time-Dependent Density-Functional Theory (TD-DFT). *Dye. Pigment.* **2000**, *46* (2), 85–92.

(142) Petrenko, T.; Neese, F. Analysis and Prediction of Absorption Band Shapes, Fluorescence Band Shapes, Resonance Raman Intensities, and Excitation Profiles Using the Time-Dependent Theory of Electronic Spectroscopy. *J. Chem. Phys.* **2007**, *127* (16).

(143) Petrenko, T.; Neese, F. Efficient and Automatic Calculation of Optical Band Shapes and Resonance Raman Spectra for Larger Molecules within the Independent Mode Displaced Harmonic Oscillator Model. *J. Chem. Phys.* **2012**, *137* (23).

(144) Roman Morales, E. M. Global and Local Structural Analysis of the Sulfheme Complex: A Role in the Decrease of Myoglobin Functionality, Univeristy of Puerto Rico Mayagüez Campus, 2016.

(145) Neese, F.; Petrenko, T.; Ganyushin, D.; Olbrich, G. Advanced Aspects of Ab Initio Theoretical Optical Spectroscopy of Transition Metal Complexes: Multiplets, Spin-Orbit Coupling and Resonance Raman Intensities. *Coord. Chem. Rev.* **2007**, *251* (3–4), 288–327.

(146) Petrenko, T.; Krylova, O.; Neese, F.; Sokolowski, M. Optical Absorption and Emission Properties of Rubrene: Insight from a Combined Experimental and Theoretical Study. *New J. Phys.* **2009**, *11*.

(147) Kuter, D.; Venter, G. A.; Naidoo, K. J.; Egan, T. J. Experimental and Time-Dependent Density Functional Theory Characterization of the UV-Visible Spectra of Monomeric and μ-Oxo Dimeric Ferriprotoporphyrin IX. *Inorg. Chem.* **2012**, *51* (19), 10233–10250.

(148) Binstead, R. A.; Crossley, M. J.; Hush, N. S. Modulation of Valence Orbital Levels of Metalloporphyrins by Beta-Substitution - Evidence from Spectroscopic and Electrochemical Studies of 2-Substituted Metallo-5,10,15,20-Tetraphenylporphyrins. *Inorg. Chem.* **1991**, *30* (6), 1259–1264.